DOE/NASA/0110-1
NASA CR-165619

NASA-CR-165619
19830007196

Advanced Ceramic Coating Development For Industrial/Utility Gas Turbine Applications

C.A. Andersson, S.K. Lau, R.J. Bratton, and S.Y. Lee
Research and Development Center

K.L. Rieke, J. Allen, and K.E. Munson
Combustion Turbine Systems Division

February 1982

Prepared for
NATIONAL AERONAUTICS AND SPACE ADMINISTRATION
Lewis Research Center
Under Contract DEN 3-110

for
U.S. DEPARTMENT OF ENERGY
Fossil Energy
Office of Coal Utilization

DOE/NASA/0110-1
NASA CR-165619

Advanced Ceramic Coating Development For Industrial/Utility Gas Turbine Applications

C.A. Andersson, S.K. Lau, R.J. Bratton, and S.Y. Lee
Westinghouse Electric Corporation
Research and Development Center
1310 Beulah Road
Pittsburgh, Pennsylvania 15235

and

K.L. Rieke, J. Allen, and K.E. Munson
Westinghouse Electric Corporation
Combustion Turbine Systems Division
925 Baltimore Pike
Concordville, Pennsylvania 19331

February 1982

Prepared for
NATIONAL AERONAUTICS AND SPACE ADMINISTRATION
Lewis Research Center
Cleveland, Ohio 44135
Under Contract DEN 3-110

for
U.S. DEPARTMENT OF ENERGY
Fossil Energy
Office of Coal Utilization
Washington, D.C. 20545
Under Interagency Agreement DE-AI01-77ET13111

1. Report No.	2. Government Accession No.	3. Recipient's Catalog No.
NASA CR-165619		

4. Title and Subtitle	5. Report Date
ADVANCED CERAMIC COATING DEVELOPMENT FOR INDUSTRIAL/UTILITY GAS TURBINE APPLICATIONS	February 1982
	6. Performing Organization Code
7. Author(s)	8. Performing Organization Report No.
C. A. Andersson, S. K. Lau, R. J. Bratton, S. Y. Lee, K. L. Rieke, J. Allen, and K. E. Munson	
	10. Work Unit No.
9. Performing Organization Name and Address	11. Contract or Grant No.
Westinghouse Electric Corporation Research & Development Center 1310 Beulah Road Pittsburgh, Pennsylvania 15235	DEN 3-110
	13. Type of Report and Period Covered
12. Sponsoring Agency Name and Address	Contractor Report
U. S. Department of Energy Office of Coal Utilization Washington, D.C. 20545	14. Sponsoring Agency Code Report No. DOE/NASA/0110-1

15. Supplementary Notes

Final Report. Prepared under Interagency Agreement DE-AI01-77ET13111. Project Manager, G. E. McDonald, Materials Division, NASA Lewis Research Center, Cleveland, Ohio 44135.

16. Abstract

Ceramic coating systems for industrial/utility turbine components with improved lifetimes in corrosive environments were developed. The plasma sprayed coatings consisted of a metallic NiCrAlY bond coat layer, a porous, coarse grained zirconia-yttria ceramic layer, and a dense, fine grained zirconia-yttria or zirconia-yttria plus glass overcoat layer. Nickel-chromium alloy wire screens intermediate to the bond and ceramic coatings in these systems also proved to be beneficial. The best coating system operating in combustion gases doped with sea salt ratioed to 100 ppm sodium and 2 percent sulphur, had a lifetime 4.5 times that of the baseline porous zirconia-yttria coating.

The effects of ceramic coatings on the lifetimes of metal turbine components and on the performance of a utility turbine, as well as of the turbine operational cycle on the ceramic coatings were analytically determined. When operating the turbine under conditions of constant cooling flow, the first row blades run 55K cooler, and as a result, would be expected to have ten times the creep rupture life, ten times the low cycle fatigue life and twice the corrosion life with only slight decreases in both specific power and efficiency. When operating the turbine at constant metal temperature and reduced cooling flow, both specific power and efficiency will increase, with no change in component lifetime. The most severe thermal transient of the turbine will cause the coating bond stresses to approach 60 percent of the bond strengths.

An understanding of ceramic coating failures was also achieved. Analytic models based on fracture mechanics theories, combined with measured properties were used to quantitatively assess both single and multiple thermal cycle failures. This allowed coating lifetime predictions to be made. Qualitative models for corrosion failures are also presented.

17. Key Words (Suggested by Author(s))	18. Distribution Statement
Ceramic Coatings; Corrosion Resistance; Thermal Barriers; Turbine Performance; Lifetime Improvement; Failure Analysis	Unclassified - unlimited Star Category 26 DOE Category UC-25

19. Security Classif. (of this report)	20. Security Classif. (of this page)	21. No. of Pages	22. Price*
Unclassified	Unclassified	139	

* For sale by the National Technical Information Service, Springfield, Virginia 22161

TABLE OF CONTENTS

TABLE OF CONTENTS (Cont.)

TABLE OF CONTENTS (Cont.)

LIST OF FIGURES

LIST OF FIGURES (Cont.)

LIST OF FIGURES (Cont.)

LIST OF FIGURES (Cont.)

LIST OF FIGURES (Cont.)

LIST OF FIGURES (Cont.)

LIST OF TABLES

LIST OF TABLES (Cont.)

FORWARD

The authors wish to acknowledge the technical assistance of W. J. Carmen, J. J. Nalevanko, M. J. Testa, K. L. Kussmaul, R. W. Palmquist, E. S. Diaz, Dr. E. A. DeZubay, and J. Valentich of the Westinghouse Research and Development Center. In addition, they wish to acknowledge Dr. J. Patten of Battelle Pacific Northwest Laboratories and Dr. E. Demaray of Airco Temescal for their coating applications.

1. SUMMARY

The major objective of this program was to develop ceramic coatings which increase industrial/utility gas turbine hot section durability with heavy emphasis on operation with lower grade petroleum base fuels and liquid coal derived fuels. The second objective was to take advantage of the insulative properties of ceramic coatings on turbine airfoils and combustors without incurring a meaningful penalty in obtaining the primary objective.

In accordance with the overall objectives, the program was organized into the following technical tasks.

Task I: Preliminary Coating Development and Screening Tests

Task IA: Burner Rig Exposure Tests

Task IB: Thermomechanical Property Evaluation

Task II: Preliminary Coating Design Criteria

Task III: Coating Improvement and Endurance Testing

Coating development proceeded in three stages in Tasks I, IA and III: Starting with a large number of concepts in Task I, and by selective development and screening ending with a few improved coatings in Task III. The purpose of Task IB was to obtain thermophysical and thermomechanical properties for design usage. In addition, coating failure properties were assessed.

Task II was an analytic study with three objectives. The first was to assess the effects of coatings on the improvement in lifetime of industrial turbine hot section components, in particular the first stage blade. The second consisted of determining the effects of cyclic turbine operation on first row blade coating stresses. In combination with a failure criteria from Task IB, this would allow the prediction of coating durability on turbine components. The third subtask was to determine the consequences on engine performance of applying coatings to hot section

turbine components.

A final objective of the program was to gain understanding of the functioning of ceramic coatings in aggressive environments. That is, it was desired to formulate a model for the thermocyclic failure criterion and to define the corrosion mechanisms.

1.1 Coating Development

In order to endure in an industrial environment, coatings must meet two minimum criteria:

- They must be able to withstand the cyclic thermal stresses incurred during the operation of the engine.
- They must be able to resist corrosion from the products of combustion.

These criteria have guided the three staged coating development program.

In Task I, Preliminary Coating Development and Screening Tests, 58 coating candidates in five categories were assessed:

- Compositional modifications of zirconia
- Composites with zirconia
- Overcoats on zirconia base coatings
- Layers intermediate to bond and base coatings
- Ceramics other than zirconia

Most of the coatings evaluated were applied by plasma spraying, although a number of sputter deposited and ion plated layers were also investigated. The test specimens were superalloy buttons. The tops and sides were first coated with NiCrAlY bond coat (20% Cr, 10% Al, <0.5Y) and then with the various other layers. Bond coats were nominally 125 μm (5 mils) thick and ceramics 380 μm (15 mils) thick.

The specimens were threaded into a specially designed water cooled fixture having the capacity to hold 64 specimens. They were tested in a burner rig in the combustion products of three No. 2 distillate fuels: Clean, Na doped and residual fuel doped. Gas

temperatures were held at 1475K (2200°F) and the metal temperatures ranged between 1035 and 1115K (1400 and 1550°F). The thermal cycle consisted of 55 minutes of heating and 5 minutes of forced air cooling. The specimens were tested for 60 hours (cycles) and evaluated.

The results of the Task I tests were that although a number of the candidates showed potential, the best ceramic candidate was the $ZrO_2 \cdot 8Y_2O_3$ plasma sprayed to NASA Lewis specifications. This candidate had the greatest amount of development time and the best resistance to cyclic thermal stresses. However, it was known from other work that its corrosion resistance to both sodium and vanadium was limited even though failures did not occur in these screening tests. It was also shown that the best thermal shock resistance was achieved with materials containing about 20 v/o porosity. Reducing porosity below this level tended to shorten thermal stress lifetime.

Another result of the screening test evaluation was that dense overcoats retarded the penetration of contaminants into the pores of plasma sprayed coatings. Therefore, overcoats thick enough to seal off the surfaces, yet thin enough not to destroy the thermal stress resistance had the potential to extend the lifetime of $ZrO_2 \cdot 8Y_2O_3$ in corroding environments.

A final result of Task I was that wire screens which were fixed to the bond coating provided additional mechanical locking for the plasma sprayed ceramic. The wires helped the ceramic to resist crack propagation and retarded massive flaking of the ceramic.

The five coatings candidates selected for continued development in Task IA were all based on plasma sprayed zirconia. Four used this ceramic base coat with overcoats of Pt, $ZrO_2 \cdot 20Y_2O_3$, Pt graded to $ZrO_2 \cdot 20Y_2O_3$ and an AlPt alloy graded to $ZrO_2 \cdot 20Y_2O_3$. One used the zirconia coating with an Inconel 600 wire screen layer intermediate to the ceramic and bond coats.

Air cooled cylindrical superalloy test pins used in this task were coated with 125 μm (5 mils) of NiCrAlY and 380 μm (15 mils) of ceramic. The base coatings which were also sputter overcoated were

prepared at NASA Lewis and sputtering was accomplished at Battelle Pacific Northwest Laboratories. Thickness of overcoats ranged between 5 and 20 μm. The coatings with intermediate layers were prepared at Westinghouse. Sixteen specimens per test were fitted onto a cooling air manifold and cycled in and out of the burner rig using 55 minutes of heating and 5 minutes of cooling. Tests were conducted with three types of No. 2 distillate fuel: Clean, sea salt doped (ratioed to 100 ppm Na) and residual fuel doped (50 ppm V and 150 ppm Mg). Gas temperatures were maintained at 1475K (2200°F) and metal temperatures ranged between 1075 and 1170K (1475 and 1650°F).

All specimens survived 500 hours of testing in the clean fuel, indicating that they had sufficient thermal stress and oxidation resistance.

The average time to the initial failure of the baseline coatings in the residual doped fuel was 120 hours for the NASA prepared specimens and 295 hours for the Westinghouse specimens. The overcoated specimens survived 1.5 times the NASA baseline before failure initiation. The wire screen intermediate layer specimens had the same lifetimes as the baseline Westinghouse specimens. Not one of the 19 specimens tested in this fuel survived 500 hours.

The average times to initial failure of the baseline coatings in the sea salt doped fuel were 90 hours for the NASA prepared specimens and 140 hours for the Westinghouse specimens. Lifetimes of the overcoated specimens were 2.7 times that of the NASA baseline and lifetimes of coatings with screen intermediate layers were 2.2 times that of the Westinghouse baseline coatings.

The final development was performed in Task III. It was decided to undertake another iteration of development of the overcoating and intermediate layers by broadening the types investigated rather than narrowing down to the two best from Task Ia. The same NiCrAlY and zirconia base coats were used in this task. In addition, coating systems which combined overcoats with intermediate layers were assessed. As a result several factorial experiments were performed. In the first, two

types of sputtered overcoats (Pt and AlPt alloy) were combined with three types of intermediate layers (Inconel 600 wire screen, 50% ZrO_2 + 50% NiCrAlY pseudograded mixture, and none). In the second experiment, two types of plasma sprayed overcoats (fine $ZrO_2 \cdot 8Y_2O_3$ powder, and fine $ZrO_2 \cdot 8Y_2O_3$ + glass mixtures) were combined with four types of intermediate layers (Inconel 600 screen, Feltmetal, 50% $ZrO_2 \cdot 8Y_2O_3$ + 50% NiCrAlY pseudograded mixture, and none). In the latter experiment, four types of glass and two mixture ratios were used for the overcoats.

A separate set of six specimens were also prepared by physical vapor deposition methods at Airco Temescal. The compositions of the bond and ceramic coatings were nominally the same as the plasma sprayed base coatings. Both the bond coats and ceramic coatings were 125 μm (5 mils) thick.

Although improvements were made in the deposition procedures on the cylindrical specimens, they were essentially similar to those described in Task IA. The test procedures were the same. A single type of fuel was used: sea salt doped No. 2 distillate (with sea salt constituents ratioed to 100 ppm Na).

The results of the tests showed that lifetimes of plasma sprayed coatings with Inconel screen, 50% NiCrAlY + 50% $ZrO_2 \cdot 8Y_2O_3$ or no intermediate layers in combination with overcoats of plasma sprayed fine $ZrO_2 \cdot 8Y_2O_3$ or fine $ZrO_2 \cdot 8Y_2O_3$ + 20% glass had average times to failure which were 6 to 9 times that of the baseline NASA coating. Feltmetal intermediate layers and some of the plasma sprayed overcoats with 40% glass decreased lifetimes. Finally all but one of the newly developed physical vapor deposited coatings failed within the first few cycles by a thermal stress mechanism.

All of the corrosive fuel burner rig test data from Task IA and III were statistically analyzed to determine the contribution of the various components on coating system lifetime. The results are summarized in Table 1.1. Even though the mean failure times of the NASA plasma sprayed base coatings were 90 hours, no statistically significant

Table 1.1

Statistically Predicted Values of Mean Times to Initial Failure in Hours of Coating Systems as Functions of Types of Overcoats, Intermediate Layers and Base Coat Sources

Base Coat Source	Intermediate Layers	Overcoat Layer: None and Others	Fine $ZrO_2 \cdot 8Y_2O_3$	Fine $ZrO_2 \cdot 8Y_2O_3$ +25% "A" Glass	Fine $ZrO_2 \cdot 8Y_2O_3$ +20% "B" Glass	Fine $ZrO_2 8Y_2O_3$ +40% "A" Glass
NASA	None	181[a]	-	-	-	-
(W)	None and Inconel Screen	256[b]	815	568	659	48
(W)	50% $ZrO_2 \cdot 8Y_2O_3$ +50% NiCrAlY	238[b]	756	528	612	44
(W)	Feltmetal	38[b]	121	85	98	7
Airco Temescal	PVD	20	-	-	-	-

[a] Includes all sputtered deposited overcoats.

[b] Includes all other plasma sprayed overcoats than the four listed.

difference was found between this lifetime and those coatings which had sputter deposited overcoats due to the distribution of those times. All the NASA data was therefore averaged together. The best intermediate layers were either the Inconel screen or none. Again differences between these two were not significant. The best overcoat was the fine particle $ZrO_2 \cdot 8Y_2O_3$ followed by mixtures of this powder and 20-25% of two of the glass types. The best combination was 4.5 times better than the NASA baseline and sputter overcoated combined average or 9 times better than the baseline itself.

Both Feltmetal intermediate layers and overcoats with 40% of particular types of glass degraded the coating lifetime below that of the baseline. The Feltmetals debonded from the bond coats early in testing and oxidized/corroded badly. The particular glass that failed early probably had too large an expansion mismatch with the basecoat. Finally, the PVD coatings failed by thermal stress rather than corrosion.

1.2 Thermomechanical Property Screening

Thermophysical and thermomechanical properties as functions of temperature were determined for the base coating materials, $ZrO_2 \cdot 8Y_2O_3$ and NiCrAlY. These included thermal conductivities, thermal expansion coefficients, elastic moduli, shear moduli and Poisson's ratios.

In addition, coating failure properties were also assessed. These included coating stress bearing capacity parallel to the bond interface, fracture strength normal to the bond interface, the fracture toughness and the cyclic crack growth rates.

1.3 Design Analysis

Finite element analyses were performed on a coated and an uncoated first row blade of a Westinghouse 501D industrial turbine. In addition to steady state operation, the analyses were performed for several start up and shut down conditions. Temperatures and stresses were determined in the substrate metals and coatings as functions of

coating thickness, using the properties of zirconia thermal barrier coatings with NiCrAlY bond coatings.

The major improvement in metal blade life occurs due to the insulating effect of the coating. For a 380 μm (15 mil) thick coating, the average metal steady state operational temperature for constant cooling conditions is reduced by 55K (100°F). The expected effects on blade life are

- A ten-fold improvement in creep life
- A ten-fold improvement in low cycle fatigue life
- A two-fold improvement in corrosion life (assuming no additional benefit from the coating as a corrosion barrier)

In addition, the thermal barrier acts to reduce the severity of thermal stresses in the blade during temperature transients.

The effects of the turbine operating cycle on the ceramic coating stresses was also determined by the finite element analyses. During steady state operation, the tangential stresses, σ_t, directed parallel to the bond interface range between 70 and 110 MPa (10 and 16 ksi) around the periphery. For full load trip out, the σ_t ranges between 210 and 250 MPa (30 and 36 ksi), and for normal start-up the σ_t ranges between -20 and -40 MPa (-3 and -6 ksi). The tensile tangential stresses for steady state and shut-down conditions should be sufficiently high to cause the coatings to crack normal to the surface. This should not be detrimental to coating adherence. However, the compressive tangential stress during start-up induces a tensile stress normal to the bond interface, σ_n, which if sufficiently high can cause the coating to flake off. The maximum σ_n was found to be 4 MPa (0.6 ksi), and since the bond strength was found to be 16 MPa (2.3 ksi) single cycle failure is not expected.

A separate study was also performed in Task II to determine the effects of coatings of various thicknesses on engine performance. Both thermodynamic and aerodynamic analyses were made on the Westinghouse

501D engine for both single cycle and combined cycle usage. Two conditions were assessed for constant gas temperatures: first, the cooling air flow was maintained constant and the metal temperatures reduced,and second, the metal temperatures were held constant and the cooling flow was reduced. Both the single cycle and combined cycle cases showed similar results. The engine performance as measured by specific power and heat rate increased for the constant metal temperature condition and decreased for constant cooling flow condition. Thus, there will be a trade-off between performance and component lifetime improvements.

1.4 Coating Failure Mechanisms and Endurance

In order to endure turbine environments, a coating must have the capacity to resist the thermal cyclic stresses and oxidation/corrosion from the combustion gases. An understanding of the mechanisms of coating failures is essential to interpret the results of the tests and to enable coating development to proceed efficiently.

Analytic models for the thermal stress failure mechanisms based on fracture mechanics theories were developed during the program. In the usual strength theories, failure occurs when the applied stress, σ, (in this case the thermal stress) becomes equal to strength. In fracture mechanics, the stress intensity factor, K_I, is related to two independent parameters, the stress and the crack size, c. Failure occurs when K_I reaches a critical value, K_{I_c}. Thus, for a given crack size, the stress could reach a critical value, or for a given applied stress the crack could grow to a critical value. Fracture mechanics is, therefore, an improvement over strength theory since fracture mechanics can account for cyclic crack growth which can ultimately lead to failure. Models for single and multiple cycle thermal stress failures were developed.

Two sources of stresses were accounted for: residual and operational. The residual stresses arise on cool down of the coatings and substrates from elevated application temperatures. The operational

stress which leads to crack propagation parallel to the bond interface and which ultimately can cause flaking of the coating was shown to be the heat-up transient stress. Heating causes the stress in the coating directed parallel to the interface to be in compression. On cylindrical surfaces, this then generates a tensile stress normal to the bond.

Calculations of the stresses and stress intensity factors show that single cycle failures are not expected for zirconia thermal barrier coatings, as long as the residual stresses parallel to the interface are not compressive. Indeed, properly made coatings do not fail on the first few cycles. However, they may be subject to multi-cycle failures. To account for this, a multicycle failure model was developed based on fracture mechanics subcritical crack growth theory. The results of calculations for the coatings studied in this program indicated the following: for typical mean normal stresses generated in both turbine and burner rig test specimen coatings which are on the order of 4 MPa (0.6 ksi), lifetimes of greater than 10^6 cycles would be expected. However, the lifetimes are very sensitive to the value of the thermal stress. There exists uncertainties in the property values and heat transfer analysis used to calculate the stresses, and residual stresses have not been accounted for. If both of these combine to give a 50% error in stress (to 6 MPa), the lifetime would be reduced to the order of 10^3 cycles, and if the error were as great as 100% (8 MPa) only tens of cycles would cause failure. This sensitivity was demonstrated during the early coating development work on this program, where the denser, more highly thermally stressed coatings did fail very much earlier than the more compliant coatings applied later.

Related to thermal stress failure mechanisms is the oxidation of the bond coating. An oxide scale forms on these materials during elevated temperature operation at the ceramic/bond coat interface. If the scale becomes thick enough, it will be subjected to the same types of stresses as the ceramic coatings during cyclic operation. As a result, crack propagation could be easier in the scale than in the

ceramic coating. Thus, operating the bond coating at temperatures much above 1200 K (1700°F) drastically decreases coating lifetime. Chemical corrosion of the bond coat would be expected to have similar results.

Two types of corrosion attack of the ceramic coatings have been observed: mechanical and chemical. Failures of coatings subjected to combustion products rich in Na and S occur due to the penetration of Na_2SO_4 into the pores and cracks of the coatings. Cyclic freezing and thawing of this high expansion salt causes incremental mechanical crack extension to occur, until the cracks reach critical size. No evidence for chemical reactions between Na_2SO_4 and $ZrO_2 \cdot 8Y_2O_3$ have been found.

On the other hand, the combustion products of residual type fuels, which are high in V and added Mg, do chemically react. The exact corrosion mechanism is uncertain, but there is evidence that the zirconia can become destabilized. Phase transformations to monoclinic from the as-deposited tetragonal/cubic are accompanied by shear and dilational stresses and strains which cause macrocracking of the coating.

Yet another possibility is enhanced crack growth by stress corrosion mechanisms. It is well established in other materials that chemical attack in the highly stressed region of a crack tip under load promotes the growth of that crack. The effects of V and other elements on subcritical crack growth of zirconia have not been established.

1.5 Conclusions and Recommendations

Ceramic coatings on hot stage components were shown to be beneficial to either component lifetimes or overall turbine performance. The endurance of a number of the candidates in clean fuel combustion is reasonably good. These should be field tested on components of existing turbines which burn clean fuel in order to assess durability under actual operating conditions.

Considerable progress was made in this program to improve endurance of coatings subjected to lower grade fuels and/or marine environments.

However, another iteration of coating development is required to further improve corrosion/oxidation resistances of the coating systems to meet utility turbine requirements.

Quantification of the thermal functioning of coatings by combining finite element stress analyses and fracture mechanics was accomplished in this program. This work should be both continued and expanded.

Corrosion mechanisms were also qualitatively determined in the study. The corrodants cause ceramic coating failures by both mechanical and chemical means. In addition, oxidation of the bond coat at the ceramic interface can degrade coating lifetime. These mechanisms should be subjected to further study and be quantified.

It is therefore recommended that both fundamental and applied investigations of ceramic coating systems should be continued. The fundamental work is necessary to efficiently guide the development work.

2. INTRODUCTION

2.1 Background

The concept of applying ceramic coatings on heat engine components to provide oxidation and corrosion protection for the substrate alloys has been in existence for some time [refs. 1- 3]. As originally conceived, the protection was dependent on the absolute integrity of the ceramic layer. Failures of metal components occurred through flaws and cracks in the as-deposited coatings or to those generated during thermal cycling. Metal coatings which depend on the formation of oxide scales to act as diffusion barriers have also been the subject of on-going investigations [refs. 2- 3]. Although they have been quite successful, they also have limited usefulness in the presence of certain corrosion products [ref. 4]. The use of the insulation properties of ceramics for heat protection was also considered early [refs. 2, 3, 5, 6].

Recently, developmental efforts have been directed toward combining metal and ceramic coatings into a layered composite which takes advantage of the best properties of each of the constituents [refs. 7- 8]. A thin, relatively ductile metal coating is applied on the substrate alloy, and a usually slightly thicker ceramic coating is applied on top of it. Oxidation and corrosion protection of this thermal barrier coating system is mainly provided by the metal component, although this report will present evidence that the ceramic contributes significantly. The primary function of the ceramic is as a thermal insulator, and thus its absolute integrity is not required. Other than having a low thermal conductivity, the important property of the ceramic layer is thermal stress resistance. Thus, the ceramic is typically applied by plasma spraying methods with large fractions of pores and cracks to give it tolerance to thermal transients and to thermal expansion differences between it and the substrate alloy.

Contemporary thermal barrier coatings have proven capability for operating in clean oxidizing environments such as the combustion products of natural gas, distilled oils and kerosenes. They are currently being considered for use in industrial/utility class combustion turbines where fuels and environments may not be ideal. Depending on market prices and availability, fuels with higher impurity contents could be considered. Site location of the engine could allow the airborne injestion of harmful contaminants. In addition, future fuels will potentially consist of coal derived products whose contaminant levels could be quite variable depending on the source of the coal and the process used.

Investigations of present thermal barrier coatings indicate that their functioning in contaminated combustion products is marginal [eg, refs. 9-10]. The ceramic layers flake and spall when tested with simulated residual fuels or in accelerated marine environments. Therefore, to be acceptable for industrial usage with a wide spectrum of fuels, improvements in the coating systems are required.

2.2 Program Objectives

The major objective of this program was to develop ceramic coatings which increase industrial/utility gas turbine hot section durability with heavy emphasis on operation with lower grade petroleum base fuels and coal derived fuels. The second objective was to take advantage of the insulative properties of ceramic coatings on turbine airfoils and combustors without incurring a meaningful penalty in obtaining the primary objective.

2.3 Technical Plan

The program plan to accomplish the goals consisted of five tasks:

Task I: Preliminary Coating Development and Screening Tests

Task IA: Burner Rig Testing

Task IB: Thermomechanical Property Evaluation
Task II: Preliminary Coating Design Criteria
Task III: Coating Improvement and Endurance Testing

Coating development and evaluation were carried out in Tasks I, IA and III. The approach used was to initially start with a large number of candidates using a diverse variety of concepts to ensure that the state-of-the-art would be covered. Via screening tests, these were first to be reduced to five and then to two candidates in the final stage. In actuality, the number of candidates in Task III was broadened to include several new candidates which evolved during the progress of the program. The candidates, test procedures and results of this work are presented in the Coating Development section.

Two types of properties of the coatings were evaluated in Task IB, thermophysical and mechanical. Thermophysical properties are those required for design, thermal analysis and stress analysis, and include thermal conductivity, thermal expansion and elastic properties over the operational temperature range. Two types of mechanical or failure properties were assessed: coating strengths (both parallel and perpendicular to the bond interface) and fracture toughness (both fast fracture and cyclic subcritical crack growth). The procedures and results are presented in the Coating Properties section.

Thermal, stress and aerothermodynamic analyses were performed in Task II. Assessments were made of the effects of coatings on the lifetimes of an industrial first row turbine blade, of the effects of the turbine operational cycle on the coating stresses, and of the effects of coatings on the power and efficiency of the engine. The results are presented in the Coating Design Criteria section.

The final section of the report, Coating Endurance, assesses the various coating failure mechanisms. An analysis of cyclic thermal stress failures based on fracture mechanics is presented. Based on this and the data gathered in the program, lifetime predictions are made. The corrosion mechanisms encountered during the program are also discussed.

3.0 COATING DEVELOPMENT

The development of advanced coatings for industrial/utility gas turbine components proceeded in three stages. The intent of the first stage, Preliminary Coating Development and Screening Tests (Task I) was to survey a large variety of coating candidates. A total of 58 candidates in five categories were surveyed. The categories consisted of 1) compositional modifications of zirconia, 2) composites with zirconia, 3) overcoats on zirconia, 4) intermediate layers between bond and ceramic coatings and 5) other ceramics. These coatings were assessed on button specimens in a thermal cyclic burner rig test burning three types of fuels.

The five most promising candidates from Task I were selected for further development and evaluation in the second stage of coating development: Burner Rig Testing (Task IA). The five candidates were chosen to be improvements on the baseline NASA plasma sprayed zirconia coating. The improved versions consisted of this baseline coating with four sputter deposited seal off overcoats and with one wire screen layer intermediate to the bond and ceramic coatings. The coatings were assessed on air cooled cylindrical specimens in the thermal cyclic burner rig in the combustion products of three fuels.

The concepts of intermediate layers and overcoats used with zirconia basecoats were combined in the final development stage, Coating Improvement and Endurance Testing (Task III). The types of overcoats and intermediate layers were actually broadened to include coatings other than those tested in Task IA. In addition, newly developed physical vapor deposited coatings were included in the test series. The coatings were also assessed on air cooled cylindrical specimens in the thermal cyclic burner rig burning a single type of highly corrosive fuel.

The coating materials, equipment test procedures and results will be detailed in the following section.

3.1 Materials

3.1.1 Substrate Alloys

The substrate alloys for the program were selected to be representative of current industrial turbine practice. The Ni-based blade alloy, Udimet 720, was a wrought material. The Co-base vane alloy, ECY-768 was used in the as cast condition.

3.1.2 Bond Coating

The bond coating composition was maintained constant throughout the program in order to eliminate it as a variable. The selection of NiCrAlY alloy, with a nominal composition of 20 w/o Cr, 10 w/o Al, <0.5 w/o Y and the balance Ni, was based on NASA data (ref.11). It was purchased[(a)] in powder form (-200 + 325 mesh and -270 mesh + 10 μm) for the plasma spraying process which was used for most of the coatings studied. The remaining materials were hot isostatically pressed sputter deposition targets and physical vapor deposition melts.

3.1.3 Ceramic Coatings

Although a large variety of ceramic materials were initially investigated, most of the later work utilized a partially stabilized zirconia (PSZ) having an 8 w/o yttria content ($ZrO_2 \cdot 8Y_2O_3$)[(b)]. Two particle sizes were investigated, a coarser grade (-200 + 325 mesh) and a finer grade (-270 mesh + 10 μm). The coarser grade in conjunction with the similar sized NiCrAlY powder served as the baseline duplex coating when produced to the NASA specification (ref.12). The finer grade powder was purchased using the specifications of a coating vendor who was supposed to apply the coatings in the later tasks.

In the following text, multicomponent coatings separated by plus (+)

(a) Alloy Metals, Inc., Troy, MI

(b) Zircoa Products, Corning Glass Works, Solon, OH

signs refer to mechanical or phase mixtures, and those separated by slashes (/) refer to distinct layers with the outermost layer written first. Alloy, stabilizer or composite mixture contents are given in weight percents. In Task I, Preliminary Coating Development, the $ZrO_2 \cdot 8Y_2O_3$ used was primarily the fine Zircoa grade. Some baseline coarse grade coatings were also assessed. In the later two development stages, the coarse grade $ZrO_2 \cdot 8Y_2O_3$ was used exclusively, except where noted.

The coatings assessed in Task I, Preliminary Coating Development are given in Table 3.1. The materials were obtained from a variety of sources and for the most part had a variety of particle sizes. Except where noted, the coatings were applied by plasma spraying. Insufficient time was available to develop optimum particle sizes and plasma spray parameters for each type. Therefore, much of the results which will be reported could be attributed to deposition rather than compositional characteristics.

The coatings assessed in Task IA, Burner Rig Tests, are presented in Table 3.2. In group A, the NiCrAlY bond coatings and zirconia base-coats were applied by the NASA Lewis Research Center. The specimens were sent to Battelle Pacific Northwest Laboratories for the application of sputter deposited overcoats: Group B was totally prepared at Westinghouse. In one set, Inconel wire screen was spot welded onto the NiCrAlY prior to the application of the ceramic coating. In all cases, the coarse mesh Zircoa powder was used, and NASA specified spray parameters were used.

The coatings evaluated in the final stage of coating development, Task III - Coating Improvement and Endurance Testing, are presented in Table 3.3. The original intent of the program was to reduce the number of coatings tested in Task III to a maximum of two. However, as testing in Task IA progressed, it became evident that another iteration of coating development was required. Therefore, two factorial experiments were established to investigate a broader spectrum of overcoats and

TABLE 3.1

CERAMIC COATING MATERIALS EVALUATED IN TASK I - PRELIMINARY COATING DEVELOPMENT AND SCREENING TESTS

A. Zirconia Compositional Variations		
$ZrO_2 \cdot 2.5Y_2O_3$	$ZrO_2 \cdot 13CeO_2$	$ZrO_2 \cdot 15Y_2O_3 \cdot 10Ta_2O_5$
$ZrO_2 \cdot 5.5Y_2O_3$	$ZrO_2 \cdot 24CeO_2$	$ZrO_2 \cdot 20Y_2O_3 \cdot 10Ta_2O_5$
$ZrO_2 \cdot 6Y_2O_3$	$ZrO_2 \cdot 58CeO_2$	
$ZrO_2 \cdot 8Y_2O_3$	$ZrO_2 \cdot 81CeO_2$	
$ZrO_2 \cdot 10.5Y_2O_3$		
$ZrO_2 \cdot 14Y_2O_3$		
$ZrO_2 \cdot 25Y_2O_3$		
$ZrO_2 \cdot 30Y_2O_3$		
$ZrO_2 \cdot 38Y_2O_3$		
B. Composites with Zirconia		
90% $ZrO_2 \cdot 8Y_2O_3$ + 10% ZrO_2	99% $ZrO_2 \cdot 8Y_2O_3$ + 1% Pt	75% $ZrO_2 \cdot 8Y_2O_3$ + 25% MgO
85% $ZrO_2 \cdot 8Y_2O_3$ + 15% ZrO_2	98% $ZrO_2 \cdot 8Y_2O_3$ + 2% Pt	ZrO_2 + Al_2O_3 eutectic
80% $ZrO_2 \cdot 8Y_2O_3$ + 20% ZrO_2	95% $ZrO_2 \cdot 8Y_2O_3$ + 5% Pt	ZrO_2 + YVO_4
		$ZrO_2 \cdot 8Y_2O_3$ + $3Al_2O_3 \cdot SiO_2$
85% $ZrO_2 \cdot 8Y_2O_3$ + 15% ZrO_2 fibers		$ZrO_2 \cdot 20Y_2O_3$ (Multilayered SD[a])/NiCrAlY
85% $ZrO_2 \cdot 8Y_2O_3$ + 15% Al_2O_3 fibers		$ZrO_2 \cdot 20Y_2O_3$ (Multilayered SD)/NiCrAlY
C. Overcoats on Zirconia		
$AlPt_3/ZrO_2 \cdot 8Y_2O_3$	$ZrO_2 \cdot 8Y_2O_3$ (SD)/$ZrO_2 \cdot 8Y_2O_3$	
$ZrPt_3/ZrO_2 \cdot 8Y_2O_3$		
$HfPt_3/ZrO_2 \cdot 8Y_2O_3$	Pt (IP[b])/$ZrO_2 \cdot 8Y_2O_3$	
$TaPt_3/ZrO_2 \cdot 8Y_2O_3$		
$TiPt_3/ZrO_2 \cdot 8Y_2O_3$	Glass (FM[c])/$ZrO_2 \cdot 8Y_2O_3$	
D. Layers intermediate to Zirconia and Bond Coating		
$ZrO_2 \cdot 8Y_2O_3$/Cr	$ZrO_2 \cdot 8Y_2O_3/ZrO_2 \cdot 8Y_2O_3$ (SD)	$ZrO_2 \cdot 8Y_2O_3$/Pt screen
$ZrO_2 \cdot 8Y_2O_3$/Mo		$ZrO_2 \cdot 8Y_2O_3$/In 600 40 mesh screen
$ZrO_2 \cdot 8Y_2O_3$/Ti		$ZrO_2 \cdot 8Y_2O_3$/In 60 80 mesh screen
$ZrO_2 \cdot 8Y_2O_3$/Pt (IP)		
E. Other Ceramics		
$La_{.95}Mg_{.05}Cr_{.5}Al_{.5}O_3$	$CaSO_4$	HfO_2
$La_{.95}Sr_{.05}CrO_3$	CeO_2	TiB_2
Cr_2O_3	$ZrSiO_4$	$3Al_2O_3 \cdot 2SiO_2$
MgO + $MgCr_2O_4$ eutectic	TiO_2	$AlPt_3$

a) SD = sputter deposited

b) IP = ion plated

c) FM = frit melted

d) Nominal thickness of plasma sprayed coatings were 130 μm (5 mils) of NiCrAlY and 380 μm (15 mils) of ceramic and 50 μm (2 mils) of overcoat.

TABLE 3.2

CERAMIC COATING MATERIALS EVALUATED
IN TASK IA - BURNER RIG TESTING

A.	Zirconia Plasma sprayed[a] at NASA-Lewis Research Center and overcoats sputter deposited[b] at Battelle Pacific Northwest Laboratories
	Baseline $ZrO_2 \cdot 8Y_2O_3$ Pt (SD[c])/$ZrO_2 \cdot 8Y_2O_3$ $ZrO_2 \cdot 20Y_2O_3$(SD)/$ZrO_2 \cdot 8Y_2O_3$ Pt graded to $ZrO_2 \cdot 20Y_2O_3$ (SD)/$ZrO_2 \cdot 8Y_2O_3$ AlPt alloy graded to $ZrO_2 \cdot 20Y_2O_3$ (SD)/$ZrO_2 \cdot 8Y_2O_3$
B.	Zirconia Plasma sprayed[a] at Westinghouse R&D Center
	Baseline $ZrO_2 \cdot 8Y_2O_3$ $ZrO_2 \cdot 8Y_2O_3$/Inconel 600 Screen

a) 130 μm (5 mils) nominal thickness NiCrAlY + 380 μm (15 mils) nominal thickness $ZrO_2 \cdot 8Y_2O_3$.

b) Two nominal thicknesses applied:

(5 μm) 0.2 mils
(15 μm) 0.6 mils

c) SD = sputter deposited

TABLE 3.3

COATINGS EVALUATED IN TASK III - COATING IMPROVEMENT AND ENDURANCE TESTING

Coating Layer	Description	Number of Variables	
A. Zirconia coatings with intermediate layers and sputter deposited overcoats			
Top Coat	Sputter Deposited, 19 μm ∿.75 mils thick Types: a) Pt b) AlPt	2	
Undercoat	Plasma sprayed $ZrO_2 \cdot 8Y_2O_3$ (-270 mesh + 10 μm), Surface Ground, 51 - 130 μm 2-5 mils thick	1	
Base Coat	Plasma sprayed $ZrO_2 \cdot 8Y_2O_3$ (-200 + 325 mesh)	1	
Intermediate Layers/ Bond Coat	a) NiCrAlY/Fine Mesh Inconel Screen/NiCr b) NiCrAlY/Coarse Mesh Inconel Screen/NiCr c) 50 v/o $ZrO_2 \cdot 8Y_2O_3$ + 50 v/o NiCrAlY/NiCrAlY d) NiCrAlY only	X2 X2 X2 X1	7
		TOTAL NUMBER 14	
B. Zirconia coatings with intermediate layers and plasma sprayed overcoats			
Top Coat	Plasma sprayed $ZrO_2 \cdot 8Y_2O_3$ (-270 mesh + 10 μm) + glass mixtures, 51 - 76 μm 2-3 mils thick Glass Types: a) EK5 b) EK7 c) 3831 d) 5301 Mixture Ratios: a) 0 v/o Glass b) 25 v/o Glass c) 50 v/o Glass	4 3	12
Base Coat	Plasma sprayed $ZrO_2 \cdot 8Y_2O_3$ (-200 + 325 mesh)		
Intermediate Layers/Bond Coat	a) NiCrAlY/Inconel Screen/NiCr b) NiCrAlY/DH242 Feltmetal/NiCr c) 50 v/o $ZrO_2 \cdot 8Y_2O_3$ + 50 v/o NiCrAlY/NiCrAlY d) NiCrAlY only	2-4	
		TOTAL NUMBER 28	
C. Physical vapor deposition coatings			
Base Coat	Physical vapor deposited $ZrO_2 \cdot 8Y_2O_3$	X6=6	
Bond Coat	Physical vapor deposited NiCrAlY	1	
		TOTAL NUMBER 6	

intermediate layers. In the first experiment, two types of sputter deposited overcoats were combined with four types of intermediate layers (Group A in Table 3.3). In the second, four types of plasma sprayed fine zirconia plus glass mixtures were combined with four types of intermediate layers. The bond coats, intermediate layers, and plasma sprayed layers were all applied at Westinghouse. The sputter deposited layers were applied by Battelle.

A third set of physical vapor deposited coatings[(c)] were also evaluated. These were duplex coatings of the same nominal composition as the NASA basecoat. Since this was the first set of coatings produced for burner rig evaluation, and since deposition parameters had not been previously established, the coating structures produced were quite variable.

3.1.4 Overcoats

Thin, relatively dense overcoats were applied over numerous basecoats listed in Tables 3.1, 3.2 and 3.3 in order to provide seal off layers to retard penetration of contaminants. These varied in composition and structure from metals (Pt and AlPt alloys) to intermetallic compounds ($AlPt_3$, $ZrPt_3$, etc.) to ceramics ($ZrO_2 \cdot 8Y_2O_3$, $ZrO_2 \cdot 20Y_2O_3$) to glasses to ceramic + glass mixtures. As indicated on the tables, several deposition methods were assessed, with sputter deposition and plasma spraying being the primary ones.

Thicknesses of these overcoats also varied. The thinnest coatings were applied by sputter deposition and ion plating where the coatings varied between 2 and 40 μm (0.1 and 1.5 mils). Plasma sprayed overcoats required thicker applications between 50 and 75 μm (2 and 3 mils).

(c) prepared by Airco Temescal, Berkeley, CA

3.1.5 Intermediate Layers

A number of layers intermediate to the bond and ceramic coatings were also assessed. As shown in Tables 3.1, 3.2 and 3.3 these included two mesh sizes of Inconel 600 wire screens: a coarse mesh, 3150 x 3150 per meter (80 x 80 per inch), and a fine mesh, 6300 x 5510 per meter (160 x 140 per inch). The wire size in each case was 100 μm (4 mils).

Two thicknesses of Feltmetal[(d)] were also attempted: 175 and 250 μm (7 and 10 mils). Both were composed of 25 μm (1 mil) thick DH-242 Ni-Cr alloy.

A pseudograded zone was also used. This consisted of a plasma sprayed layer of a 50 v/o NiCrAlY + 50 v/o zirconia mixture. Finally other thin metallic and ceramic layers shown in Table 3.1 were also attempted.

3.2 Equipment

3.2.1 Coating Application

3.2.1.1 Plasma Spray Deposition. The primary coating application method used was plasma spraying. Both Westinghouse and NASA-Lewis used similar equipment produced by Plasmadyne[(e)]. The Westinghouse Model SG-1B spray gun was backed by a 40 kW power supply, Model PS-61M and two Roto-feed Hoppers, Models 1000A and 1224A. Rotating tables with variable speed motors were used to aid uniform coating of specimens with cylindrical symmetry. At NASA, the gun is usually hand held during the spraying application. Westinghouse dedicated a small machine lathe to the coating operation. The gun was fixed to the lathe table and was uniformly semi-automatically translated by the lathe screw thread. At the same time the gun distance remained constant.

(d) Technetics Div., Brunswick Corp., Deland, FL

(e) Plasmadyne Div., Goetel Inc., Santa Ana, CA

3.2.1.2 Sputter Deposition. Sputter deposited coatings were applied at Battelle[f] with equipment of their own design and construction. It consists of a large vacuum chamber with seven rotationally motorized side feedthroughs to which seven specimens can be attached and coated at one time. Two sputter targets, one located above and one below the specimens can be used either simultaneously or separately. The equipment has capability of being operated in dc-triode, rf-diode or rf-triode modes. Details of this equipment are described elsewhere (ref.13).

3.2.1.3 Physical Vapor Deposition. Physical vapor deposited coatings were applied at Airco Temescal[g] with equipment of their own design and construction. Details of the equipment are described elsewhere (ref.14).

3.2.2 Test Equipment

3.2.2.1 Burner Rig Test Furnaces. Burner rig testing was accomplished with two 41,000 J/S (140,000 Btu/hr) furnaces, schematically shown in Figure 3.1. The stainless steel furnace shell sits on a welded steel frame and is lined with refractory brick. Two 20,500 J/S (70,000 Btu/hr) oil burners are located at one end of the shell. Each fires approximately at 45° to the centerline of the furnace into the 30 cm (12 inch) wide by 20 cm (8 inch) high main duct. Gas temperatures are regulated by metering both fuel and air to the burners. The hot gases pass through the test section and out the chimney duct. An auxiliary duct located at the furnace top between the test section and the chimney duct is provided for tests in which specimen cooling air must be dumped. This duct is otherwise plugged.

---

[f] Dr. J. W. Patten, Battelle Pacific Northwest Laboratories, Richland, WA

[g] Dr. E. Demaray, Airco Temescal-Turbine Coating Group, Berkeley, CA

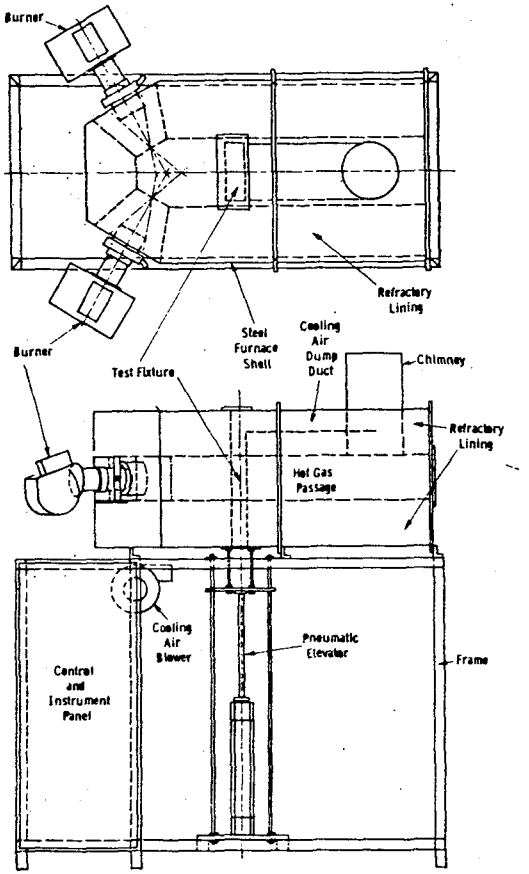

Figure 3.1 Schematic of 41000 J/s (140000 BTU/hr) burner rig test furnace

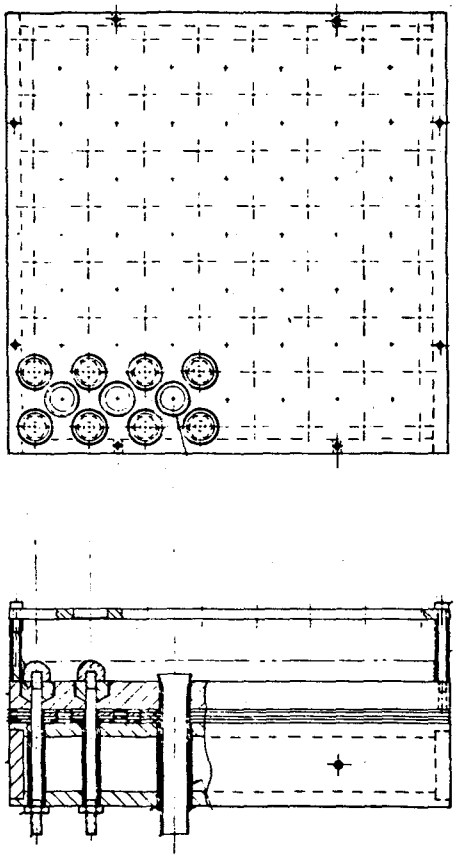

Figure 3.2 - Water cooled button specimen test fixture

The test section is bolted to the top of a pneumatic elevator, which can be rapidly raised or lowered under the control of a pair of electro-mechanical timers. The cycle is started after preheating the furnace for several hours by lifting the test section into the gas stream. At the completion of the heating portion of the cycle, the section is lowered into an ambient temperature air stream provided by a squirrel cage blower located under the furnace shell.

Specimen temperatures, measured by thermocouples inserted into them, are continuously monitored by a multipoint recorder. Gas temperature, measured by a thermocouple situated in the gas stream several centimeters in front of the test section, is also recorded. An additional thermocouple in the gas stream is provided for an over-temperature trip safety device.

A special 8 x 8 array button test fixture was designed and constructed for the Task I screening tests, as shown in Figure 3.2. The combustion gas flows through the orifice plate and forms jets which impinge on the coated specimen buttons and then via the discharge tubes through the heat sink. The buttons are fastened to the heat sink with hollow studs, which permit the introduction of thermocouples through the rear to the buttons. The heat sink is designed to provide a good approximation to axial heat flow. The heat sink plate is separated from the brass water coolant chamber by perforated steel plates. These plates provide the necessary thermal impedance to maintain the buttons at the desired temperature and still permit a gradient to exist across the thermal barrier.

Burner rig exposure tests of Tasks IA and III were also run in two 140,000 Btu/hr furnaces, but used cylindrical specimens. The only changes required for this test series was the specimen holding fixture that sits on top of the pneumatic elevator. As shown in Figure 3.3, this consists of stainless steel box which acts as the cooling air manifold. The high pressure air is brought in through the bottom and exits through two staggered rows of eight holes each at the top. Sixteen test pins

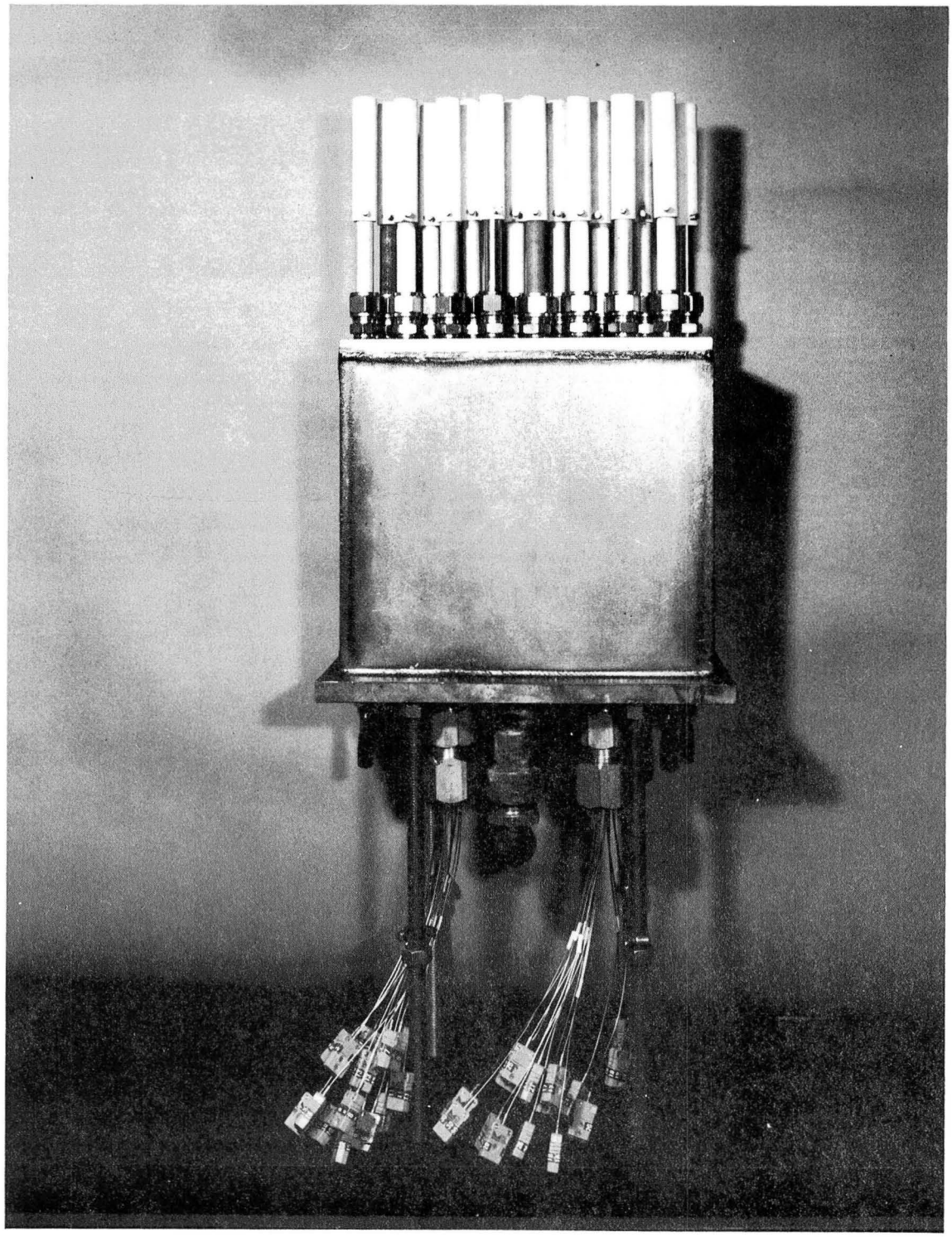

Figure 3.3 - Air cooled cylindrical specimen test fixture

held in stainless steel ferruled tubing fittings are threaded into these holes. The air flow is then through the 6.4 mm (0.25 inch) diameter axial bores of the test pins into the bores of 10 cm (4 inch) long Inconel 601 chimneys at the tops of each pin which finally exits into the cooling air dump duct of the furnace. The purpose of the chimneys is to carry the cooling air sufficiently far away so as not to effect the hot gas flow over the ceramic coated surfaces. The air flow in each test pin is moderated by conical inserts at the bottom of each pin. The conical inserts are attached to micrometer adjustment threads located at the bottom of the manifold chamber. Screwing these in causes the cone to reduce the air flow area at the bottom of the pin.

Two thermocouples are inserted into each pin. The first measures the maximum specimen temperature near the top of the pin on the side facing the hot gas flow. The second measures the minimum specimen temperature at the bottom of the specimen away from the gas flow. Maximum operating temperature in each pin is controlled by regulating the air flow through it.

3.2.3 Analysis

Pre- and post-test analysis of specimens were accomplished with a variety of equipment including: light microscopes and metallographs, scanning electron microscopes (SEM) an electron microprobe (EM), X-ray diffraction equipment, and spectrographic chemical analyzers.

3.3 Experimental Procedures

3.3.1 Test Specimens

Two types of specimens were machined from the substrate alloy materials: buttons for Task I - Coating Development, and cylinders for both Task IA - Burner Rig Exposure and Task III - Coating Improvement.

3.3.1.1 Button Specimens. The largest fraction of button specimens were of a hemispherical dome type. It was designed to maximize the radii of curvature and minimize stress concentrations in the coating. The buttons measured 12.7 mm (0.5 inches) in diameter and were 9.5 mm (0.375 inches) in height. The top surface was radiused 6.4 mm (0.25 inches). A 10-32 female thread was tapped into the bottom (flat) surface to a depth of 4.8 mm (0.188 inches).

A few specimens which were to test the effects of wire screen intermediate layers were machined with flat tops. These also measured 12.7 mm in diameter and were 9.5 mm high. The top corners were radiused 1.6 mm (0.063 inches), leaving a 9.5 mm diameter flat on top. The bottom surface received the same female threading.

3.3.1.2 Cylindrical Specimens. Cylindrical specimens measuring 12.7 mm (0.5 inch) in diameter by 76.2 mm (3 inches) long with a 6.4 mm (0.25 inch) diameter axial cooling bore hole were machined from the alloys. Two thermocouple holes were also machined parallel to the axis from the bottom of the specimen. These two 1.1 mm (0.043 inch) diameter holes were drilled 180° apart on a 9.5 mm (0.375 inch) hole circle. The leading edge hole was drilled to a depth of 64 mm (2.5 inches) and the trailing edge hole to 25 mm (1.0 inch).

After machining, all Udimet 720 specimens were heat treated as follows: 1440K (2135°F) for 4 hours solution treatment and then furnace cooled; and 1350K (1975°F) for 4 hours aging and then furnace cooled. The ECY-768 was used in the as cast condition.

3.3.2 Coatings

3.3.2.1 Plasma Spray Coatings. The majority of coatings throughout the program were applied by plasma spraying. Prior to coating all specimens were ultrasonically cleaned with triclorethane and then grit blasted with aluminum oxide grain (Carborundum Blastite, Specification 36). The bond coat was applied using the specification given in Table 3.4 to a

TABLE 3.4

NASA LEWIS RESEARCH CENTER SPECIFICATIONS
FOR PLASMA SPRAYING OF BASE COATING (REF. 2)

Parameter	Bond Coating	Zirconia Coating
Stand off Distance	12.7 cm (5 in.)	7.6 cm (3 in.)
Arc Potential	31 V	33 V
Arc Current	400A	600A
Arc Gas Flow Rate	4.3×10^{-4} m^3s^{-1} (55 CFH)	4.7×10^{-4} m^3s^{-1} (60 CFH)
Powder Gas Flow Rate	8.7×10^{-5} m^3s^{-1} (11 CFH)	9.4×10^{-5} m^3s^{-1} (12 CFH)
Powder Feed Rate, Hopper Rotational Speed	1.1 rpm	2.4 rpm
Feed Port	rear	rear
Coating Build-up Rate	(1 mil/pass)	(1 mil/pass)

thickness of 127 μm (5 mils).

In cases where intermediate layers were used, they were applied next. Some were also plasma sprayed: Cr, Mo and Ti in Task I and 50% NiCrAlY + 50% $ZrO_2 \cdot 8Y_2O_3$ powder mixture in Task III. One was sputter deposited: $ZrO_2 \cdot 8Y_2O_3$; and one ion plated: Pt in Task I. Others were spot welded: Pt screen and Inconel 600 screens in Task I, and Inconel 600 screens in Task IA. Finally, a number were vacuum brazed with Nicrobraze 500: Feltmetals and Inconel 600 screens in Task III. The Inconel screens and Feltmetals in Tasks IA and III received an additional 50 μm (2 mils) of bond coat prior to the application of the ceramic coatings.

Ceramic coatings were applied either over the bond coating or the intermediate layer. In Task I, a variety of coating parameters had to be used since each powder other than the $ZrO_2 \cdot 8Y_2O_3$ had unique characteristics. The parameters were adjusted to achieve coating adhesion but were by no means optimized due to time limitations.

In Tasks IA and Task III the ceramic coating powders were chosen to be the coarse variety of $ZrO_2 \cdot 8Y_2O_3$. The spraying parameters used for these coatings are also listed in Table 3.4. In Task IA a majority of these were applied at NASA-Lewis. The remaining specimens and those used in Task III were applied at Westinghouse.

In some cases, overcoats were applied on the porous ceramic basecoats. Plasma spraying was used for the MPt_3 intermetallics in Task I, and for fine $ZrO_2 \cdot 8Y_2O_3$ and mixtures of fine $ZrO_2 \cdot 8Y_2O_3$ + glass in Task III. The basecoats were allowed to cool before the intermetallics were sprayed. The Task III coatings and overcoatings were continuously applied, ie., two powder feed hoppers were connected to the plasma spray gun and were switched during the coating operation. After the plasma spraying operation of the $ZrO_2 \cdot 8Y_2O_3$ + glass was completed, the specimens were heated to allow the glass to melt and better fill the voids.

Other than the ion plating of Pt and the melting of a glass powder

frit in Task I, most of the other overcoats were applied by sputter deposition. In Tasks IA and III this was performed at Battelle. Prior to shipping the specimens for overcoating, half of the specimens in Task IA were hand polished on a lathe with SiC polishing paper, starting with 180 grit and finishing with 600 grit. Microscopic examination later proved that some regions of the cylindrical surfaces remained rough. For Task III, the coarse mesh basecoat was oversprayed with fine mesh $ZrO_2 \cdot 8Y_2O_3$ by switching the hoppers during the operation. The plasma sprayed coating thickness was increased by slightly less than 100 μm (4 mils) and then diamond ground off to final dimensions in a centered grinder using a 325 mesh wheel. Sputtering was performed on top of this smoother, more uniform surface.

In Task I, the button specimens were plasma spray coated by threading a rod into the specimen back, chucking into a variable speed motor drive and rotating it at approximately 60 rpm. The gun was hand held and rotated in an arc at the approximate stand off distance during the spraying operation. The bottom of the specimens were covered to prevent coating of this region since it was to be in contact with a cooled fixture during testing. The hand held operation did cause variability in coating thickness on both individual specimens and between specimens.

The total lengths of the cylindrical specimens were bond coated, but only the centrally located 51 mm (2 in.) lengths of the specimens were coated with ceramic. Also, to reduce stress in the regions where the coating ended, the coating thicknesses were tapered over the last 3 mm (0.12 in.).

The specimens in Task IA coated at NASA were clamped vertically on a motorized turntable. The plasma gun was hand held and the spray translated up and down the specimen during the coating operations. The uniformity was dependent on the skill of the operator.

The cylindrical specimens sprayed by Westinghouse were chucked horizontally in a modified machine lathe. The gun was fixtured to the translation table at a constant distance from the specimen. During the

coating operation, the specimen was rotated and the gun translated back and forth at a uniform rate parallel to the specimen axis by the lathe's screw thread. In this manner, the coating thickness was kept uniform, both along the lengths of individual specimens and between specimens.

Two hoppers were also connected to the plasma spray gun. By switching hopper feeds, coating constitution could be changed without a time lapse.

3.3.2.2 Sputter Deposited Coatings. Two types of sputter deposited coatings were prepared by Battelle. In Task I, multilayered ceramic/metal coatings were applied to button specimens. In Tasks IA and III several types of overcoats were applied on plasma sprayed ceramic base coatings.

Two targets were used to apply the multilayered coatings: a $ZrO_2 \cdot 20Y_2O_3$ which had been used previously and a NiCrAlY (NASA specification) made specifically for this program. The procedures used were similar to those used previously (ref.13). The substrate was first bombardment etched immediately prior to sputter deposition to improve coating adherence. Then nine alternating layers of NiCrAlY and $ZrO_2 \cdot 20Y_2O_3$ were deposited on the rotating button specimens, yielding five metal and four ceramic layers. On five of the specimens, the transition between the ceramic and metal layers were sharp. On the other five produced, the compositions in the layers were graded from metal to ceramic.

Four types of overcoats were sputter deposited on the plasma sprayed $ZrO_2 \cdot 8Y_2O_3$ basecoatings in Task IA. Again, the plasma sprayed base coating was bombardment etched prior to sputtering. Seven specimens were rotationally coated in each run. At the time the coatings were being applied, no experience was available with regard to the optimum thickness of the overcoat. They were required to be thick enough to cover the surface pores in the basecoat, but not overly thick so as to contribute to thermal stress failures. Two thickness ranges were

selected for trial: 5 to 8 μm (0.2 to 0.3 mils) and 15 to 20 μm (0.6 to 0.75 mils). A total of eight successful runs were made.

For Task III, two types of overcoats were applied on the plasma sprayed base coating. Since the thicker coatings had proven to be more effective in Task IA, a nominal overcoating thickness of 20 μm (0.75 mils) was selected. In actuality, the Pt was thicker at 31 μm (1.2 mils) and the AlPt thinner at 14 μm (0.55 mils).

3.3.2.3 Physical Vapor Deposition. Six specimens were prepared by Airco Temescal for Task III on newly built PVD equipment. The specimens also represented some of the early efforts in producing ceramic coatings. This in conjunction with debugging and ongoing modifications of the equipment resulted in no standard procedure being used. Details of the process are presented elsewhere (ref. 14). In general, however, the procedure consisted of glass bead peening, chemical cleaning and degreasing of the substrate, followed by the PVD application of the NiCrAlY (NASA specification). The substrate was preheated, the bond coat material electron beam melted and the parts were coated overall to a thickness of 127 μm (5 mils) while rotating. The NiCrAlY was again bead peened, cleaned and degreased. After masking off the ends, the specimens were fitted into the holder. Prior to coating some of the specimens were preheated by radiation from the $ZrO_2 \cdot 8Y_2O_3$ electron beam heated melt, others were preheated by resistance heaters and some were given no preheat. The electron beam current was ramped up and the parts were then rotationally coated for 20 to 48 minutes to give a nominal 127 μm (5 mil) ceramic coating. Afterwards they were slowly cooled for 15 to 20 hours.

3.3.3 Testing

3.3.3.1 Task I - Preliminary Coating Development and Screening Tests. Six test runs were performed in Task I. The first three screening tests were run with clean No. 2 distillate, the next two burned No. 2 distillate

doped with 5 ppm Na, 2 ppm V, 10 ppm Ca, 5 ppm Pb and 5000 ppm S, and the final run with No. 2 distillate doped with 50 ppm V, 150 ppm Mg, 1 ppm Na, 15 ppm Pb, 0.5 ppm Ca and 5000 ppm S. The gas temperatures were held at a nominal 1475K (2200°F) for all runs. The nominal metal temperatures for the clean fuel and the Na doped fuel were between 1090K (1500°F) and 1115K (1550°F) and for the V doped fuel run 1035K (1400°F).

The general test procedure consisted of randomly bolting pairs of button specimens to the water cooled test fixture. Eight to nine thermocouples were inserted into the backs of specimens distributed throughout the array so as to sample the temperatures at the various locations. The fixture was bolted to the pneumatic elevator, water hoses were connected and thermocouples plugged into the recorder. After preheating the furnace, the elevator raised the fixture into the test channel for 55 minutes of heating, and then withdrew it for 5 minutes of forced air cooling. Each run consisted of nominally 60 thermal cycles. The test fixture was removed from the furnace every 20 cycles in order to allow closer examination of the specimens.

3.3.3.2 Task IA - Burner Rig Testing. Three 500 hour burner rig tests were run in Task IA: one clean No. 2 distillate test, one test burning No. 2 distillate doped with 50 ppm V, 150 ppm Mg, 1 ppm Na, 15 ppm Pb, 0.5 ppm Ca and 5000 ppm S, and one burning No. 2 distillate doped with 100 ppm Na, 10 ppm Mg, 180 ppm Cl, 3 ppm K, 4 ppm Ca and 20,000 ppm S. The latter fuel was doped to ASTM D1141-52 specification for sea salt with the constituents ratioed to the 100 ppm Na. The nominal gas temperature was 1475K (2200°F) in each case. The nominal metal temperatures for the coated specimens were 1170K (1650°F) for the clean fuel run, 1075K (1475°F) for the high V doped fuel run and 1115K (1550°F) for the sea salt doped fuel. Uncoated substrate alloy test pins were also tested in these runs, but at metal temperatures 55K (100°F) higher in temperature to account for the lack of the thermal barrier. Each thermal cycle consisted of 55 minutes of heating in the furnace and 5 minutes of forced air cooling when the fixture was retracted.

The specimens were examined at least once a day during a cooling cycle. At approximately the 167 cycle intervals, the fixture was removed from the test furnace for more careful specimen examination. Failed specimens were replaced with new ones.

3.3.3.3 Task III - Coating Improvement and Endurance Testing. The endurance test was a 1000 hour run burning No. 2 distillate doped with 100 ppm Na, 10 ppm Mg, 180 ppm Cl, 3 ppm K, 4 ppm Ca and 20,000 ppm S (sea salt specifications). The nominal gas temperature was 1475 (2200°F) and the nominal metal temperatures of the coated specimens was controlled at 1115K (1550°F). The test procedure was the same as used in Task IA. At approximately 167 hour intervals the specimens were removed from the furnace and examined. Failed specimens were replaced with new ones. The maximum run time allowed for any specimen was 500 hours.

3.4 Results

3.4.1 Task I - Preliminary Coating Development and Screening Tests

The performance of coatings in the five categories with respect to the test fuels are summarized in Table 3.5. If both buttons passed the test without cracking or flaking, the coating was considered to have survived (S). If one of the pair were defective after testing the results were designated mixed (M) and if both were cracked or flaked, then the coating was considered to have failed (F).

The candidate with the best performance was the coarse grained $ZrO_2 \cdot 8Y_2O_3$, especially that which used the NASA developed plasma spraying process. It was the most highly developed coating tested and as a result survived all the screening tests.

A number of other candidates showed some potential, but require further development and testing. These candidates listed in their various categories are:

TABLE 3.5 - SUMMARY OF TASK I - COATING DEVELOPMENT AND SCREENING TEST RESULTS

	Fuel Type: Clean			Na Doped			V Doped		
	Survived	Mixed	Failed	Survived	Mixed	Failed	Survived	Mixed	Failed
A. Zirconia Compositional Variations									
$ZrO_2 \cdot 2.5\ Y_2O_3$					M		S		
$ZrO_2 \cdot 5.5Y_2O_3$					M			M	
$ZrO_2 \cdot 6Y_2O_3$	S					F			
$ZrO_2 \cdot 8Y_2O_3$	S			S			S		
$ZrO_2 \cdot 10.5Y_2O_3$						F			
$ZrO_2 \cdot 14Y_2O_3$						F			
$ZrO_2 \cdot 25Y_2O_3$	S				M		S		
$ZrO_2 \cdot 30Y_2O_3$			F						
$ZrO_2 \cdot 38Y_2O_3$			F						
$ZrO_2 \cdot 13CaO_2$			F						
$ZrO_2 \cdot 24CaO_2$	S					F			
$ZrO_2 \cdot 58CaO_2$	S				M		S		
$ZrO_2 \cdot 81CaO_2$			F						
$ZrO_2 \cdot 15Y_2O_3 \cdot 10Ta_2O_5$		M				F			
$ZrO_2 \cdot 20Y_2O_3 \cdot 10Ta_2O_5$		M				F			
B. Composites with Zirconia									
90% $ZrO_2 \cdot 8Y_2O_3$ + 10% ZrO_2			F						
85% $ZrO_2 \cdot 8Y_2O_3$ + 15% ZrO_2		M							
80% $ZrO_2 \cdot 8Y_2O_3$ + 20% ZrO_2			F						
85% $ZrO_2 \cdot 8Y_2O_3$ + 15% ZrO_2 fibers						F			
85% $ZrO_2 \cdot 8Y_2O_3$ + 15% Al_2O_3 fibers						F			
99% $ZrO_2 \cdot 8Y_2O_3$ + 1% Pt		M		S				M	
98% $ZrO_2 \cdot 8Y_2O_3$ + 2% Pt	S				M			M	
95% $ZrO_2 \cdot 8Y_2O_3$ + 5% Pt							S		
75% $ZrO_2 \cdot 8Y_2O_3$ + 25% MgO						F			
ZrO_2 + Al_2O_3 eutectic			F						
ZrO_2 + YVO_4									F
$ZrO_2 \cdot 8Y_2O_3$ + $3Al_2O_3 \cdot 25.0_2$			F						
$ZrO_2 \cdot 20Y_2O_3$ (Multilayered SD)/NiCrAlY						F			
$ZrO_2 \cdot 20Y_2O_3$ (Multilayered SD)/NiCrAlY						F		M	
C. Overcoats on Zirconia									
$AlPt_3/ZrO_2 \cdot 8Y_2O_3$					M			M	
$ZrPt_3/ZrO_2 \cdot 8Y_2O_3$					M		S		
$HfPt_3/ZrO_2 \cdot 8Y_2O_3$				S				M	
$TaPt_3/ZrO_2 \cdot 8Y_2O_3$					M			M	
$TiPt_3/ZrO_2 \cdot 8Y_2O_3$						F			
$ZrO_2 \cdot 8Y_2O_3$ (SD)/$ZrO_2 \cdot 8Y_2O_3$				S					F
Pt (LP)/$ZrO_2 \cdot 8Y_2O_3$					M				F
Glass (FM)/$ZrO_2 \cdot 8Y_2O_3$						F		M	
D. Layers Intermediate to Zirconia and Bond Coating									
$ZrO_2 \cdot 8Y_2O_3$/Cr	S			S					F
$ZrO_2 \cdot 8Y_2O_3$/Mo			F						
$ZrO_2 \cdot 8Y_2O_3$/Ti			F						
$ZrO_2 \cdot 8Y_2O_3$/Pt (IP)						F			
$ZrO_2 \cdot 8Y_2O_3/ZrO_2 \cdot 8Y_2O_3$ (sputtered)						F			
$ZrO_2 \cdot 8Y_2O_3$/Pt screen		M				F		M	
$ZrO_2 \cdot 8Y_2O_3$/In 600 40 mesh screen			F			F			F
$ZrO_2 \cdot 8Y_2O_3$/In 600 80 mesh screen	S				M			M	
E. Other Ceramics									
$La_{.95}Mg_{.05}Cr_{.5}Al_{.5}O_3$	S				M				F
$La_{.95}Sr_{.05}CrO_3$						F			
Cr_2O_3						F			
MgO + $MgCrO_3$ eutectic			F						
$CaSO_4$	S					F			
CeO_2		M							
$ZrSiO_4$			F						
TiO_2			F						
HfO_2			F						
TiB_2									F
$3Al_2O_3 \cdot 2SiO_2$.			F						
$AlPt_3$ (SD)						F			

- Zirconia compositional variations:
  plasma sprayed $ZrO_2 \cdot 2.5$ to $25Y_2O_3$
  plasma sprayed $ZrO_2 \cdot 13$ to 58 CeO_2
- Composites with zirconia:
  plasma sprayed $ZrO_2 \cdot Y_2O_3$ + 1 to 5% Pt
- Overcoats on zirconia:
  Pt or AlPt on plasma sprayed $ZrO_2 \cdot Y_2O_3$
  Dense $ZrO_2 \cdot Y_2O_3$ on plasma sprayed $ZrO_2 \cdot Y_2O_3$
  Glass on plasma sprayed $ZrO_2 \cdot Y_2O_3$
- Intermediate layers between plasma sprayed zirconia and bond coat:
  Metal wire screen
- Other ceramics:
  $LaCr_{0.5}Al_{0.5}O_3$

Most of the other coatings tested appeared to have little or no potential.

3.4.2 Task IA - Burner Rig Exposure Tests

3.4.2.1 Clean Fuel Test Results. Fourteen coated and two uncoated specimens were tested in the combustion products of No. 2 distillate. The results of the test are presented in Table 3.6. No failures of the plasma sprayed base coats were observed for this 500 hour test. However, three of the thicker overcoats (.75 Z20Y/Z8Y, .75 Pt G. Z20Y/Z8Y and .75 AlPt G. Z20Y/Z8Y) did show failures which started during the first few cycles of the test. The thinner overcoats maintained adherence. The remaining thick overcoat (.6 Pt/Z8Y) maintained general adherence but had a few spots where the overcoat was chipped off probably due to handling. The overcoating failures of the former three were associated with poor adherence of the sputter deposited $ZrO_2 \cdot 20Y_2O_3$ on the plasma sprayed $ZrO_2 \cdot 8Y_2O_3$ material.

TABLE 3.6 - RESULTS OF CLEAN FUEL TEST IA-C, TASK IA BURNER RIG EXPOSURE TESTS

Fuel: No. 2 Distillate
Maximum Nominal Metal Temperature: 1170K (1650°F)(coated specimens)
1225K (1750°F)(uncoated specimens)
Cycle: 55 min. Heating, 5 min. Air Cooling

SPEC. NO.	POSITION		POL.	TIME TO INITIAL FAILURE, Hr.	OVERALL DESCRIPTION
21	4	N-Z8Y	P	>500	
19	16	N-Z8Y		>500	
1	3	.2 Pt/Z8Y		>500	
44	15	.6 Pt/Z8Y	P	>500	A few small regions of mechanical damage.
15	1	.2 Z20Y/Z8Y		>500	
53	13	.75 Z20Y/Z8Y	P	>500	≈ 50% of overcoating flaked off.
12	9	.3 Pt G. Z20Y/Z8Y		>500	
31	5	.75 Pt G. Z20Y/Z8Y	P	>500	Overcoat fish scaled over entire surface.
43	7	.3 AlPt G. Z20Y/Z8Y		>500	
22	11	.75 AlPt G. Z20Y/Z8Y	P	>500	≈ 75% of overcoating flaked off.
74	2	W-Z8Y	P	>500	
73	14	W-Z8Y		>500	
64	6	W-Z8Y/In. Scr.		>500	
65	10	W-Z8Y/In. Scr.		>500	
B2	8	Uncoated U720		>500	
V2	12	Uncoated ECY		>500	

(a) P = polished plasma sprayed surface

3.4.2.2 Residual Doped Fuel Test Results. The test conditions and results of the high V and Mg doped fuel tests are presented in Table 3.7.

Even though the failure initiation times listed in the table show a great deal of scatter, there appear to be qualitative differences between the coatings. In making comparisons, the overcoated types should be compared with the NASA base coat. The total population of overcoated specimens seemed to have improved lives. The thin overcoats were no different than the N-Z8Y coatings, but the thick overcoated ones performed better. No distinction could be made between the performance of polished and as-plasma sprayed specimens.

Coating failures initiated slightly more at the front, top edge of the specimens than at the bottom. In both cases the failures started as cracks parallel to the interface and formed a small chip at the end of the coating. Flaking progressed with time up or down the surface facing the gas flow. In some cases, it progressed to the back of the specimen and eventually led to a total loss of the coating.

The Westinghouse base coatings also appeared to have longer lives than the NASA base coats. There was no difference in failure initiation times between the Westinghouse base coats and those with Inconel screen intermediate layers. However, there was a significant difference in crack propagation rates. Usually, a significant fraction of the coating flakes off within the first 20 hours after failure initiation is observed. In the cases of coatings with Inconel screen intermediate layers, the flaking progressed slowly and was not significant until about 125 hours had passed. Therefore, the screening was acting as a crack arrestor and/or compliant zone as designed.

3.4.2.3 Accelerated Sea Salt Test Results. The results of the sea salt doped fuel tests are presented in Table 3.8. Even though the failure initiation times listed in the table show scatter, there are qualitative differences between the coatings. In making comparisons, the overcoated types should be compared with the NASA base coat. The total population

TABLE 3.7 - RESULTS OF RESIDUAL DOPED FUEL TEST IA-D1, TASK IA, BURNER RIG EXPOSURE TESTS

Fuel: No. 2 Distillate doped with 50 ppm V, 150 ppm Mg, 1 ppm Na, 15 ppm Pb, 0.5 ppm Ca and 0.5% S

Maximum Nominal Metal Temperature: 1475°F (coated specimens)
1575°F (uncoated specimens)

Cycle: 55 min. Heating, 5 min. Air Cooling

SPEC. NO.	POSITION	SPECIMEN TYPE	POL.	TIME TO INITIAL FAILURE, Hr.	LOCATION OF INITIAL FAILURE	TOTAL TIME, Hr.	DESCRIPTION
N1	4	N-Z8Y	P	123	Top Front	173	80% of Front Flaked
N2	16	N-Z8Y	-	115	Top Front	173	75% of Front Flaked
10	3	.2 Pt/Z8Y	-	123	Top Front	173	Front Totally Flaked
48	3	.6 Pt/Z8Y	-	151	Bottom Front	327	75% of Front Flaked
29	15	.6 Pt/Z8Y	-	240	Bottom Front	500	Front Totally Flaked
41	1	.2 Z20Y/Z8Y	-	173	Bottom Front	173	15% Flaked
52	1	.75 Z20Y/Z8Y	P	159	Bottom Front	323	Front Almost Totally Flaked
54	13	.75 Z20Y/Z8Y	P	250	Top Front	500	Top Half Flaked
42	5	.3 Pt G. Z20Y/Z8Y	-	165	Top Front	327	75% of Front Flaked
46	9	.3 Pt G. Z20Y/Z8Y	-	173	Bottom Front	173	15% of Front Flaked
8	5	.75 Pt G. Z20Y/Z8Y	-	168	Bottom Front	173	50% of Front Flaked
47	7	.3 AlPt G. Z20Y/Z8Y	P	96	Top Front	173	60% of Total Flaked
13	7	.75 AlPt G. Z20Y/Z8Y	-	323	Top Front	327	Small Chip At Top
9	11	.75 AlPt G. Z20Y/Z8Y	-	89	Top Front	173	Front Totally Flaked, 50% of Rear
76	2	W-Z8Y	P	144	Bottom Front	173	40% of Front Flaked
69	2	W-Z8Y	-	252	Top Front	327	70% of Front Flaked
78	14	W-Z8Y	-	490	Top Front	500	Flaked 1 cm. Down
58	6	W-Z8Y/In. Scr.	-	250	Top Front	500	70% of Front Flaked
62	10	W-Z8Y/In. Scr	-	324	Center Side	500	Totally Flaked

(a) P = polished plasma sprayed surface

TABLE 3.8

RESULTS FROM THIRD SERIES OF TASK IA BURNER RIG EXPOSURE TESTS AFTER 500 HOURS

Fuel: No. 2 Distillate doped with 100 ppm Na, 10 ppm Mg, 180 ppm Cl, 3 ppm K, 4 ppm Ca and 2% S
Maximum Metal Temperature: 1550°F (coated); 1650°F (uncoated)
Cycle: 55 min. Heating + 5 min. Air Cooling

Spec. No.	Position	Specimen Type	Pol.	TIME TO INITIAL FAILURE, Hr.	LOCATION OF INITIAL FAILURE	TOTAL TIME, Hr.	Description
N-5	4	N-Z8Y	-	90	Top Front	336	Front totally flaked.
N-6	16	N-Z8Y	-	90	Top Front	336	Front flaked 80%
37	3	.6 Pt/Z8Y	P	>336		336	50% of overcoat flaked
14	15	.6 Pt/Z8Y	-	90	Top & Bottom Front	336	25 mm flake at top, 3 mm flake at bottom.
28	3	.2 Pt/Z8Y	P	>164		164	
6	14	.2 Pt/Z8Y	-	101	Top & Bottom Front	164	11 x 12 mm, 18 x 8 mm, 2 x 3 mm flakes
49	1	.75 Z20Y/Z8Y	P	435	Middle & Bottom Front	500	13 x 8 mm, 6 x 7 mm, 2 x 7 mm, 7 x 3 mm flakes
50	13	.2 Z20Y/Z8Y	-	463		500	Chips and spalls overall
45	16	.2 Z20Y/Z8Y	P	129	Top Front	164	Mud cracks and 5 x 15 mm flake at top
25	2	.08 Z20Y/Z8Y	P	>164		164	
26	5	.75 Pt G.Z20Y/Z8Y	P	90	Top Front & Bottom Back	336	Overcoat heavily spalled, 12 mm flake at top
4	9	.75 Pt G.Z20Y/Z8Y	-	336	Top Front	336	5 x 13 mm
39	5	.2 Pt G.Z20Y/Z8Y	-	>164		164	Overcoat bubbled
32	7	.75 AlPt G.Z20Y/Z8Y	P	>336		336	Overcoat spalled
5	11	.75 AlPt G.Z20Y/Z8Y	-	463	Top Front & Back	500	5 x 10 mm, 9 x 10 mm flakes
40	7	.2 AlPt G.Z20Y/Z8Y	P	156	Top Front	164	Flaked 90% of length
71	2	W-Z8Y	-	177	Top Front	336	19 x 14 mm, 15 x 7 mm flakes
68	14	W-Z8Y	-	103	Top Front	336	Front nearly totally flaked
63	6	W-Z8Y/In.Scr.	-	404	Overall	500	Multiple spalls over surface
67	10	W-Z8Y/In.Scr.	-	336	Middle Side	336	2 x 2 mm flakes, metal badly corroded above coating
57	10	W-Z8Y/In.Scr.	-	>164		164	Metal corroded above coating
B4	8	Uncoated U710	-		Overall	500	Badly corroded, ~2 mm deep in places
V4	12	Uncoated ECY	-		Overall	500	Badly corroded, ~1 mm deep in places

of overcoated specimens seemed to have improved lifetimes. The average lifetime of each of the overcoating types were at least 2 to 3.5 times that of the NASA baseline coating. For this high sodium containing fuel, the $ZrO_2 \cdot 20Y_2O_3$ and the AlPt graded to $ZrO_2 \cdot 20Y_2O_3$ overcoats performed better than the Pt and Pt graded to $ZrO_2 \cdot 20Y_2O_3$ overcoats. No difference was found between the performance of overcoats on polished surfaces and the as-plasma sprayed surfaces. However, thicker overcoats outperformed the thinner ones. On average, the thick overcoats ran 50% longer than the thin ones before failing.

The Westinghouse base coatings had longer average lives than the NASA basecoats (approximately 50% longer). On average, the Westinghouse specimens with Inconel screens went twice as long before failure initiation as the Westinghouse base coated specimens. Again, as in previous tests, the initiation of flaking did not lead to catastrophic failure for the screen containing coatings. Even at the end of 500 hours, these coatings had considerable protective coating volume available.

The worst corrosion occurred on the uncoated specimens where nearly 1 to 2 mm of recession was observed. Even after flaking, the poorest of the coated specimens did not allow this amount of metal corrosion.

3.4.3 Task III - Coating Improvement and Endurance Testing

Task III was divided into two 500 hour test series. The conditions and results of these are presented in Tables 3.9 and 3.10. A large number of the Initial Times to Failure have "<" and ">" symbols preceeding the values. The "<" symbol indicates that the particular specimen started to fail prior to the first inspection. The ">" symbol indicates that the specimen lifetime was greater than the value. In some cases, this means that the specimen exceeded the 500 hour test limit. However, in the first series there was a temperature excursion for two cycles (hours) at the 455th hour of the run caused by a loss of cooling air. This allowed the metal temperatures to exceed 1285K (1850°F) causing premature failures of a number of coatings. These coating failure times

TABLE 3.9—RESULTS FROM FIRST SERIES OF TASK III BURNER RIG EXPOSURE TESTS AFTER 506 HOURS

Fuel: No. 2-Distillate Doped with 100 ppm Na, 10 ppm Mg, 180 ppm Cl, 3 ppm K, 4 ppm Ca and 2 % S
Nominal Gas Temperature: 2200°F
Maximum Metal Temperature: 1550°F
Cycle 55 Min. Heating + 5 Min. Air Cooling

Spec. No.	Test Position	Intermediate Layer				Overcoat Layer									Time to Initial Failure, Hr.	Initial Failure Location	Total Time Hr.	Description
		None[a]	50 v/o $ZrO_2 \cdot 8Y_2O_3$ + 50 v/o N	Inconel Screen	Felt-Metal	Fine[e] ZBY	EK5 Glass + ZBY[f]		EK7 Glass + ZBY[f]		3831 Glass + ZBY[f]		5301 Glass + ZBY[f]					
							25 v/o	40 v/o	20 v/o	40 v/o	20 v/o	40 v/o	20 v/o	40 v/o				
127	5	X				X									> 455[g]	Top & Bottom	506	Multiple Chips at Top & Bottom
123	11	X					X								> 455[g]	Middle Front	506	5 × 5 mm Chip in Middle
128	1	X						X							> 290[g]	Top Front	340	Multiple Chips at Top and Bottom
125	15	X							X						> 506[h]		506	
126	1	X								X					73	Top Front	166	7 × 6 mm Chip at Top
141	7	X									X				177[h]	Middle	177	20 × 10 mm Chip in Middle
136	6	X										X			> 290[g]	Top Front	340	6 × 20 mm, 10 × 27 mm Flakes in Top Half
138	6	X											X		334	Top & Bottom Front	334	Top Chipped 3 mm Down. Overcoat Flaked 22 mm × 20 mm Up from Bottom
140	16	X												X	> 290[g]	Middle	340	Multiple Small Chips Over Total Surface
115	3		X			X									> 290[g]	Bottom Front	340	Chip 5 mm Up from Bottom. 6 × 11 mm Chip in Middle
111	7		X				X								318	Top Front	333	9 × 6 mm at Top. 2 × 10 mm at Bottom
120	3		X					X							< 23	Top Front	166	15 × 15 mm Flake at Top
113	9		X						X						> 506[h]		506	
114	13		X							X					> 455[g]	Over All	506	Multiple Chips in Lower Half and Top Edge
133	16		X								X				> 500		500	Overcoat Flaking Near Bottom
134	12		X									X			> 122[g]	Top	173	23× 10 mm & 22 × 10 mm Flakes at Top. Multiple Chips in Bottom Half
137	8		X										X		194	Middle and Top Back	338	Flaked at Top Back 20 mm Down. Overcoat Chipped & Cracked
139	2		X											X	44	Top Front	173	13 × 20 mm Flake at Top. Multiple Chips in Middle
110	14			Coarse[c]		X									> 506[h]		506	
103	8			Coarse[c]			X								> 290[g]	Top	340	4 × 10 mm & 4 × 8 mm Flakes at Top. 3 × 2 mm Chips in Middle
104	8			Fine[d]				X							< 23	Top Front	166	Flaked 20 mm Down from Top
102	4			Fine[d]					X						> 455[g]	Middle	506	3 × 3 mm, 4 × 4 mm & 5 × 5 mm Chips in Middle
105	10			Coarse[c]						X					> 455[g]	Middle	506	2 × 2 mm Chip in Middle
100	12				7 mil	X									190	Top Front	333	Coating Loose & Flaked 30 × 20 mm from Top. Feltmetal Debonded
95	2				10 mil		X								< 23	Top & Bottom Front	166	Chipped Top & Bottom. Wide Crack Halfway Up from Bottom. Feltmetal Debonded
97	16				7 mil			X							< 23	Top Front & Back	166	Flaked Off Halfway Down. Feltmetal Debonded
99	2				7 mil				X						99	Top	168	Coating Almost Totally Debonded. Top Half Flaked Off
96	6				10 mil					X					< 23	Top Front	166	Full Length Wide Crack Plus Other Cracks

(a) NiCrAlY Bond Coating Only
(b) 50 v/o $ZrO_2 \cdot 8Y_2O_3$ + 50 v/o NiCrAlY
(c) 80 × 80 Mesh Inconel 600, 4 mil Diameter Wire Screen
(d) 160 × 140 Mesh Inconel 600, 4 mil Diameter Wire Screen
(e) −270 Mesh + 10 μm $ZrO_2 \cdot 8Y_2O_3$
(f) Plasma Sprayed Mechanical Mixtures of Glass and −270 Mesh + 10 μm $ZrO_2 \cdot 8Y_2O_3$. Percentages Refer to Glass Content
(g) Failures Caused by Loss of Cooling Air During Two Cycles in Mid Test. Metal Temperatures Rose to 1285°K (1850°F)
(h) Survived Loss of Cooling Air During Two Cycles in Mid Test

TABLE 3.10 – RESULTS FROM SECOND SERIES OF TASK III BURNER RIG EXPOSURE TESTS AFTER 500 HOURS

Fuel: No. 2 Distillate Doped with 100 ppm Na, 10 ppm Mg, 180 ppm Cl, 3 ppm K, 4 ppm Ca, and 2% S
Nominal Gas Temperature: 2200°F
Maximum Metal Temperature: 1550°F
Cycle: 55 Min. Heating + 5 Min. Air Cooling

Spec. No.	Test Position	Intermediate Layer				Overcoat Layer		Time to Initial Failure, Hr	Initial Failure Location	Total Time	Description
		None[a]	50 v/o Z8Y[b] + 50 v/o N	Fine[c] Mesh Screen	Coarse[d] Mesh Screen	Pt[e]	Al Pt[f]				
122	4	X				X		242	Top Front	500	75% of Overcoat Spalled Off. 10 × 20 mm Coating Flake at Top. Severe Corrosion Above Coating
121	12	X					X	> 500		500	Overcoat Extensively Cracked. Severe Corrosion Above Coating
117	3		X			X		271	Top Front	338	50% of Overcoat Spalled Off. Coating Flaked 15 mm Circumferentially at Top
118	11		X			X		> 500		500	Overcoat Cracked and Spalled. Severe Corrosion Above Coating
116	15		X				X	500	Top Front	500	Overcoat Cracked and Spalled. 20 × 10 mm Coating Flake at Top
119	7		X				X	172	Top Front	172	Overcoat Cracked Overall. 14 × 20 mm Coating Flake at Top
131	6			X		X		172	Top Front	172	28 × 10 mm and 18 × 10 mm Flaked Coating at Top
129	14			X		X		172	Top Front	172	7 × 5 mm Coating Flake at Top. Two 15 mm Long Cracks from Top. Coating Loose Near Top
130	2			X			X	194	Top Front	338	80% of Overcoat Spalled Off. 3 × 20 mm Coating Flake at Top. 8 × 3, 6 × 9 and 10 × 8 mm Coating Flakes in Middle
132	10			X			X	462	Top Front	500	25 × 15 mm Overcoat Spall at Top. 7 × 4 mm Coating Flake at Top. 2 × 2 mm Flake in Middle
108	1				X	X		> 500		500	Severe Corrosion Above Coating
109	9				X	X		172	Top Front	500	10 × 20 mm Overcoat Flake Near Bottom. 4 × 6 mm Coating Flake at Top
106	13				X		X	172	Top Front	172	Overcoating Cracked. 8 × 12 mm Coating Crack at Top
107	5				X		X	242	Top Front	500	Overcoat Spalling Overall. 9 × 5 mm Coating Flake in Middle. Severe Corrosion Above Coating
AT3	13	EB-PVD						< 22	Over All	166	Coating Totally Off. Substrate Corrosion Through Pin Holes in Bond Coat
AT4	3	EB-PVD						< 26	Over All	162	90% of Coating Flaked Off. Severe Substrate Corrosion in Middle
AT5	14	EB-PVD						70	Top Front	328	10 × 20 mm Flake at Top. 6 × 10 mm Flake in Middle. Severe Corrosion Under Flakes
AT9	7	EB-PVD						< 22	Over All	166	95% of Coating Flaked Off
AT21	7	EB-PVD						< 26	Middle Front	162	32 × 20 mm Flake at Top. 6 × 3 mm in Middle. Severe Corrosion Above Coating and at Middle Chip
AT23	8	EB-PVD						< 26	Over All	162	95% of Coating Flaked Off. Corrosion Above Coating at Top

(a) NiCrAlY Bond Coating Only
(b) 50 v/o $ZrO_2 \cdot 8\ Y_2O_3$ + 50 v/o NiCrAlY
(c) 160 × 140 Mesh Inconel 600, 4 mil Diameter Wire Screen
(d) 80 × 80 Mesh Inconel 600, 4 mil Diameter Wire Screen
(e) 31 μm Thick Sputter Deposited
(f) 14 μm Thick Sputter Deposited

(>122, >290 and >455), designated by the superscript "g", would have been expected to exceed the values under normal operating conditions. A few which did survive the excursion are designated by the superscript "h".

The overall average endurance of coatings which combined overcoats with intermediate layers was greater than that of the NASA baseline coating tested in Task IA, by at least a factor of three. One overcoat, 40% EK5 glass + $ZrO_2 \cdot 8Y_2O_3$ did not perform as well as the others tested. The expansion coefficient of the glass was probably not as well matched as the others, giving rise to larger magnitude residual stresses. The coatings with Feltmetal intermediate layers also did not fare as well as the baseline coating. Oxidation of the Feltmetal and the braze caused early debonding at the Feltmetal/bond coating interface.

The PVD coating endurance was less than the NASA baseline. Most of the failures were by thermal stress rather than corrosion, and all but one failed within the first 26 hours of testing. One specimen, AT5, survived 70 cycles and had a significant amount of coating remaining after 328 hours of testing.

3.5 Analysis of Test Results

3.5.1 Task I - Preliminary Coating Development and Screening Tests

3.5.1.1 Thermal Stress Resistance. A large percentage of the failures in Task I were attributable to two sources of thermal stresses:residual and transient. The residual coating stresses arise on cool down from the high temperature application temperatures due to differences in coefficients of thermal expansion, CTE, between the coatings and substrates and to differences in the temperatures of the coatings and substrate during deposition. High values of coating elastic moduli increase the stresses, although coating strengths and toughness would also increase. The zirconia based materials perform better than the other ceramics

because zirconia has a higher CTE, more closely matching that of the substrate.

Both the residual and transient (heat up) thermal stresses are proportional to the elastic modulus. The modulus in turn decreases exponentially with increasing pore fraction. Thus, the coarser grained zirconia with ∿20 v/o porosity fared better than the finer grained material with ∿14 v/o porosity (see Figure 3.4). Many of the coating concepts which were to be evaluated in this task were not fairly tested because of lack of particle size (porosity) control. For example, most compositional variations of zirconia and composites with zirconia consisted of finer grained material than the $ZrO_2 \cdot 8Y_2O_3$.

The concept of using fiber reinforcement of zirconia proved invalid since the reinforcement increased the elastic modulus and the resulting thermal stresses. The coating was also strengthened in the wrong direction, i.e., parallel to the interface rather than perpendicular to it.

3.5.1.2 Crack Propagation Resistance. A variety of attempts were made to retard crack propagation. The porosity in most of the coatings tends to blunt cracks, but microcracks are probably more efficient. The one attempt at adding additional microcracks by adding pure zirconia to the partially stabilized material failed in the clean fuel tests. However, this material received insufficient development time.

Attempts to retard crack propagation with metallic additions (Pt) to zirconia had mixed results. Again the fine grained, higher modulus $ZrO_2 \cdot 8Y_2O_3$ was used and the material was by no means optimized.

The wire screens at the ceramic bond coat interface did show promise. As shown in Figure 3.5, although cracks occurred in this denser zirconia on the flat topped buttons which were subjected to higher thermal stresses, the imbedded wires prevented the coating from flaking off. Also, the wires tended to localize coating failures.

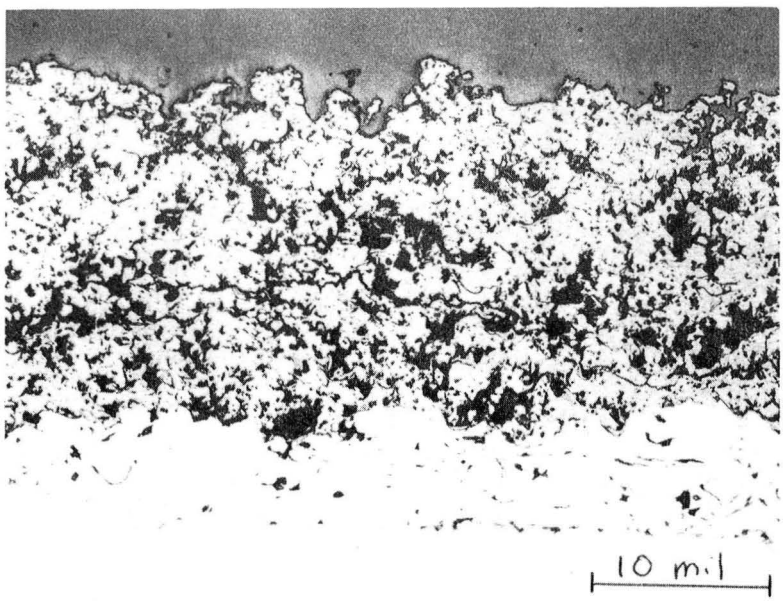

A) 55 μM AVERAGE PARTICLE SIZE

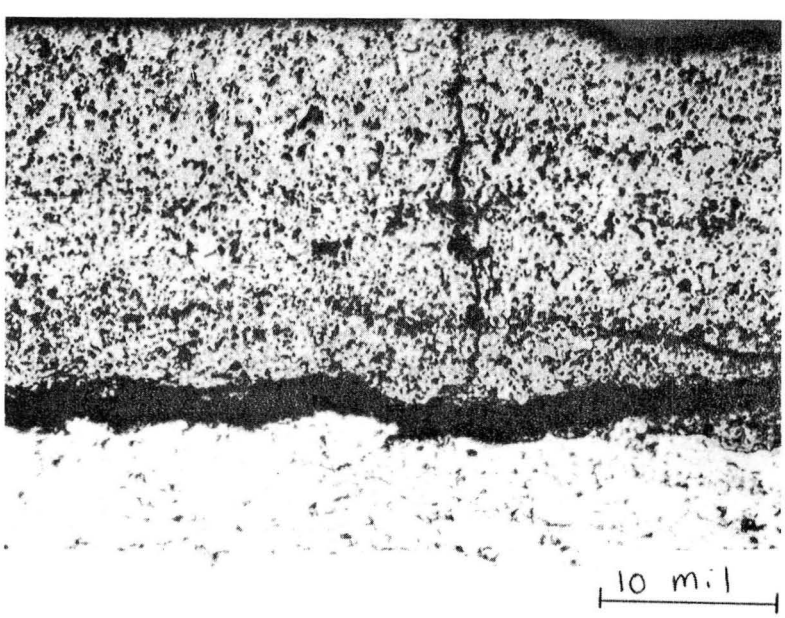

B) 8 μM AVERAGE PARTICLE SIZE

Fig. 3.4 - Photomicrographs of $ZrO_2 \cdot 8Y_2O_3$ coated button specimens after screening test run No. 4

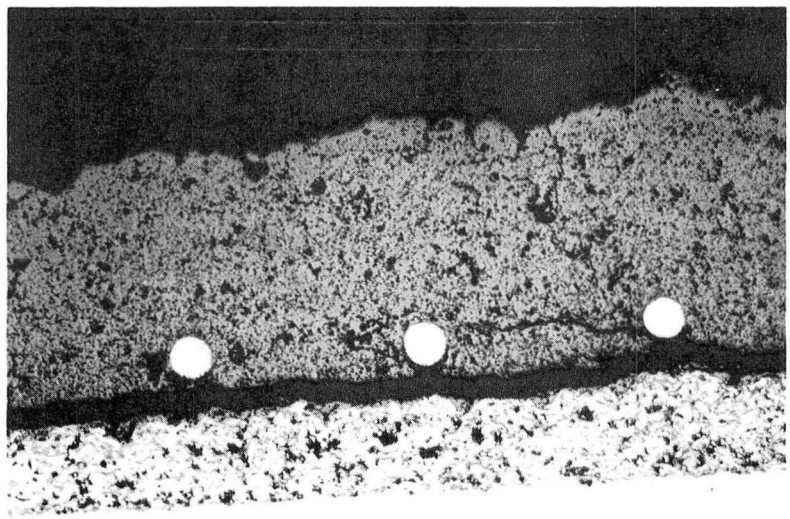

a) Fine wire mesh

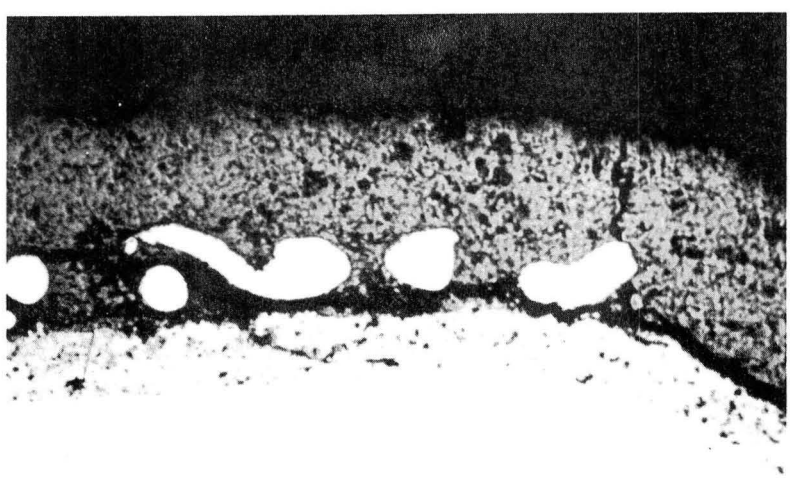

b) Coarse wire mesh

Fig. 3. 5 - Cross-sections of Inconel 601 wire mesh reinforced $ZrO_2 \cdot 8Y_2O_3$ coated buttons after screening tests

3.5.1.3 Corrosion Resistance. Since all of the materials other than $ZrO_2 \cdot Y_2O_3$, $La_{.95}Mg_{.05}Cr_{.5}Al_{.5}O_3$ and $CaSO_4$ failed by thermal stress, their corrosion resistances were not actually tested. The only coating to clearly fail by corrosion was the $CaSO_4$. The 60 hours of test time allotted for each candidate in Task I was insufficient, especially for the ZrO_2 materials which generally show corrosion failures after about 100 hours. However, the potential of several systems was apparent in the post test evaluations.

The overcoating concept appeared to be functioning, since many of the overcoats retarded penetration of contaminants into the porous ceramic coatings. For example, it is apparent from a comparison of the S concentrations in Figures 3.6 and 3.7 that Na_2SO_4 was prevented from penetrating into the ceramic as a result of the overcoat. Most of the overcoats applied by plasma spraying were too thick and those by other means too thin. The thick overcoat in Figure 3.8 caused thermal stress cracking of the basecoat. The thin coating in Figure 3.9 did not cover the open porosity sufficiently. It was judged that a medium thickness layer would work, and this concept was used in the development tasks which followed.

A number of metallic and ceramic intermediate layers put on to prevent corrosion of the bond coat showed generally poor results. The Mo, Ti, Pt and sputtered $ZrO_2 \cdot 8Y_2O_3$ failed. Only the Cr layer showed any potential.

3.5.1.4 Multilayered Sputter Deposited Coatings. The multilayered coatings failed by a combination of creep of the metallic layers and fracture of the ceramic layers. In addition the NiCrAlY metallic layers were highly oxidized as shown in Figure 3.10. This concept is not a viable one for high temperature coatings.

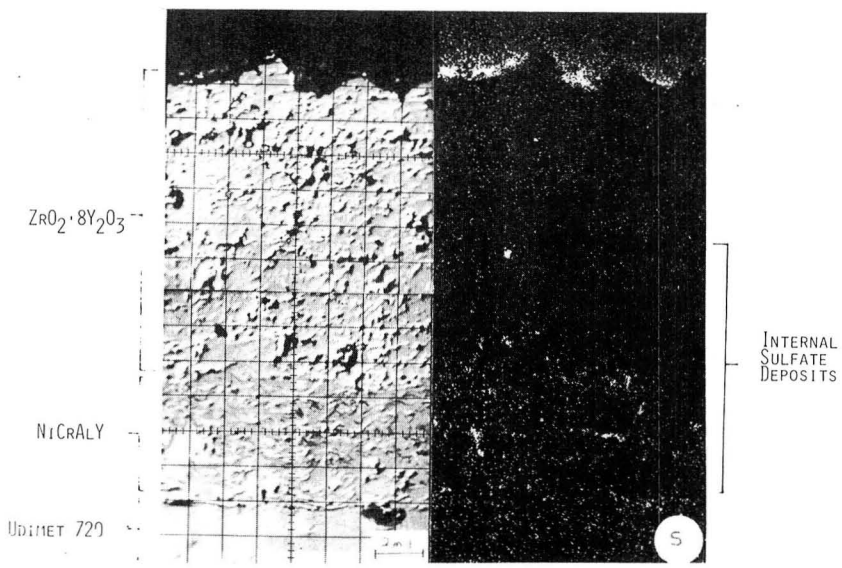

Figure 3.6 Electron microprobe mapping of sulfur for a plasma sprayed NiCrAlY/$ZrO_2 \cdot 8Y_2O_3$ coating.

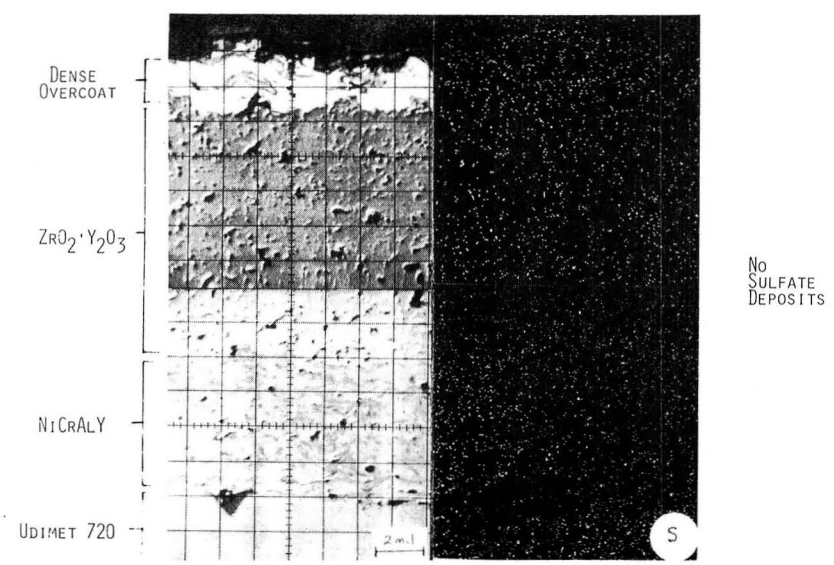

Figure 3.7 Electron microprobe mapping of sulfur for a plasma sprayed NiCrAlY/$ZrO_2 \cdot 8Y_2O_3$ coating with dense overcoat.

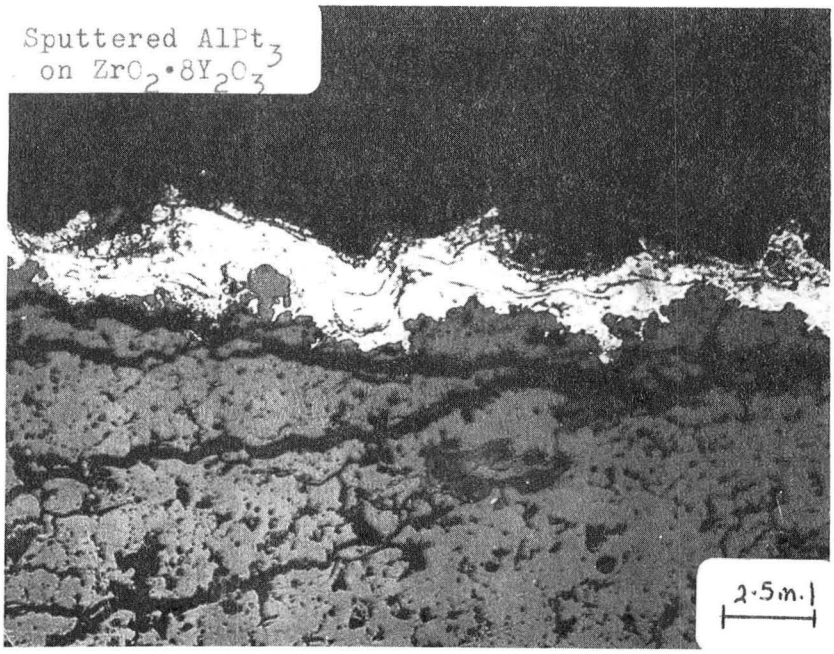

Figure 3.8 Overly thick overcoat on $ZrO_2 \cdot 8Y_2O_3$ base coat.

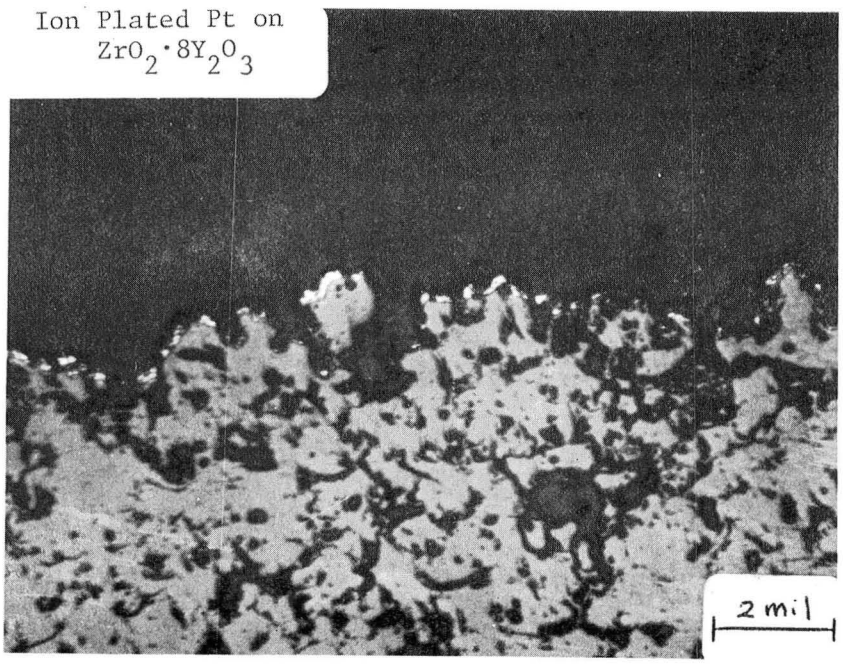

Figure 3.9 Overly thin overcoat on $ZrO_2 \cdot 8Y_2O_3$ base coat.

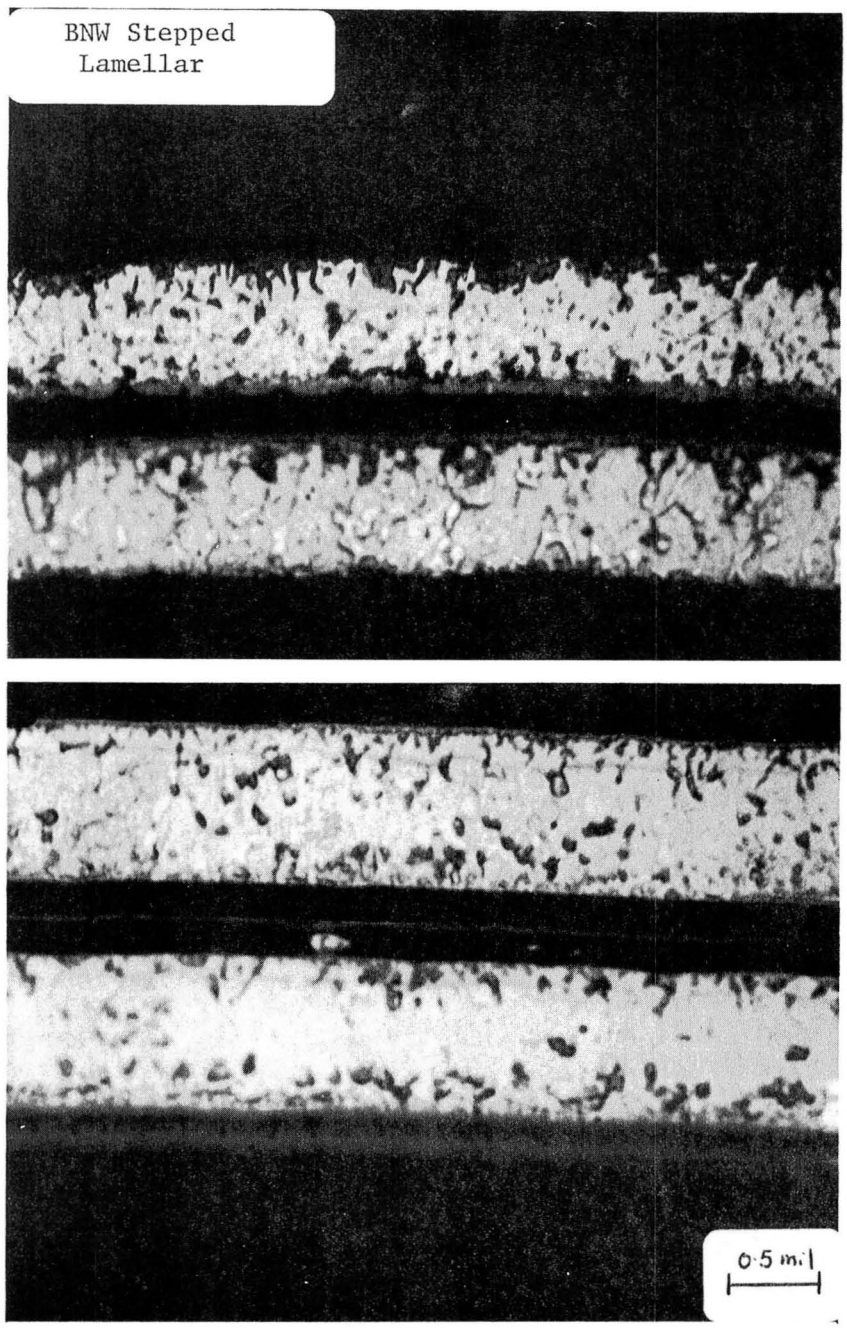

Figure 3.10 - BNW stepped lamellar coating

3.5.1.5 Task I - Conclusions. The following conclusions were reached for the Preliminary Coating Development.

- Coarse particle, low density $ZrO_2 \cdot 8Y_2O_3$ using NASA Lewis plasma spraying parameters remains the best candidate of those tested. It will be subject to corrosion due to the penetration of contaminants into the connected pores.
- Overcoats of optimum thickness can retard penetration of contaminants into base coat pores
- The wire metal screen intermediate layer retards crack propagation and mechanically locks the ceramic coating to the bond coating.
- Many of the coating systems tested were not sufficiently optimized and failed by thermal stress. A number of these still have potential, but require development.

3.5.2 Task IA - Burner Rig Evaluation and Task III- Coating Improvement and Endurance Testing

The assessment of candidate coatings for both Tasks IA and III was combined since for the most part they represent the evolution of the same concepts: overcoats and intermediate layers with $ZrO_2 \cdot 8Y_2O_3$ base coats. In addition, the test precedures were similar.

3.5.2.1 Statistical Evaluation of Coating Endurance. A statistical model was developed for relating times to initial failure to independent variables having to do with the coatings and test conditions. The model was of the form

$$\log T = \beta_o + \sum_i \beta_i X_i + \sum_{i\ j} \beta_{ij} X_i X_j + \varepsilon, \quad i<j \qquad (1)$$

where T denotes the adjusted hours to initial failure, β_o denotes the model description for a specified set of null test conditions, X_i denotes the independent variables, β_i and β_{ij} denote the unknown coefficients

relating the independent variables to failure times and ε is the error term. Twenty independent variables listed in Table 3.11 were assessed. The X_i are dummy variables, 0 or 1, that serve to include or exclude particular features in the model description. A total of 81 observations listed in Table 3.12 were assessed.

The hours to initial failure, T, that were used in the model were adjusted in some cases from the failure times, t, appearing in the laboratory records and in Table 3.12. The reason is that some of the tests were stopped before failure occurred and in one run there was a temperature excursion that caused premature failure. Also, some specimens failed prior to the first examination. These are designated by footnotes in Table 3.12. The following rules were used: When t was not footnoted, T was equal to t. Values of t >455* and >290* were adjusted to T = 500 and 333, respectively. Values of t >500**, 336** and >164** were adjusted to T = 1000, 400 and 200, respectively. Values of t <23*** were adjusted to T = 10. These adjustments represent best estimates of expected times to initial failures.

Finally, log T was used in the model rather than T itself in order to better approximate the experimental error. In many kinds of time-to-failure data, the standard deviation can be shown to be proportional to the average value of T, which means that the standard deviation of log T is constant throughout the range of values. Evaluation of the data assessed in the present case confirmed this to be a good assumption.

At first glance, the analysis appears to be optimistic since a number of the failure times were adjusted to values well beyond the actual maximum 500 hour run times, e.g., 1000 hrs. In fact, the analysis is rather conservative, since it was performed on logarithmically transformed times. This weights the effect of the lower failure times with respect to the longer ones. For example, the arithmetic mean of 100, 200, 800 and 900 hours is 500 hours, whereas the logarithmic mean is 2.54 or 346 hours. Thus, there would be only a small difference between adjusting times to 1000 hours (log T = 3.00) or to 750 hours (log T = 2.88) for the analysis.

TABLE 3.11

FORM OF STATISTICAL MODEL AND POSSIBLE INDEPENDENT VARIABLES

STATISTICAL MODEL: $\log_{10} T = \beta_o + \sum_i \beta_i X_i + \sum_{i<j} \sum_j \beta_{ij} X_i X_j + \varepsilon$

β_0 is the model description for the case of Westinghouse Basecoat
No Intermediate Layer (IL)
No Overcoat Layer (OL)
No Polishing
Front Row of Furnace
High Sodium Fuel

The X_i's serve to introduce other conditions into the model

X_1 = 1 if NASA Basecoat, 0 otherwise (OTH)
X_2 = 1 if graded IL, 0 OTH
X_3 = 1 if fine mesh screen IL, 0 OTH
X_4 = 1 if coarse mesh screen IL, 0 OTH
X_5 = 1 if feltmetal IL, 0 OTH
X_6 = 1 if fine ZrO_2 OL, 0 OTH
X_7 = 1 if ZrO_2 + 25% EK5 Glass OL, 0 OTH
X_8 = 1 " 40% EK5 " "
X_9 = 1 " 20% EK7 " "
X_{10} = 1 " 40% EK7 " "
X_{11} = 1 " 3831 Glass OL, 0 OTH
X_{12} = 1 " 5301 Glass OL, 0 OTH
X_{13} = 1 if Pt OL, 0 OTH
X_{14} = 1 if Al Pt OL, 0 OTH
X_{15} = 1 if $ZrO_2 \cdot 20\ Y_2O_3$ OL, 0 OTH
X_{16} = 1 if $Pt/ZrO_2 \cdot 20Y_2O_3$ OL, 0 OTH
X_{17} = 1 if $AlPt/ZrO_2 \cdot 20Y_2O_3$ OL, 0 OTH
X_{18} = 1 if polished surface condition, 0 OTH
X_{19} = 1 if back row of furnace, 0 OTH
X_{20} = 1 if high vanadium fuel, 0 OTH

TABLE 3.12

LIST OF OBSERVATIONS

SPECIMEN NUMBER	t	$\log_{10}T$	INDEPENDENT VARIABLES 1	2	3	4	5	6	7	8	9	10	11	12	13	14	15	16	17	18	19	20
127	>455*	2.7						1														
123	>455*	2.7							1													1
128	>290*	2.5								1												
125	>500***	3.0									1											1
126	73	1.9										1										
115	>290*	2.5		1				1														
111	318	2.5		1					1													
120	<23***	1.0		1						1												
113	>500***	3.0		1							1											1
114	>455*	2.7		1								1										1
110	>500***	3.0			1			1														1
103	>290*	2.5			1				1													
104	<23***	1.0		1						1												
102	>455*	2.7		1							1											
105	>455*	2.7			1							1										1
100	190	2.3				1		1														1
95	123	2.1				1			1													
97	<23***	1.0				1				1												1
99	99	2.0				1					1											
96	<23***	1.0				1						1										
141	175	2.2											1									
136	>290*	2.5											1									
138	328	2.5												1								
140	>290*	2.5												1								1
133	>500***	3.0		1									1									1
134	>122*	2.2		1									1									1
137	194	2.3		1										1								
139	44	1.6		1										1								
122	242	2.4													1							1
121	>500***	3.0														1						1 1
117	271	2.4		1											1							1
118	>500***	3.0		1											1							1 1
116	500	2.7		1												1						1 1
119	172	2.2		1												1						1
131	172	2.2			1										1							1
129	172	2.2			1										1							1 1
130	194	2.3			1											1						1
132	462	2.7			1											1						1 1
108	>500***	3.0				1									1							1
109	172	2.2				1									1							1 1
106	172	2.2				1										1						1 1
107	242	2.4				1										1						1
N-5	90	2.0	1																			
N-6	90	2.0	1																			1
28	>164***	2.3	1												1							1
6	101	2.0	1												1							1
37	>336***	2.6	1												1							1
14	90	2.0	1												1							1
45	129	2.1	1														1					1 1
50	463	2.7	1														1					1
49	435	2.6	1														1					1
39	>164***	2.3	1															1				
26	90	2.0	1															1				1
4	336	2.5	1															1				1
40	156	2.2	1																1			1
32	>336***	2.6	1																1			1
5	463	2.7	1																1			1
71	177	2.2																				
68	103	2.0																				1
63	404	2.6				1																
67	336	2.5				1																1
57	>164***	2.3				1																1
N-1	123	2.1	1																			1 1
N-2	115	2.1	1																			1 1
10	123	2.1	1												1							1
48	151	2.2	1												1							1
29	240	2.4	1												1							1 1
41	173	2.2	1														1					1
52	159	2.2	1														1				1	1
54	250	2.4	1														1				1	1 1
42	165	2.2	1															1				1
46	173	2.2	1															1				1 1
8	168	2.2	1															1				1
47	96	2.0	1																1		1	1
13	323	2.5	1																1			1
9	89	1.9	1																1		1	1
76	144	2.2																			1	1
69	252	2.4																				1
78	490	2.7																			1	1
56	250	2.4				1																1
62	324	2.5				1															1	1

* Failure caused by temperature excursion at either 455 or 290 hours.

** Specimen survived maximum available test time.

*** Specimen failed prior to first observation.

All the β_i and β_{ij} terms were initially fitted to the model. Some did not differ significantly from zero. An iterative process of dropping values which were not significant to the 10% confidence level was used to reduce the number of coefficients to the ten listed in Table 3.13. The estimate of the error standard deviation, s, was determined to be 0.290 (in log T terms) for the 71 degrees of freedom remaining.

Table 3.14 presents fitted values and 95% confidence intervals for average log T and T, as a function of intermediate layer, basecoat and overcoat layer. All independent variables in the final fitted model appear in Table 3.14 except for X19, which is fixed at 1/2 so as to average over the front and back rows of the furnace (in this way the nuisance variable X19 is both accounted for and removed from further consideration). The fitted values of log T are simple solutions of the model equation at the indicated combinations of the independent variables. Each entry in the bottom half of Table 3.14 is obtained by raising 10 to the power given by the corresponding entry in the top half.

The best coating system is then Inconel screen or no intermediate layer combined with the fine $ZrO_2 \cdot 8Y_2O_3$ plasma sprayed overcoat. This is followed closely by the 50% NiCrAlY + 50% ZrO_2 intermediate layer with the same overcoat. The next group of improved coatings consist of combinations of Inconel screen, 50% NiCrAlY + 50% ZrO_2 or no intermediate layers with 20% EK5 or EK7 Glass + fine $ZrO_2 \cdot 8Y_2O_3$ plasma sprayed overcoats. Feltmetal and 40% EK5 Glass + fine $ZrO_2 \cdot 8Y_2O_3$ tend to reduce lifetimes of the coatings. No statistically meaningful differences could be found between those with no overcoat and others such as sputter deposited, 20 and 40% other glasses + $ZrO_2 \cdot 8Y_2O_3$. They were therefore grouped together. This statistical conclusion might have not been reached if larger numbers of specimens of each type had been run. For example, the NASA baseline specimen lives (105 hours) fell below the 95% confidence level (141 hours) of the group which contained these plus the other overcoats. Had more baseline specimens been tested, the difference may or may not have been significant.

TABLE 3.13

STATISTICALLY SIGNIFICANT (10% LEVEL)
COEFFICIENTS IN TIME TO INITIAL FAILURE MODEL

$\log_{10}T$ = Fitted Value of $\log_{10}T$

= 2.3713	If (W) Basecoat No Intermediate Layer No Overcoat Layer Front Row of Furnace
- .1504 X_1	X_1 = 1 If NASA Basecoat, 0 Otherwise
- .3170 X_2	X_2 = 1 If Graded Interm. Layer, 0 Oth.
- .8270 X_5	X_5 = 1 If Feltmetal Interm. Layer, 0 Oth.
+ .5025 X_6	X_6 = 1 If Fine ZrO_2 Overcoat Layer, 0 Oth.
+ .3461 X_7	X_7 = 1 If ZrO_2 + 25% EK5 Glass Overc. L., 0 Oth.
- .7289 X_8	X_8 = 1 If ZrO_2 + 40% EK7 Glass Overc. L., 0 Oth.
+ .4101 X_9	X_9 = 1 If ZrO_2 + 20% EK7 Glass Overc. L., 0 Oth.
+ .0744 X_{19}	X_{19} = 1 If Back Row of Furnace, 0 Oth.
+ .5695 $X_2 X_{19}$	

TABLE 3.14

PREDICTED VALUES AND 95% CONFIDENCE INTERVALS FOR AVERAGE $\log_{10}T$ AND T
AS A FUNCTION OF INTERMEDIATE LAYER, BASECOAT AND OVERCOAT LAYER

		NONE & OTHERS		FINE ZrO_2		ZrO_2 + 25% EK5		ZrO_2 + 40% EK5		ZrO_2 + 20% EK7	
		FIT	95% CI	FIT	95% CI	FIT	95% CI	FIT	95% CI	FIT	95% CI
		FITTED VALUES OF $\log_{10}T$									
NO INTERM. LAYER & IN. 600 SCREEN	(W) BASECOAT	2.41	2.30-2.52	2.91	2.60-3.22	2.75	2.45-3.06	1.68	1.37-1.99	2.82	2.51-3.13
	NASA BC	2.26	2.15-2.37	2.76	2.43-3.09	2.60	2.27-2.94	1.53	1.19-1.86	2.67	2.43-3.00
50% NiCrAlY + 50% ZrO_2	(W) BASECOAT	2.38	2.21-2.55	2.88	2.55-3.21	2.72	2.39-3.05	1.65	1.32-1.98	2.79	2.46-3.11
	NASA BC	2.23	2.01-2.44	2.73	2.35-3.11	2.57	2.19-2.95	1.50	1.12-1.88	2.64	2.26-3.01
FELTMETAL	(W) BASECOAT	1.58	1.28-1.88	2.08	1.72-2.45	1.93	1.56-2.29	0.85	0.49-1.22	1.99	1.62-2.36
	NASA BC	1.43	1.11-1.75	1.93	1.53-2.33	1.78	1.38-2.18	0.70	0.30-1.10	1.84	1.44-2.24
		FITTED VALUES OF T									
NO INTERM. LAYER & IN. 600 SCREEN	(W) BASECOAT	256	199-329	815	400-1685	568	279-1157	48	23-97	659	324-1339
	NASA BC	181	141-232	576	267-1244	402	186-869	34	16-73	466	216-1002
50% NiCrAlY + 50% ZrO_2	(W) BASECOAT	238	161-352	756	354-1617	528	247-1126	44	21-95	612	289-1295
	NASA BC	168	102-278	535	223-1283	373	156-894	31	13-75	433	182-1026
FELTMETAL	(W) BASECOAT	38	19-76	121	53-280	85	37-196	7	3-16	98	42-229
	NASA BC	27	13-56	86	34-215	60	24-150	5	2-13	69	28-175

3.5.2.2 Failure Analysis. No failures occurred for the clean fuel tests which were run for 500 hours. This reflects the adequacy of the baseline coating with regard to thermal stress resistance. Further, the overcoats and intermediate layers did not degrade that resistance.

Failures did occur with the residual doped fuel (high V and Mg) tests. The specimens were subjected to extensive post test analyses which included X-ray diffraction, metallographic and electron microprobe analyses.

X-ray results indicated that deposits which formed on the coatings were primarily $MgSO_4$ (hydrated after burner rig exposure to $MgSO_4 \cdot 7H_2O$) with $Mg_3V_2O_8$ and MgO as minor phases. With regard to the phase stability of the zirconia coatings, the plasma sprayed $ZrO_2 \cdot 8Y_2O_3$ was primarily cubic and/or tetragonal[(h)] both before and after the tests. The minor phase was monoclinic, and in some cases it increased during the test.

An important finding from the X-ray analysis is that the cubic $ZrO_2 \cdot 20Y_2O_3$ overcoat of one specimen transformed almost completely to monoclinic after the test. This transformation probably resulted from the reaction between the Y_2O_3 in $ZrO_2 \cdot Y_2O_3$ and vanadium contained in the combustion gases and/or deposits. Since this transformation will lead to a destructive volume change on thermal cycling, this use of $ZrO_2 \cdot 20Y_2O_3$ coat may not provide much protection in combustion environments containing vanadium.

Electron microprobe scans were made to assess the possible causes of coating failures. An example of the Westinghouse baseline $ZrO_2 \cdot 8Y_2O_3$ which failed after 144 hours in the residual fuel is shown in Figure 3.11. Heavy concentrations of Mg, V and S were found on the specimen surface indicating deposits of $MgSO_4$, $Mg_3V_2O_8$ and MgO. This is in agreement with the findings of the X-ray analysis. The most important observation from the EMP scans is shown in Figure 3-12 which represents an interior area of the coating just above the NiCrAlY bond coat. Significant amounts of Na and S have penetrated through the continuous pores of the plasma

(h) Since the diffraction lines of the cubic and tetragonal phases are overlapping in this system, it is difficult to distinguish between the two.

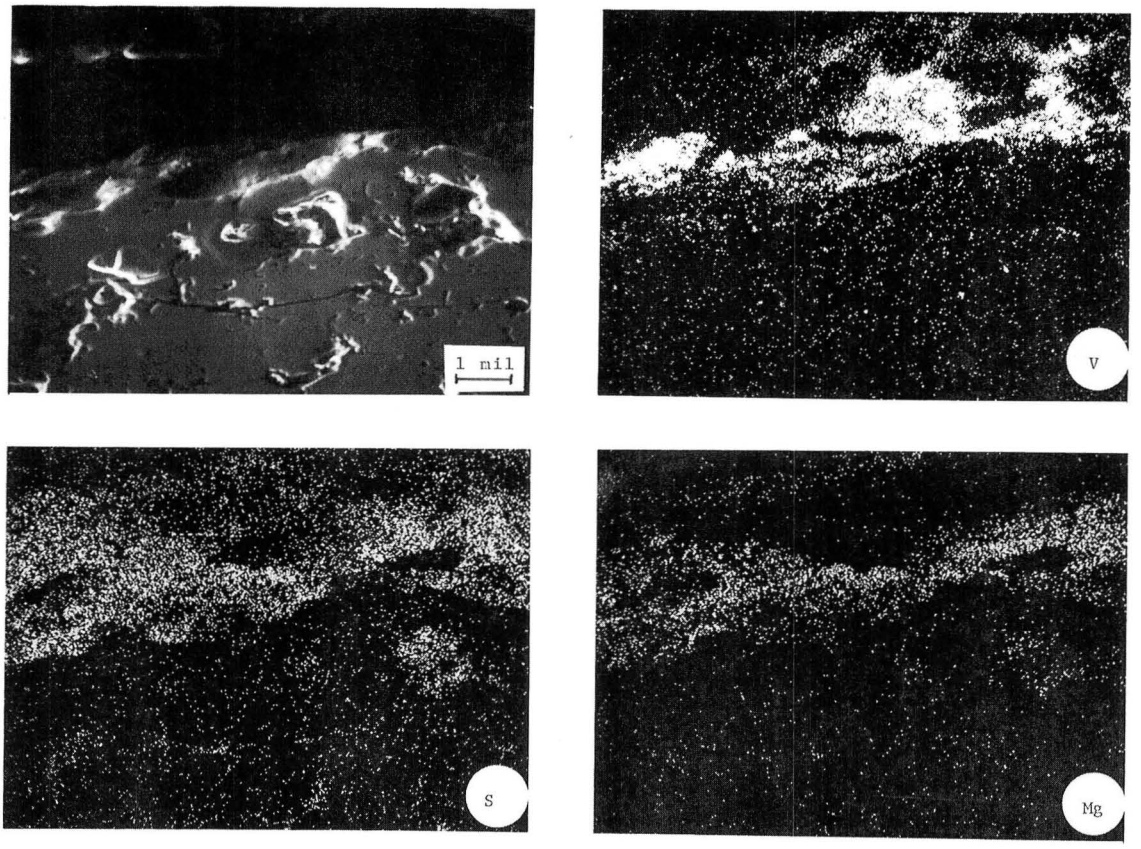

Figure 3.11 - Microprobe scans near exterior surface of a W-$ZrO_2 \cdot 8Y_2O_3$ coated specimen after exposure for 173 hours in the high vanadium fuel test (Run No. IA-D1)

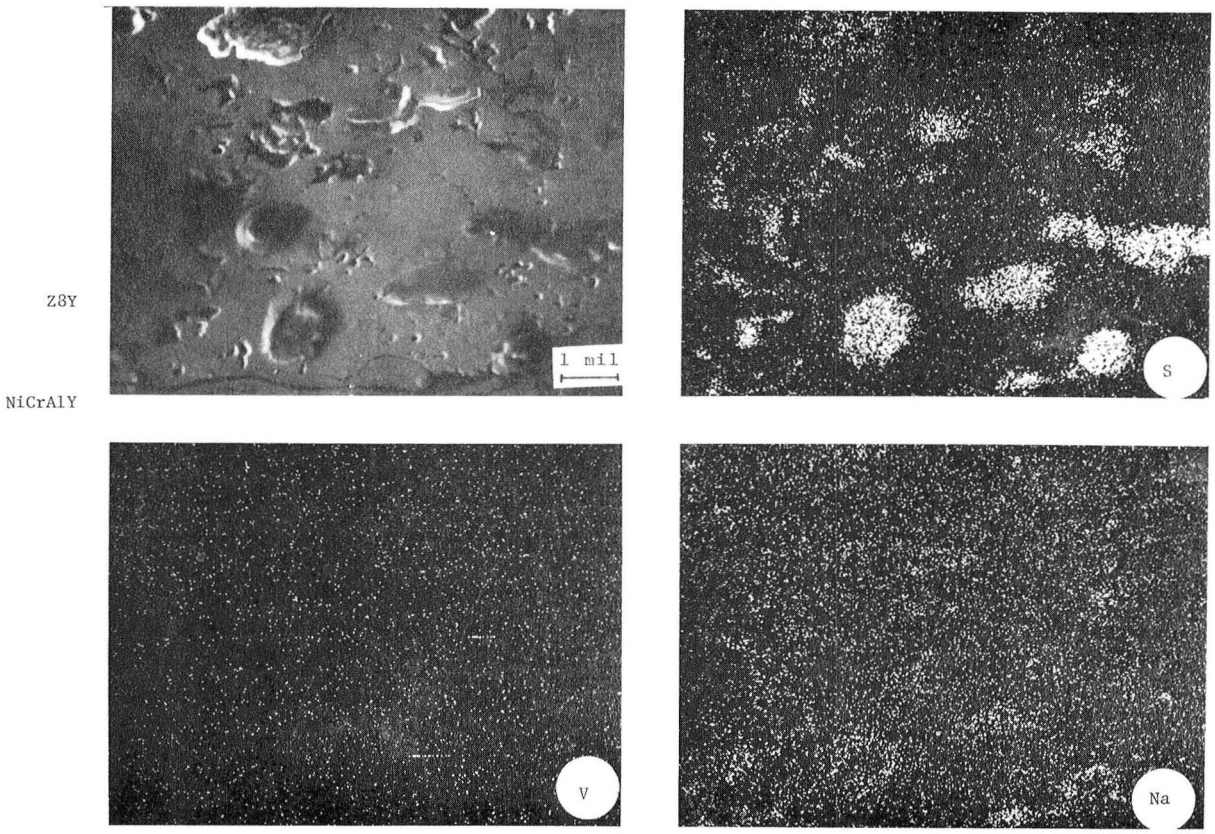

Figure 3.12 - Microprobe scans near bond coat of a W-$ZrO_2 \cdot 8Y_2O_3$ coated specimen after exposure for 173 hours in the high vanadium fuel test (Run No. IA-D1)

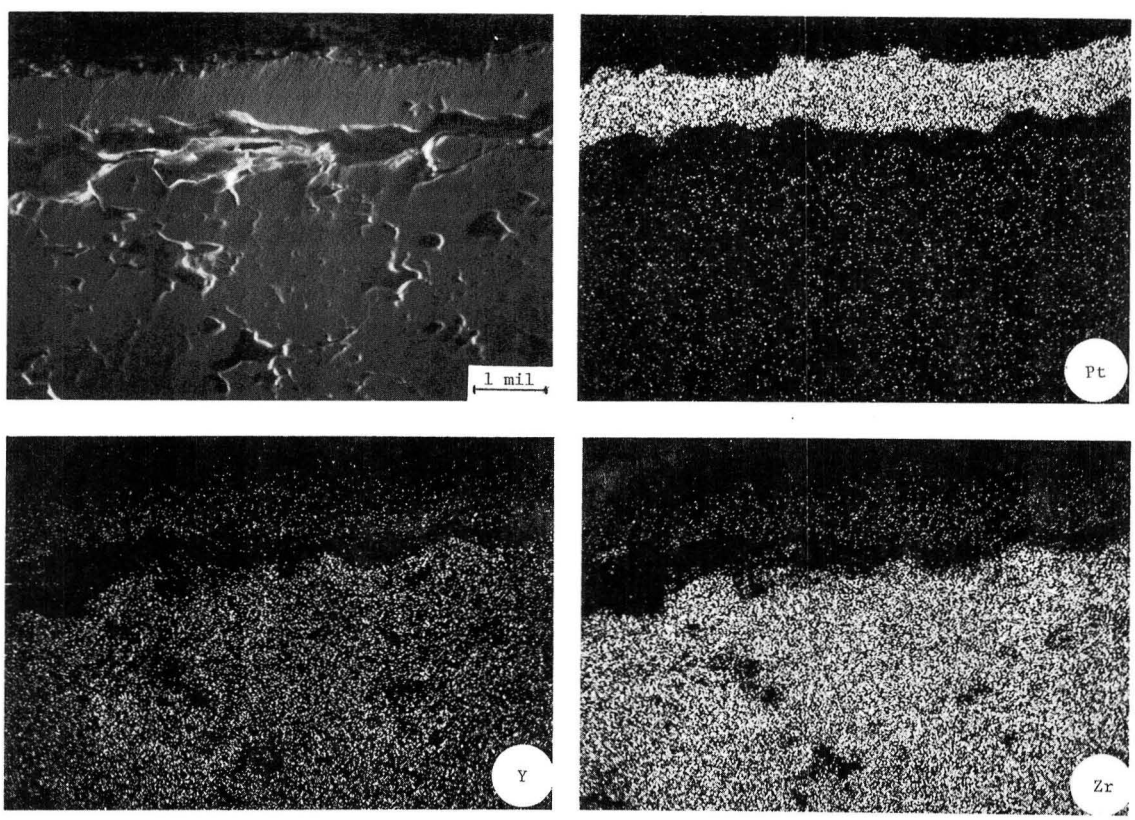

Figure 3.13 - Microprobe scans of a Pt graded to $ZrO_2 \cdot 20Y_2O_3$ overcoated specimen (0.75 mil nominal thickness) after exposure for 126 hours in the high vanadium fuel test (Run No. IA-D1)

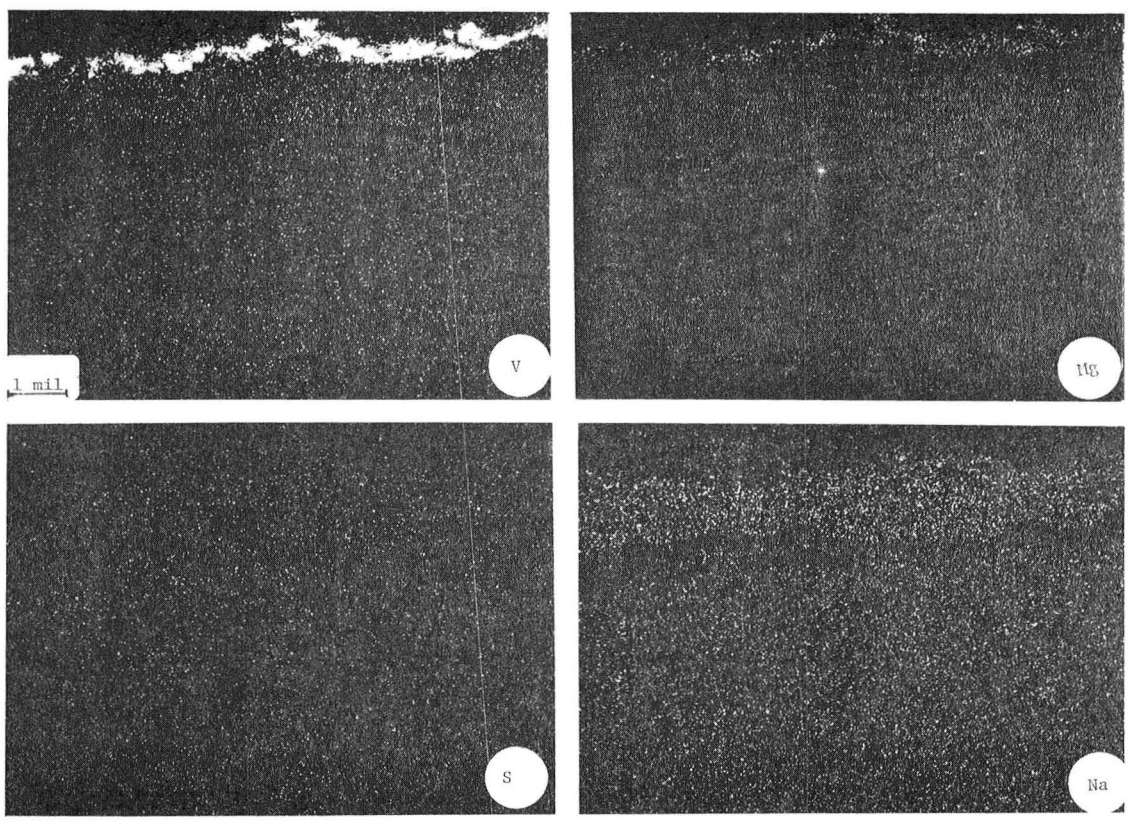

Figure 3.14 Microprobe scans of a Pt graded to $ZrO_2 \cdot 20Y_2O_3$ overcoated specimen (0.75 mil nominal thickness) after exposure for 126 hours in the high vanadium fuel test (Run No. IA-D1)

sprayed $ZrO_2 \cdot 8Y_2O_3$ coating and reached as deep as the ceramic/NiCrAlY interface. Therefore, the freezing and thawing of $Na_2SO_4/MgSO_4$ is probably responsible for failures in this fuel as well as in the sea salt doped fuels.

Figures 3-13 and 3-14 show the EMP scans of a Pt graded to $ZrO_2 \cdot 20Y_2O_3$ overcoated specimen that was tested for 126 cycles. It is important to note that S, Na and V did not penetrate through the overcoat into the interior of the plasma sprayed coating. Thus, the use of this overcoat was effective in retarding the penetration of detrimental contaminants into the coating interior for this time.

X-ray analyses of the coating surfaces after running in the combustion products of the sea salt doped fuel showed that the deposits were Na_2SO_4 (major) with some minor traces of spinel and Fe_2O_3. The sources of the latter two are the stainless steel fittings which were badly corroded during the test runs. The structure of the plasma sprayed $ZrO_2 \cdot 8Y_2O_3$ consisted mainly of tetragonal and/or cubic. The structure of the PVD $ZrO_2 \cdot 8Y_2O_3$ was also primarily tetragonal and/or cubic with minor amounts of monoclinic.

Electron microprobe analysis of the baseline coatings showed that Na_2SO_4 had penetrated into the pores of the plasma sprayed ceramic, in a similar manner to that shown in Figures 3.11 and 3.12. Although the sputtered overcoats retard the initial penetration of the contaminant, it eventually penetrates at longer times as indicated in Figure 3.15. In this case, the overcoat cracked, lost adherence overall, and allowed massive impregnation. In other cases, Na_2SO_4 penetrated through smaller flaws in the overcoats. Thus, the sputtered overcoats applied in this program tend only to delay salt penetration with an approximate doubling of the time to initial failure.

Once the Na_2SO_4 penetrated the coatings containing wire screen intermediate layers, screen and bond coat hot corrosion might be expected. However, no large scale attack has been detected. As shown in Figure 3.16,

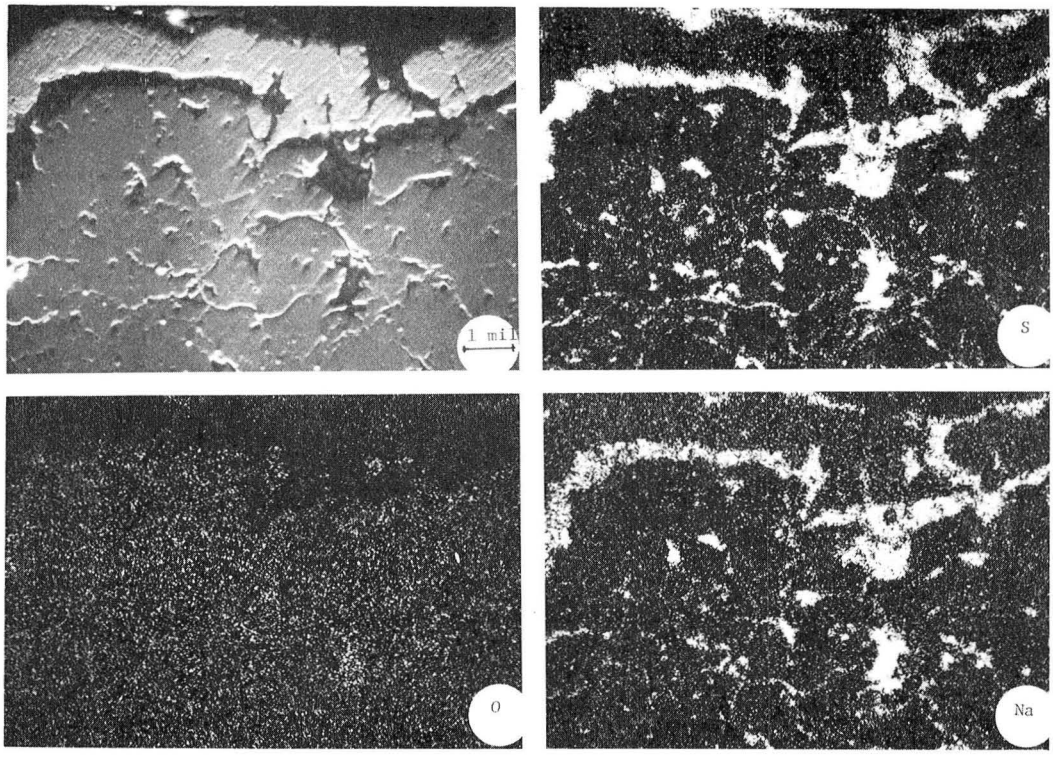

Figure 3.15 - Electron microprobe scans of a Pt overcoated (0.6 mil nominal thickness) plasma sprayed $ZrO_2 \cdot 8Y_2O_3$ basecoated specimen after exposure for 336 hours in the sea salt doped (100 ppm Na) fuel test

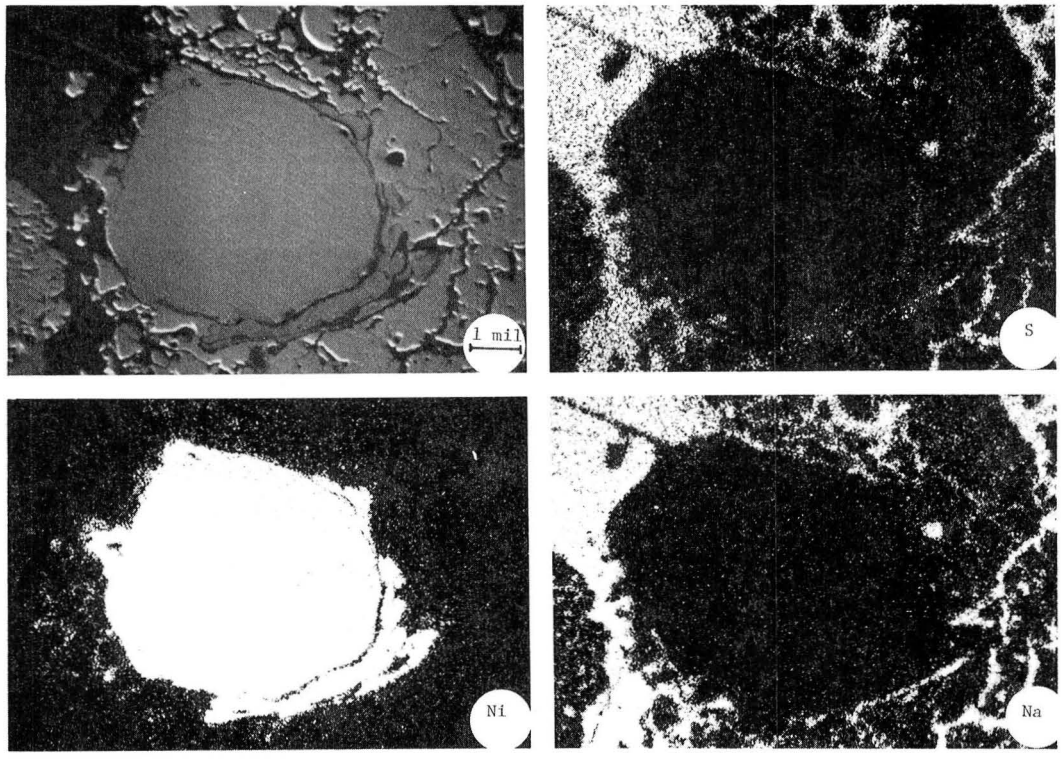

Figure 3.16 - Electron microprobe scans of Inconel 600 wire screen intermediate layer with plasma sprayed $ZrO_2 \cdot 8Y_2O_3$ basecoat after exposure for 500 hours in the sea salt doped (100 ppm Na) fuel test

the Na_2SO_4 is contained within the pores and fissures in the ceramic. Both the wire and the plasma sprayed NiCrAlY attached to it are free of Na or S indicating that no extensive corrosion took place. Attack of the bond coating by Na_2SO_4 in the ceramic coating pores is also not common even though regions just outside ceramic coverage may suffer severe corrosion. Thus, the presence of $ZrO_2 \cdot 8Y_2O_3$ seems to retard metallic corrosion. The chemistry of these observations is not understood.

The coatings which demonstrated the best lifetimes in the sea salt fuel tests were those with plasma sprayed fine $ZrO_2 \cdot 8Y_2O_3$ and fine $ZrO_2 \cdot 8Y_2O_3$ + 20 to 25% glass overcoats. In the latter case, the glass acted to fill the pores in the zirconia overcoat and prevented contaminant salt penetration. This is illustrated in the EMP scans of Figure 3.17 for a coating that was exposed for 500 hours. The pores in the overcoat shown in the SEM at the upper left-hand corner are shown to contain both Si and Na (two of the elements in the glass composition) by the bottom two scans. However, negligible S is present in the upper right hand scan. Similarly, scans taken near the bond coat show no appreciable Na_2SO_4 penetration in Figure 3.18.

The corrosion protection mechanism of the fine $ZrO_2 \cdot 8Y_2O_3$ overcoat is uncertain. Microprobe scans taken at both the overcoat and bond coat layers, Figures 3.19 and 3.20, indicate heavy penetration of Na_2SO_4 which should lead to failure. The fine pore structure of the overcoat may have acted to retard the kinetics of the salt infiltration, thus prolonging coating lifetime. This coating might be expected to eventually fail by the same mechanism as the baseline coating.

The physical vapor deposited coatings investigated had two types of microstructures. Four of the six were of the columnar type shown in Figure 3.21 and two were of the equiaxed type also shown in the figure. It is clear why both of these coatings were susceptible to thermal stress

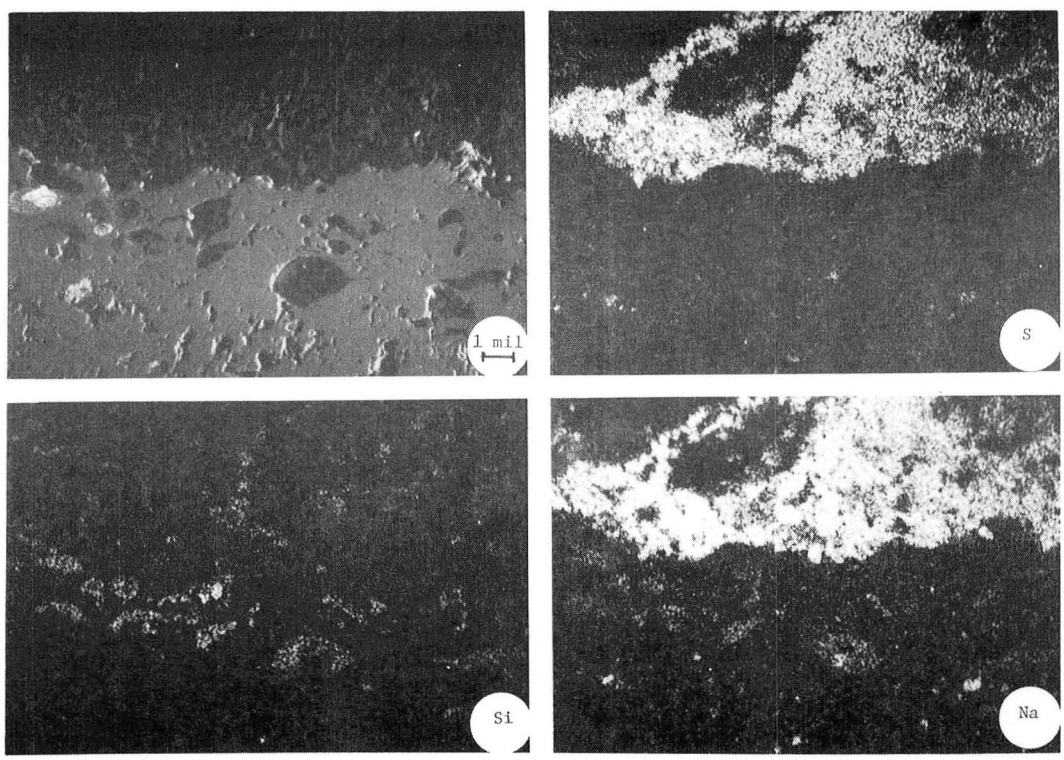

Figure 3.17 - Electron microprobe scans taken near the surface of a plasma sprayed fine $ZrO_2 \cdot 8Y_2O_3$ + 20% EK7 glass overcoated plasma sprayed $ZrO_2 \cdot 8Y_2O_3$ basecoated specimen after exposure for 500 hours in sea salt doped (100 ppm Na) fuel test

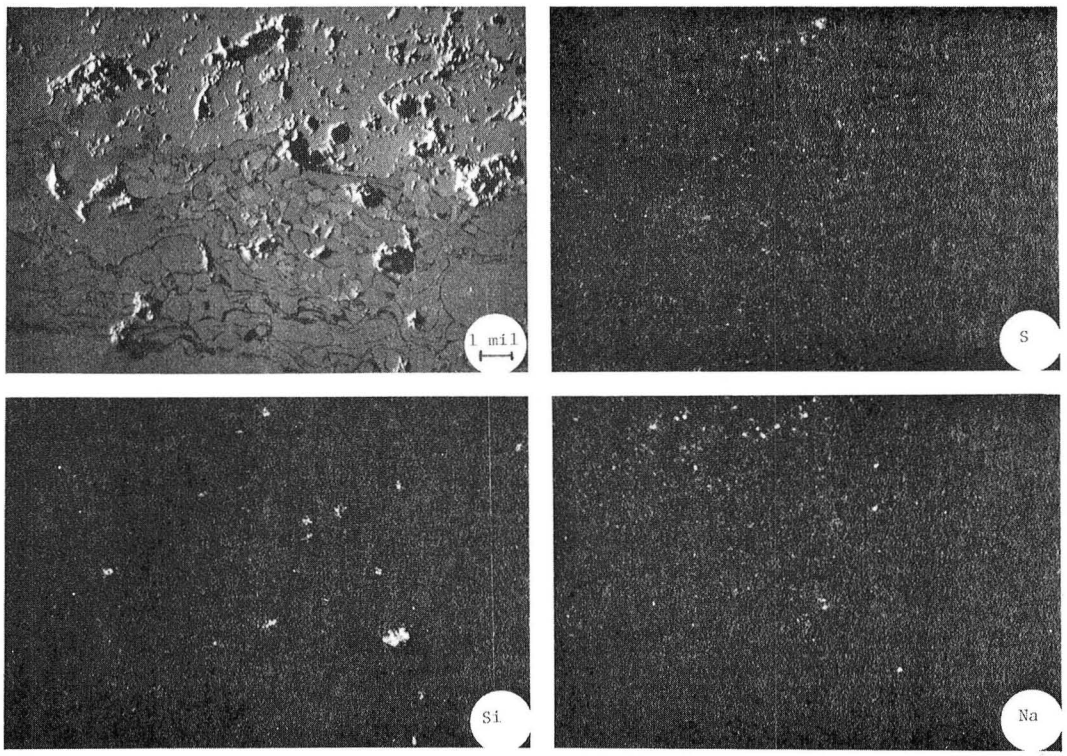

Figure 3.18 - Electron microprobe scan taken near bond interface of a plasma sprayed fine $ZrO_2 \cdot 8Y_2O_3$ + 20% EK7 glass overcoated plasma sprayed $ZrO_2 \cdot 8Y_2O_3$ basecoated specimen after exposure for 500 hours in sea salt doped (100 ppm Na) fuel test

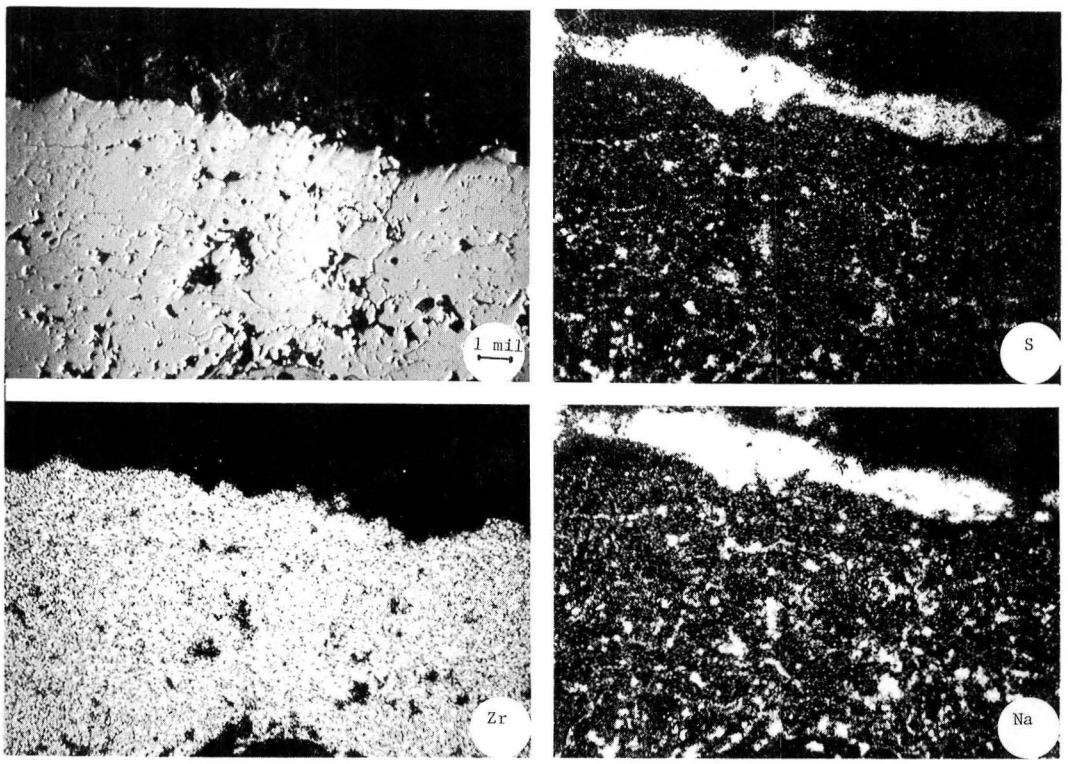

Figure 3. [19] - Electron microprobe scans taken near the surface of a plasma sprayed fine $ZrO_2.8Y_2O_3$ overcoated plasma sprayed $ZrO_2.8Y_2O_3$ base coated specimen with Inconel screen intermediate layer after exposure for 500 hours in sea salt doped (100 ppm Na) fuel test

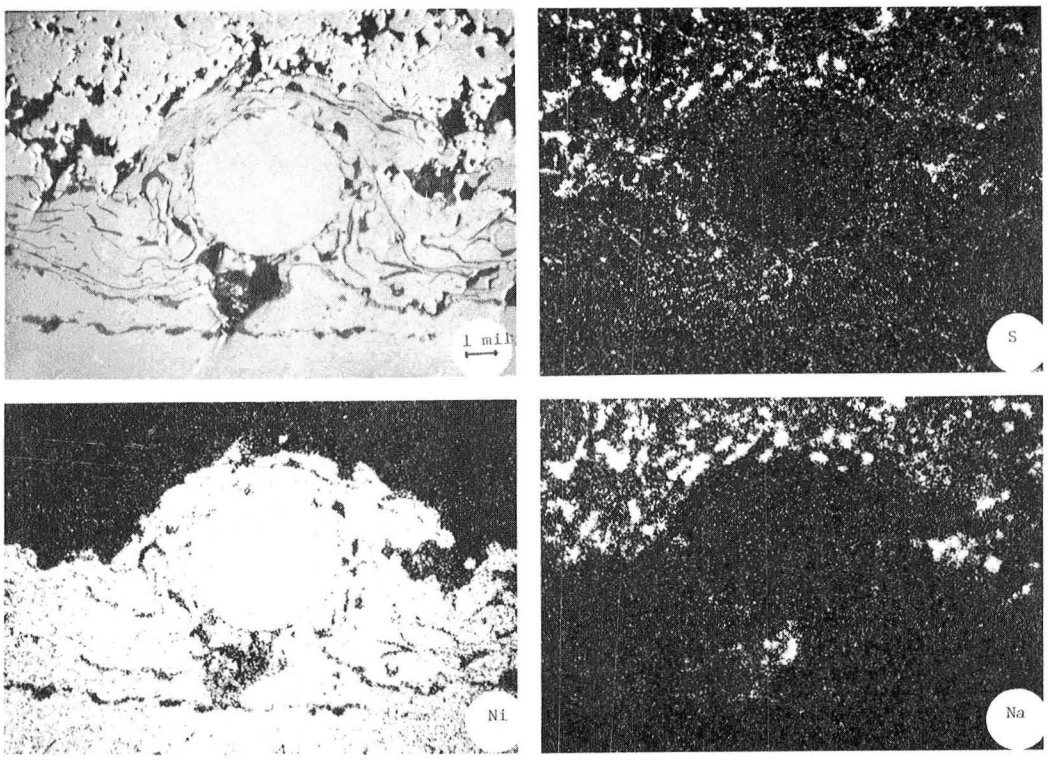

Figure 3 .20- Electron microprobe scans taken near bond interface of a plasma sprayed fine $ZrO_2 \cdot 8Y_2O_3$ overcoated plasma sprayed $ZrO_2 \cdot 8Y_2O_3$ basecoated specimen with Inconel screen intermediate layer after exposure for 500 hours in sea salt doped (100 ppm Na) fuel test

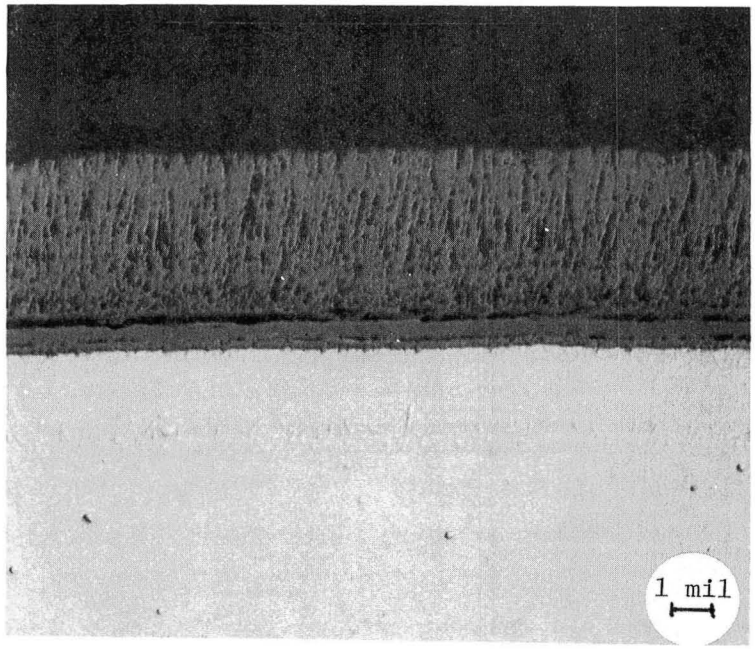

a) AT9

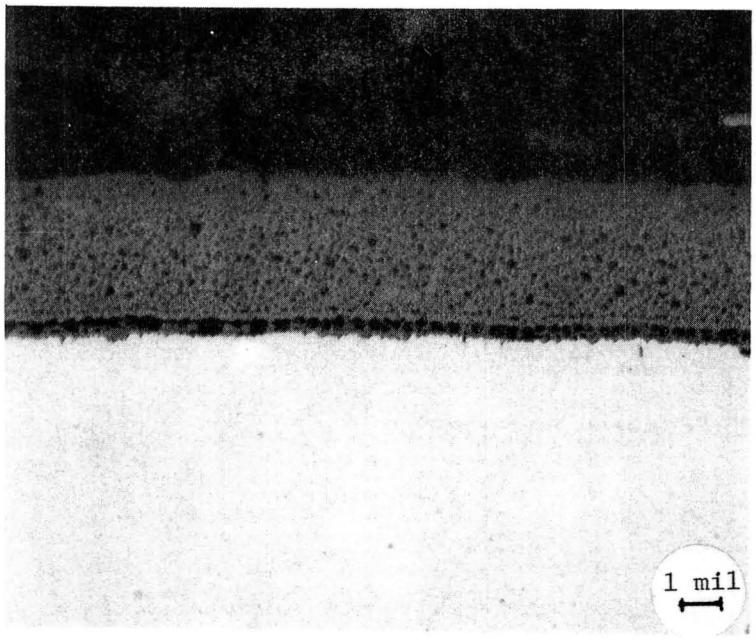

b) AT3

Figure 3.21 - Two types of coating structures produced by physical vapor deposition of $ZrO_2 \cdot 8Y_2O_3$

failures: both have gross defect structures in the ceramic layers near the bond interface which are obvious weaknesses where strength is most required.

The segmented structure shown in the top of Figure 3.21 is the one that has been sought after for thermal stress resistance (minus the defective layer near the bond coating). As shown in Figure 3.22, this structure might not be preferred for corrosion resistance. The aligned pores and fissures act as direct paths for penetration of the contaminants.

The structure at the bottom of Figure 3.21 would be preferred for corrosion resistance if the sperical pores were isolated. The coating compliance could be increased without allowing impregnation by contaminants. Unfortunately, as shown in Figure 3.23, the pores are interconnected and they contain Na_2SO_4.

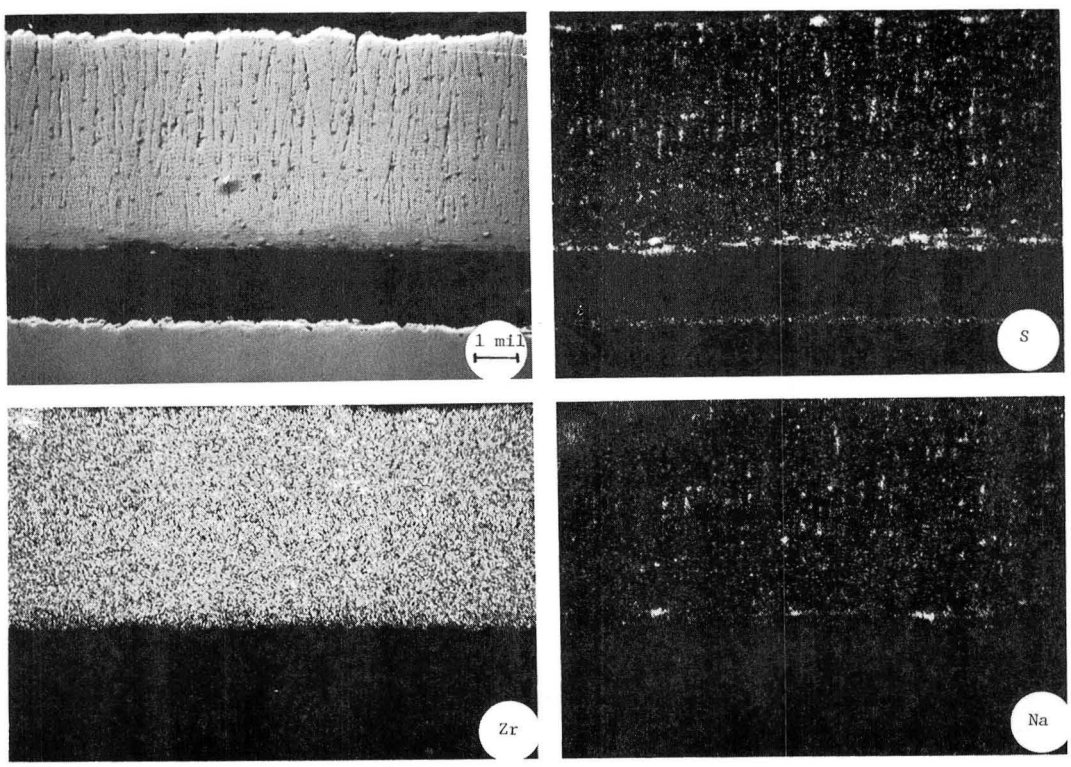

Figure 3.22 - Electron microprobe scans of physical vapor deposited $ZrO_2 \cdot 8Y_2O_3$ (AT9) after exposure for 166 hours in the sea salt doped (100 ppm Na) fuel test

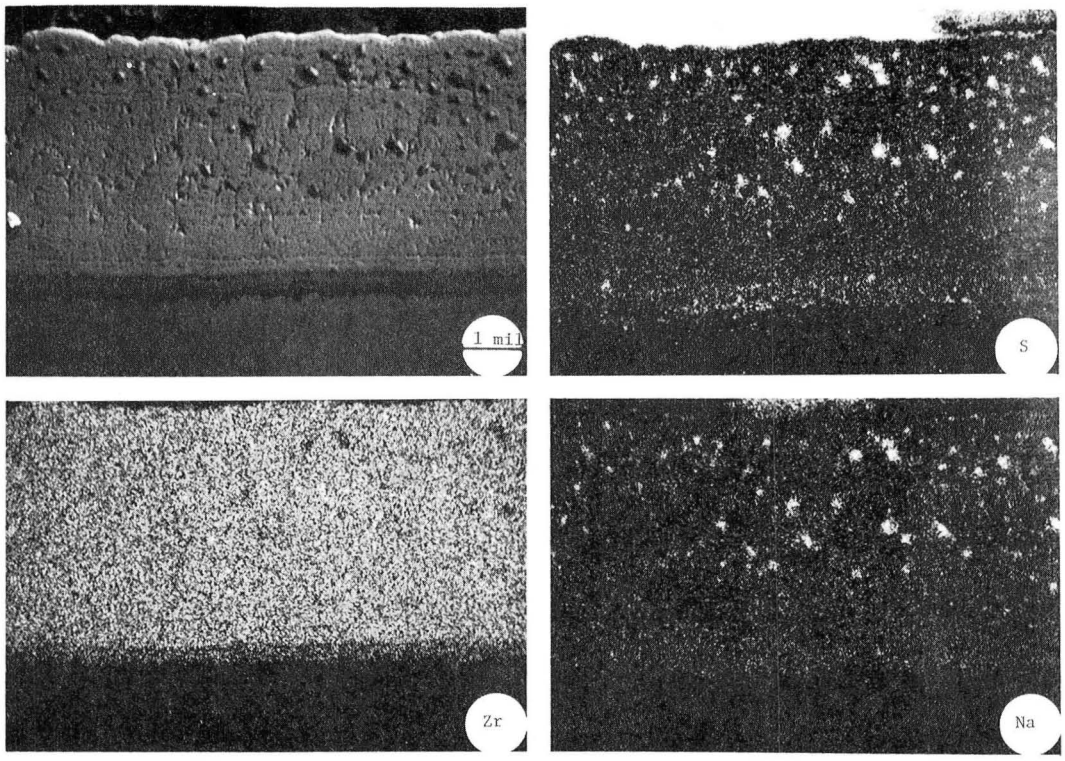

Figure 3.[23] - Electron microprobe scans of physical vapor deposited $ZrO_2 \cdot 8Y_2O_3$ coating (AT3) after exposure for 166 hours in the sea salt doped (100 ppm Na) fuel test

4.0 COATING PROPERTIES

The objective of Task IB - Thermomechanical Property Screening was first to obtain the physical properties of the coatings including:

- Thermal Conductivity
- Coefficient of Thermal Expansion
- Elastic Properties
- Density

over the temperature range of use. The second objective was to determine the coating failure properties, including:

- Strength
- Fracture Toughness
- Cyclic Subcritical Crack Growth

The effort was planned to be a limited one, thus the numbers of specimens tested were too few to obtain statistical certainty for many of the values. The materials, test procedures and results are presented in this section.

4.1 Materials

The coating materials selected for the later stages of development were based on the $ZrO_2 \cdot 8Y_2O_3$/NiCrAlY system. The property evaluations were limited to these two plasma sprayed materials. The specifications and application procedures were presented in the Coating Development Section.

4.2 Experimental Procedures

4.2.1 Thermal Conductivity

The specimens for thermal diffusivity measurements consisted of 12.7 mm (0.5 inch) diameter disks of the individual components ($ZrO_2 \cdot 8Y_2O_3$, NiCrAlY and U720) and of composites of the three. Thicknesses ranged between 1.0 and 2.0 mm (40 and 80 mils). Two particle sizes of the plasma sprayed ceramic (-200 + 325 mesh and -270 mesh + 10 μm) and one of the bond coat (-200 + 325 mesh) were evaluated.

Thermal diffusivity was measured by the laser-flash technique over the temperature range of 298 to 1373 to 298K (77 to 2012 to 77°F).[a] A single flash from the laser irradiated the front face of the specimen and the time, $t_{1/2}$, for the temperature to reach one half its final value was measured. The diffusivity, α, was then calculated from

$$\alpha = CL^2/t_{1/2} \quad (1)$$

where C is a constant and L is the specimen thickness. The thermal conductivity was calculated from

$$K_c = \alpha\rho\ C_p \quad (2)$$

where ρ is the density and C_p is the heat capacity.

4.2.2 Coefficient of Thermal Expansion

The specimens for measuring thermal expansion consisted of plasma sprayed bars of $ZrO_2 \cdot 8Y_2O_3$ measuring 51 x 6.4 x 3.2 mm (2 x 0.25 x 0.125 in.) The measurements were made with an alumina dilatometer using standard procedures.

4.2.3 Tensile Tests Parallel to the Bond Interface

Thin wall specimens machined from 13.1 mm (0.514 in.) diameter,

---

(a) Prof. D.P.H. Hasselman, Virginia Polytechnic Institute and State University, Blacksburg, VA

0.43 mm (0.017 in.) wall thickness Inconel 718 were used to measure the tensile elastic properties and the load bearing capacities of the coating components. The tubes were cut to 56 cm (22 in.) lengths and the centrally located 7.6 cm (3 in.) gauge sections machined to a wall thickness of 0.230 mm (0.009 in.). Some of the tubes were tested with no coating, some with NiCrAlY only and others with $ZrO_2 \cdot 8Y_2O_3$/NiCrAlY applied. The coatings were applied over all but the last 3 cm near the ends. Coarse mesh powders were used for plasma spraying to respective nominal bond and ceramic coating thicknesses of 150 μm (0.006 in.) and 330 μm (0.013 in.).

Specimens were loaded in a universal test machine through compression fittings on the reinforced specimen ends. Gauge section extension was measured by a calibrated extensometer. Room temperature axial and transverse strains were determined with resistance strain gauges, as well. Properties at 300, 810, 980, 1140, 1260 and 1370°K (75, 1000, 1300, 1600, 1800 and 2000°F) were determined by inserting the central portions of the specimens in an electrical resistance furnace.

The load carried by each constituent was determined by a force balance method. That is, the load carried by the bond coat on a NiCrAlY/IN-718 composite was determined by subtracting the load carried by the previously measured substrate material from the total. Similarly, the load carried by the ceramic on a $ZrO_2 \cdot 8Y_2O_3$/NiCrAlY/IN-718 was determined by subtracting the two metallic layer loads from the total.

4.2.4 Compression Tests Parallel to the Bond Interface

Specimens for measuring elastic properties and coating load bearing capacity in compression were machined from the same thin walled tubular material as the tensile specimens. These measured 5.7 cm (2.25 in.) in length and had a 3.2 cm (1.25 in.) long gauge section reduced to a wall thickness of 0.23 mm (.009 in).

Test procedures were also similar, except that the compression load was applied with ceramic plattens.

4.2.5 Shear Tests

Shear moduli were determined on 17.8 cm (7 in.) long, 0.43 mm (0.017 in.) wall thickness Inconel 718 tubing which were tested in torsion. Specimen preparation was similar to that used for the tensile and compression specimens.

Torques versus angular deflections were determined for coated and uncoated specimens over the same temperature range. A torque balance treatment was used to separate out the contribution of each constituent of the coated alloy tubes.

4.2.6 Transverse Tensile Tests

Specimens to determine the strengths of plasma sprayed coatings in the direction normal to the bond interface consisted of pairs of 15.2 mm (0.6 in.) diameter by 19.1 mm (0.75 in.) long cylinders, having female threads tapped into one end of each. The unthreaded ends of each pair were plasma sprayed. One of each pair was sprayed with 127 μm (0.005 in.) NiCr/254 μm (.010 in.) $ZrO_2 \cdot 8Y_2O_3$/127 μm (0.005 in.) NiCr layers and the other of the pair with 127 μm (0.005 in.) NiCr only. The surfaces were ground flat and brazed together.

The specimens were threaded onto the rods and loaded to failure over the same temperature range as the other specimens.

4.2.7 Fracture Toughness

The critical strain energy release rate, G_{I_c}, was determined with double cantilever beam, DCB, specimens. This configuration is well suited to determining fracture properties of bonds, since it was originally developed to determine fracture properties of adhesives. Another advantage is that several toughness values can be obtained with each specimen. The specimens were prepared by first plasma spraying the 6.4 x 178 mm (0.25 x 7 in.) surface of a 12.7 mm (0.5 in.) high rectangular bar of stainless steel with the NiCrAlY bond coat. This surface was

then oversprayed with the zirconia and epoxy bonded to another stainless steel bar of the same dimensions. Loading pin holes 3.2 mm (0.125 in.) in diameter were drilled 12.7 mm (0.5 in.) from one end in each of the bar halves. A starter notch was sawed into the plasma sprayed coating at the ends containing the holes.

The specimens were clevis pinned to tie rods attached to the test machine, and a strain gauge clip gauge used to measure crack opening displacement. The initial loading was used to pop in a natural crack from the saw cut. Thereafter, five to six successive crack propagating loads were applied. Crack lengths were determined from compliance calibration, i.e., the compliance of a similar specimen was measured after saw cuts were made to various depths in the coating.

Cyclic crack growth rates were measured on DCB specimens prepared in the same manner. After the initial natural crack was popped in, the test machine was load cycled between 0 and 25% of the initial pop in load. The load and displacements were autographically recorded, and numbers of cycles counted. Crack growth was measured by monitoring the compliance. As the crack grew, the stress intensity increased. Thus, a wide range of growth rates as functions of cyclic stress intensity was determined on a single specimen.

4.3 Results

4.3.1 Thermal Conductivity

The thermal diffusivities measured during heating and cooling for plasma sprayed NiCrAlY and plasma sprayed $ZrO_2 \cdot 8Y_2O_3$ (coarse and fine mesh) as functions of temperature are presented in Figures 4.1 through 4.3. The room temperature NiCrAlY diffusivity more than doubles after the thermal cycle indicating that the material had sintered. The $ZrO_2 \cdot 8Y_2O_3$ room temperature diffusivity decreases by 10 to 15 percent, accompanied by a slight thickness increase. This is possibly associated with crack formation in the ceramics.

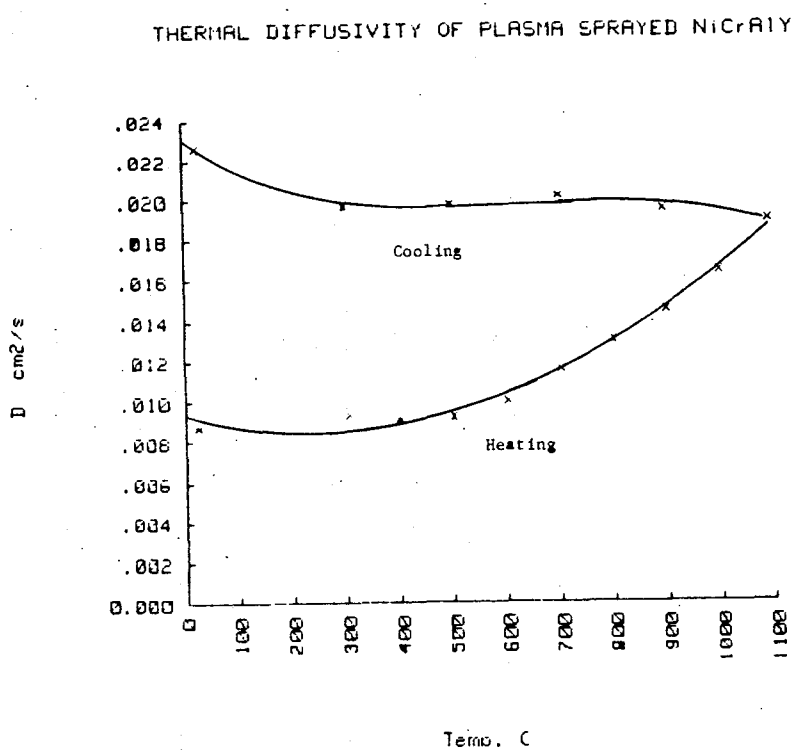

Figure 4.1 - Thermal diffusivity of coarse particle (-200 + 325 mesh) plasma sprayed NiCrAlY bond coating.

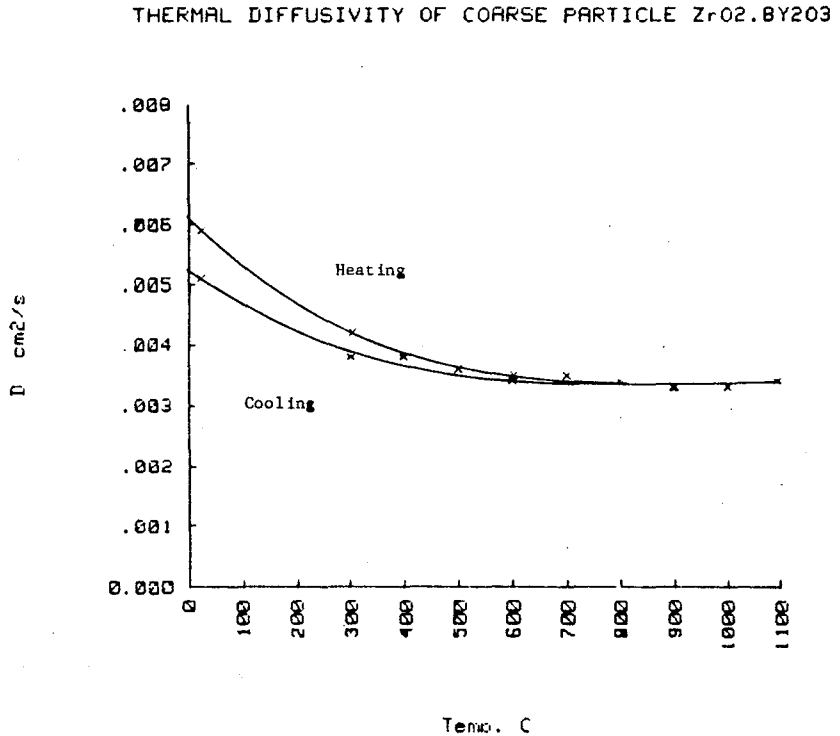

Figure 4.2 - Thermal diffusivity of coarse particle (-200 + 325 mesh) plasma sprayed $ZrO_2 \cdot 8Y_2O_3$ coating.

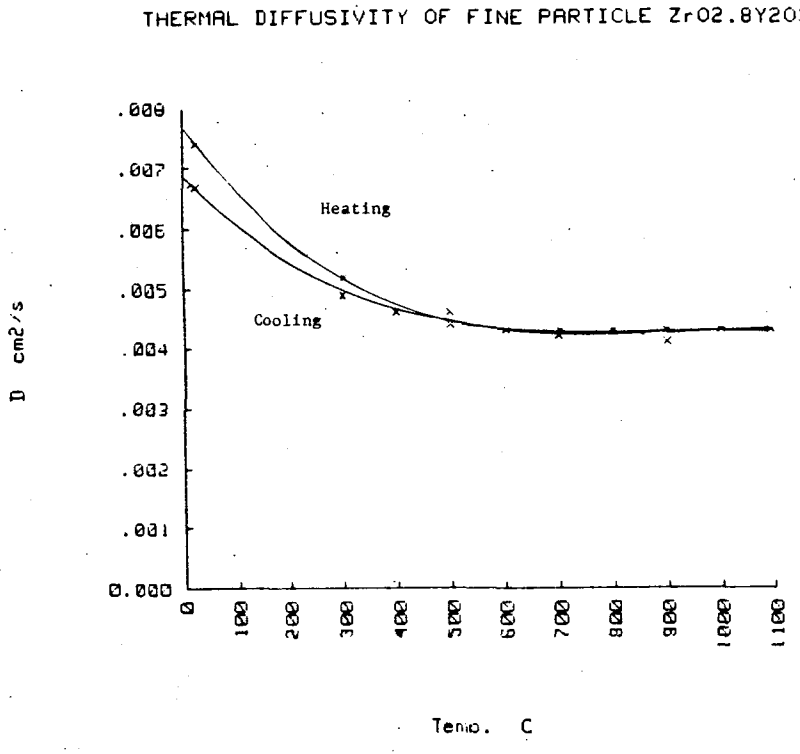

Figure 4.3 - Thermal diffusivity of fine particle (-270 mesh + 10 μm) plasma sprayed $ZrO_2 \cdot 8Y_2O_3$ coating.

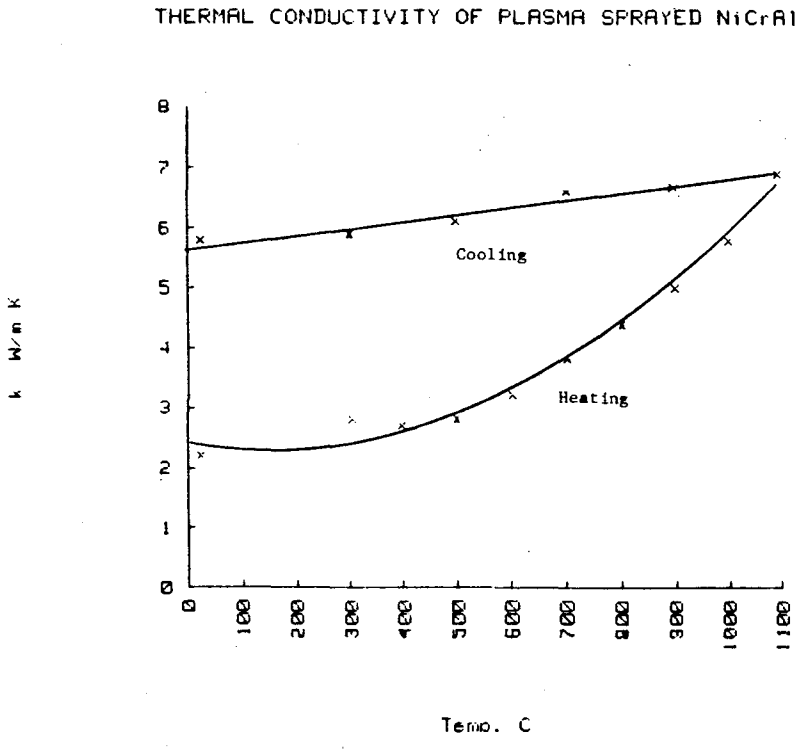

Figure 4.4 - Thermal conductivity of coarse particle (-200 +325 mesh) plasma sprayed NiCrAlY bond coating.

Thermal conductivities were calculated from the diffusivities, densities and from calculated values of specific heat. These are presented in Figures 4.4 through 4.6. Note that the denser fine $ZrO_2 \cdot 8Y_2O_3$ has ∿20% higher thermal conductivity.

4.3.2 Thermal Expansion

A plot of the thermal expansion of plasma sprayed $ZrO_2 \cdot 8Y_2O_3$ (coarse mesh) is presented in Figure 4.7. The average coefficients as a function of temperature are presented in Figure 4.8.

4.3.3 Elastic Properties

The elastic moduli measured in tension and compression as functions of temperature for $ZrO_2 \cdot 8Y_2O_3$ and NiCrAlY are given in Figures 4.9 to 4.12, and the shear moduli in Figures 4.13 to 4.14.

Room temperature Poisson's ratio measured on the NiCrAlY coated specimen was 0.27 in tension and compression, and on the $ZrO_2 \cdot 8Y_2O_3$/ NiCrAlY coated specimen 0.24 in tension and 0.26 in compression.

4.3.4 Density

The density of the plasma sprayed NiCrAlY was determined by standard water immersion techniques to be 6210 kg/m^3. The densities of the fine mesh and coarse mesh $ZrO_2 \cdot 8Y_2O_3$ were 5830 and 5610 kg/m^3, respectively.

4.3.5 Coating Stress Bearing Capacity

Both tensile and compression specimens were tested to failure. The stress bearing capacities of each constituent of the coated alloy tubes were calculated from force balances. That is, the stresses in the zirconia and bond coat were determined at a given strain value: 0.4% in tension and 0.8% in compression. These values are plotted in Figures 4.15 through 4.18 and multilinear regression analysis curves drawn through them. The equations for the curves and the standard errors are also included.

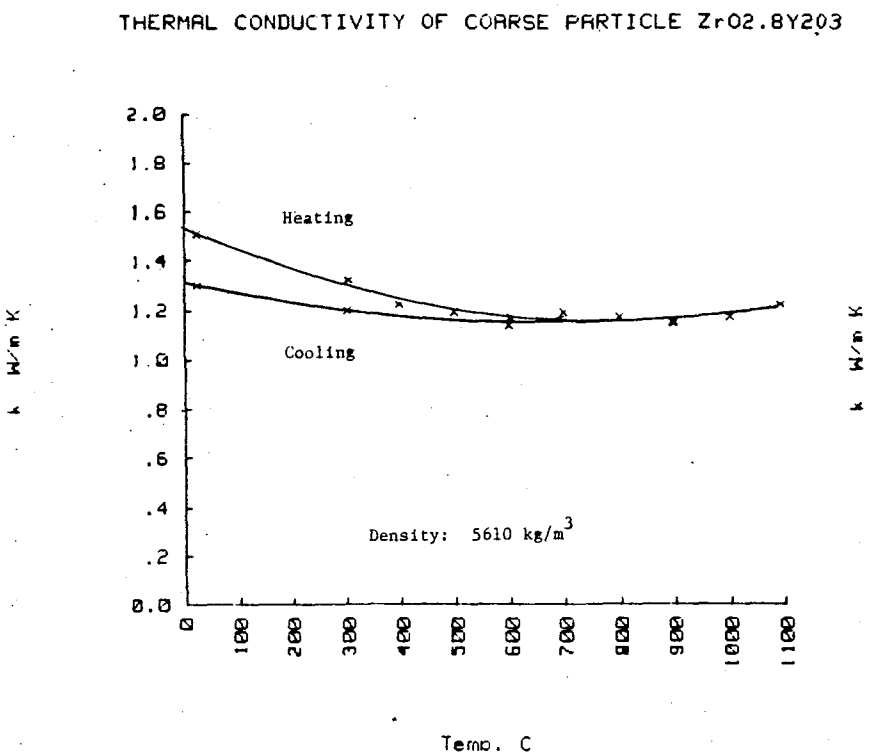

Figure 4.5 - Thermal conductivity of coarse particle (-200 + 325 mesh) plasma sprayed $ZrO_2 \cdot 8Y_2O_3$ coating.

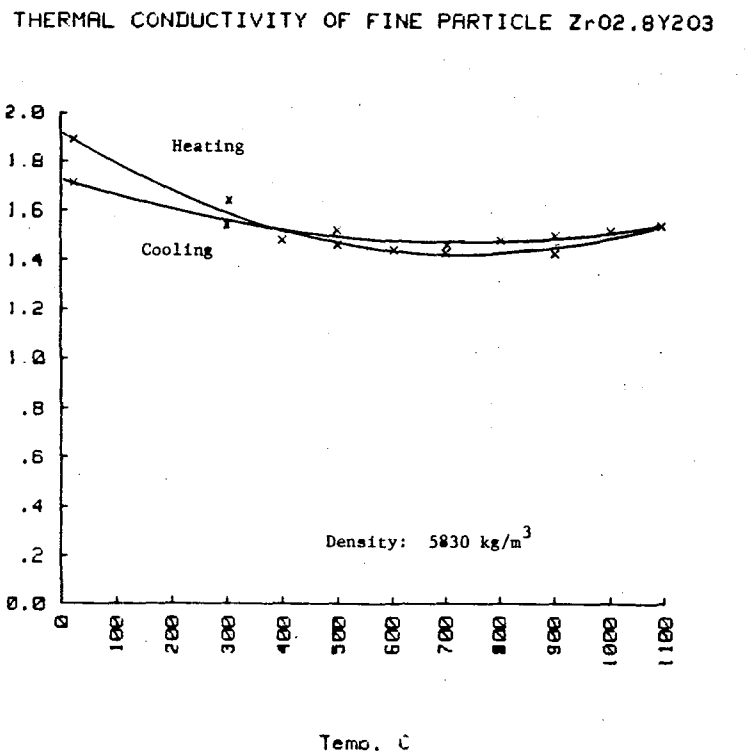

Figure 4.6 - Thermal conductivity of fine particle (-270 mesh + 10 μm) plasma sprayed $ZrO_2 \cdot 8Y_2O_3$ coating.

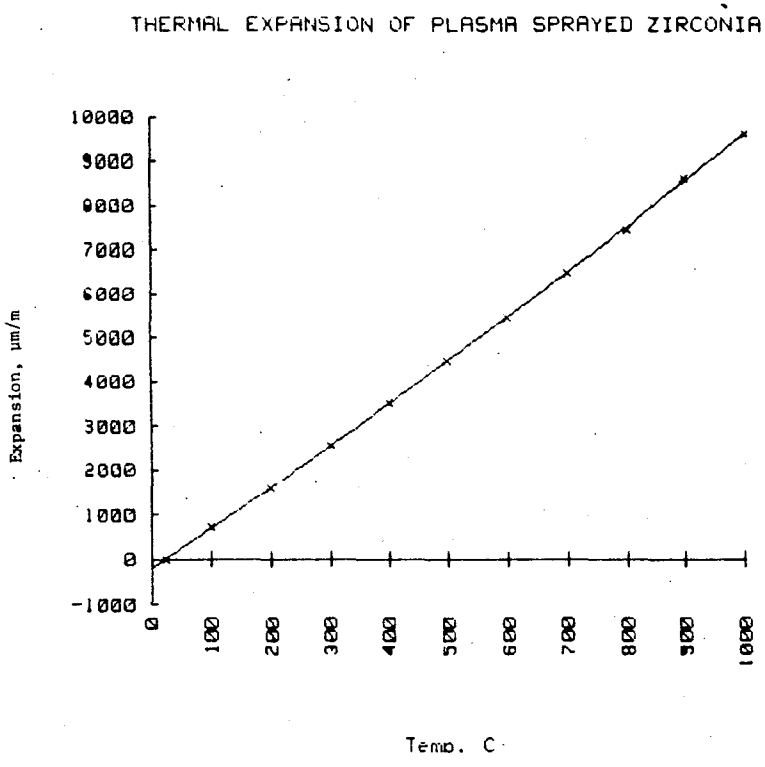

Figure 4.7 - Thermal expansion of coarse mesh (-200 + 325 mesh) plasma sprayed $ZrO_2 \cdot 8Y_2O_3$.

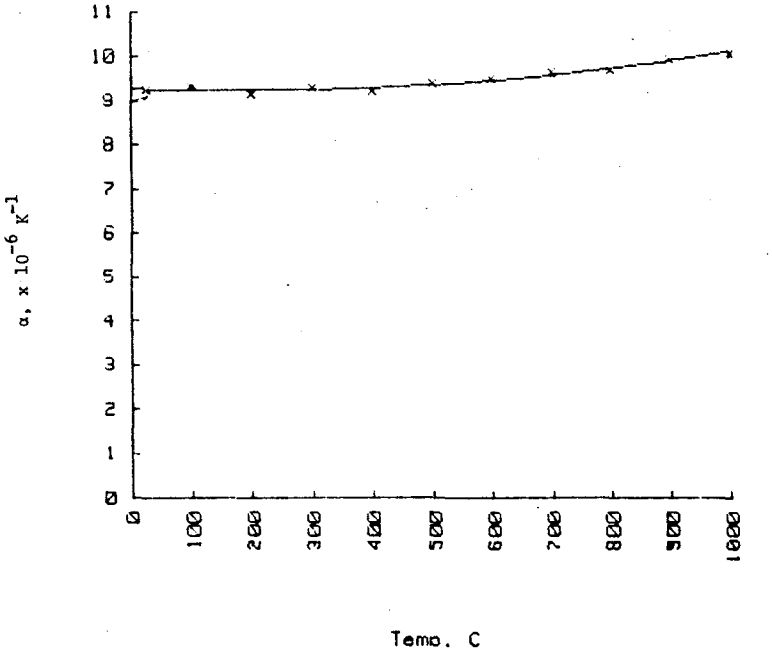

Figure 4.8 - Average coefficient of thermal expansion of coarse particle (-200 + 325 mesh) plasma sprayed $ZrO_2 \cdot 8Y_2O_3$.

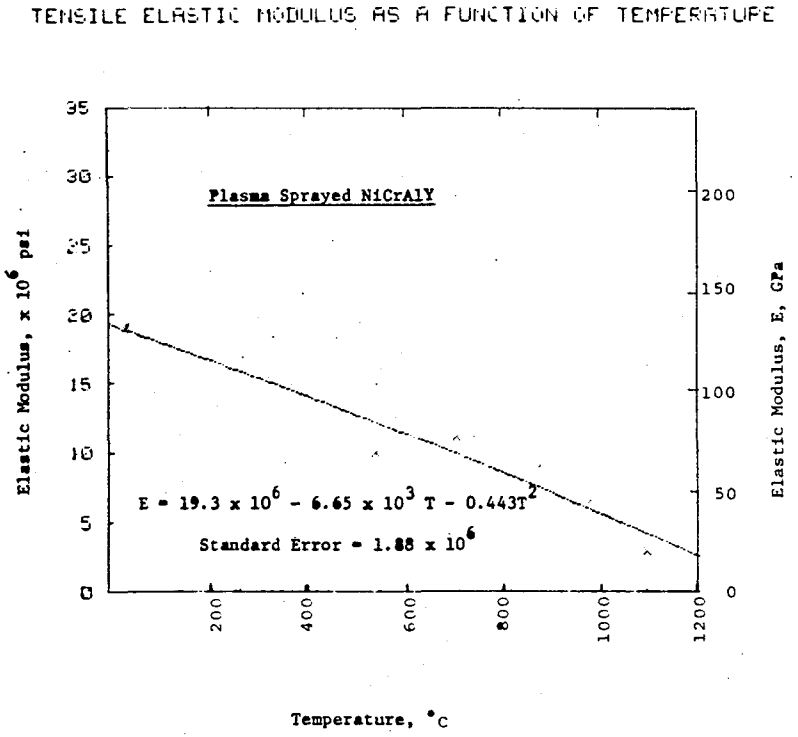

Figure 4.9 - Elastic modulus measured in tension of plasma sprayed NiCrAlY coating as a function of temperature

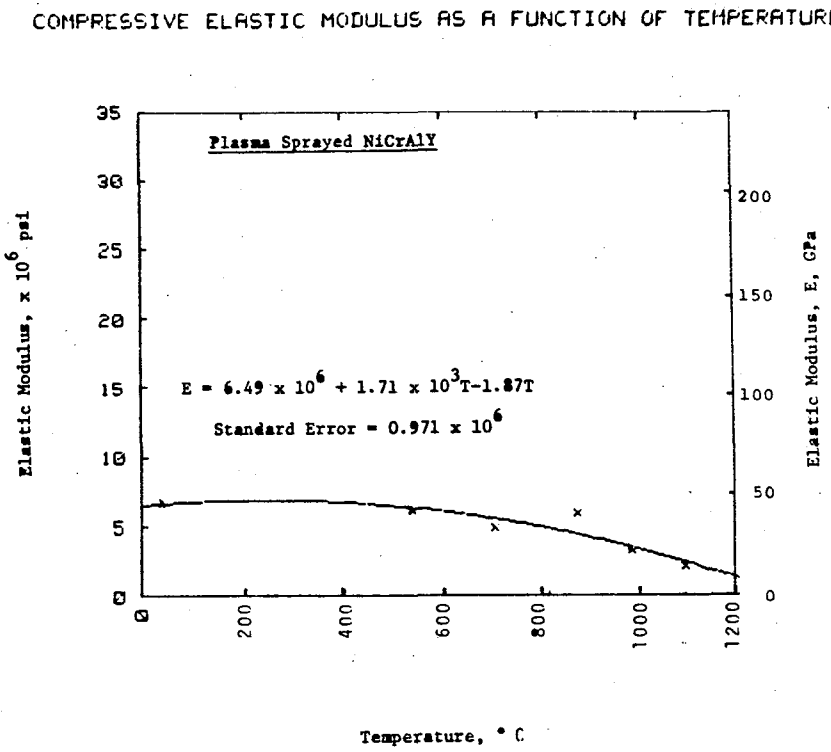

Figure 4.10 - Elastic modulus measured in compression of plasma sprayed NiCrAlY as a function of temperature

TENSILE ELASTIC MODULUS AS A FUNCTION OF TEMPERATURE

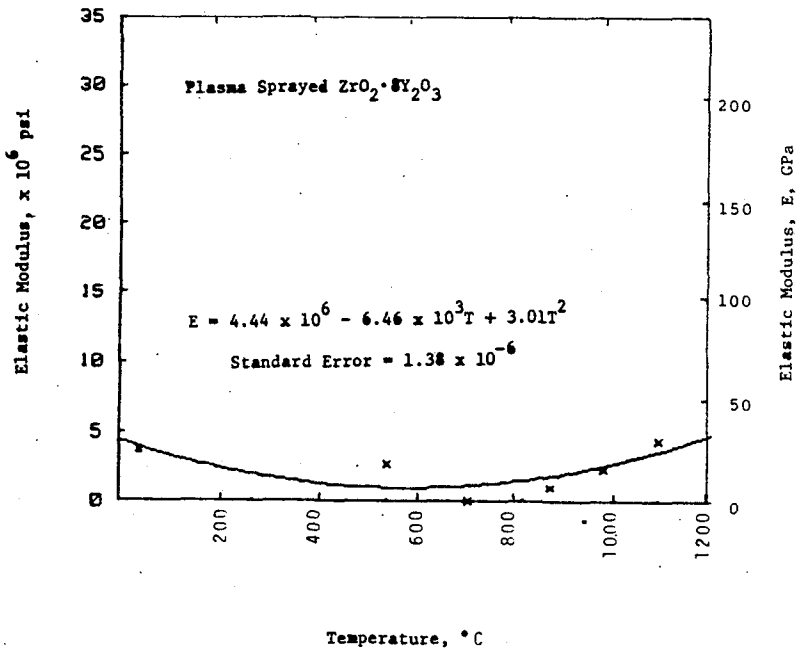

Figure 4.11 - Elastic modulus measured in tension of plasma sprayed $ZrO_2 \cdot 8Y_2O_3$ coating as a function of temperature

COMPRESSIVE ELASTIC MODULUS AS A FUNCTION OF TEMPERATURE

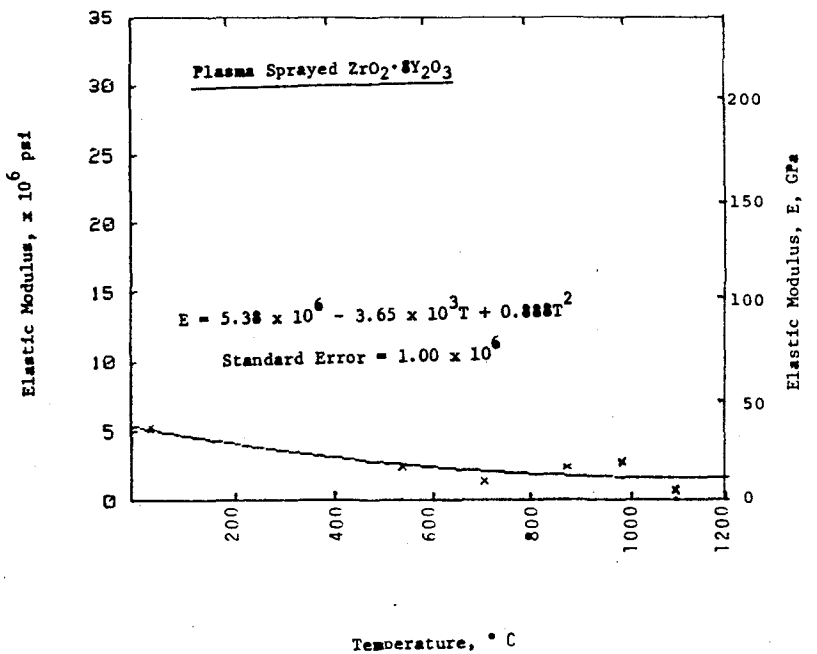

Figure 4.12 - Elastic modulus measured in compression of plasma sprayed $ZrO_2 \cdot 8Y_2O_3$ as a function of temperature

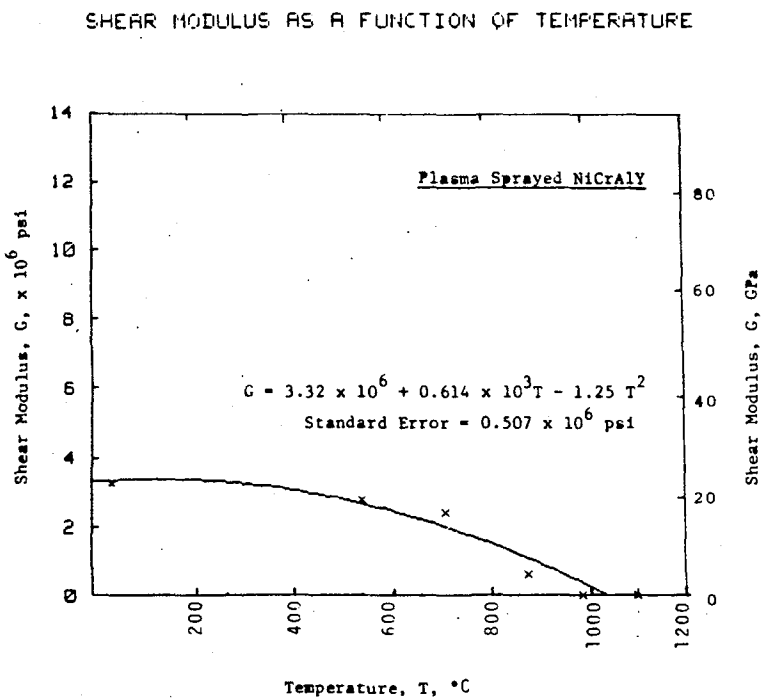

Figure 4.13 - Shear modulus measured in torsion of plasma sprayed NiCrAlY as a function of temperature

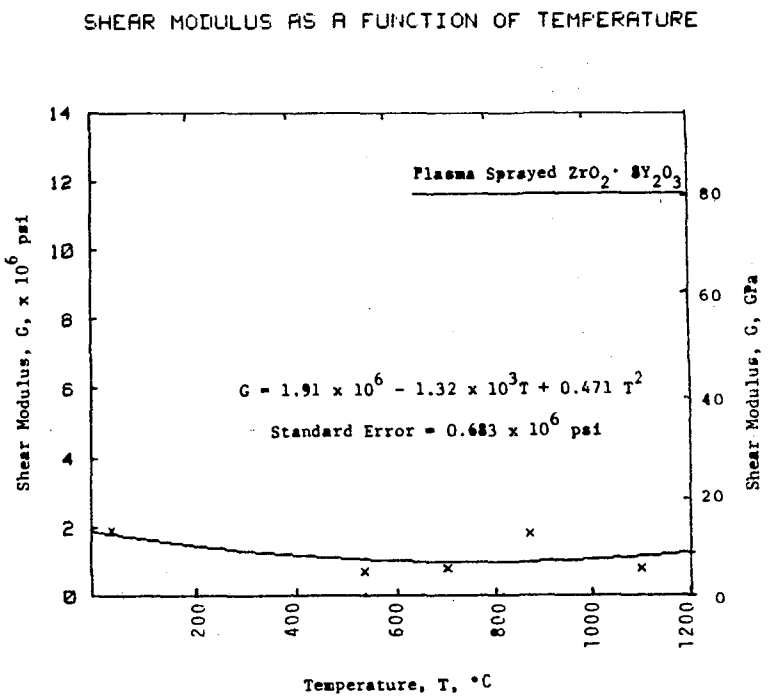

Figure 4.14 - Shear modulus measured in torsion of plasma sprayed zirconia as a function of temperature

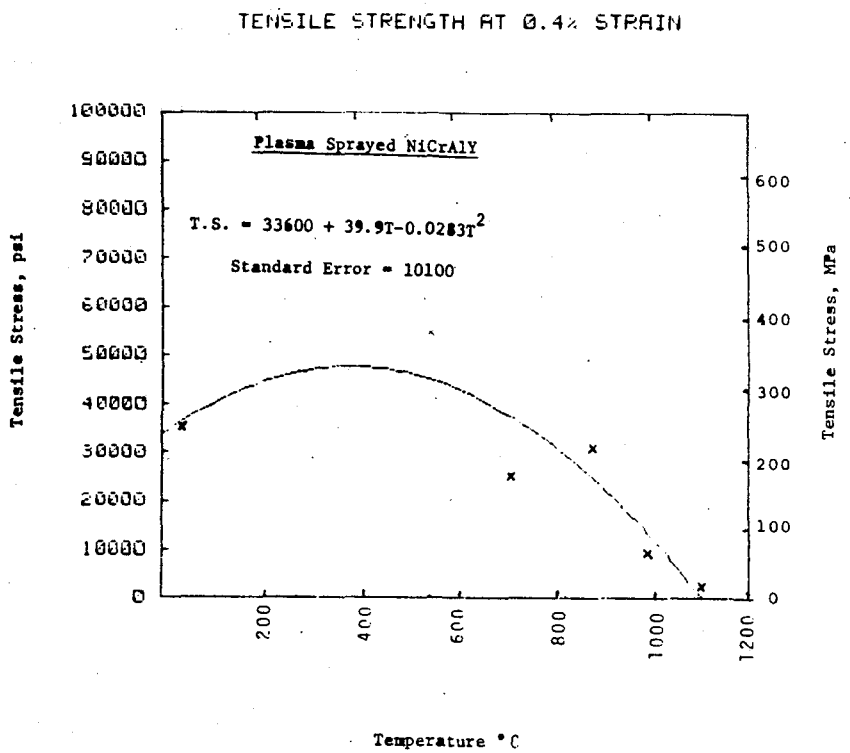

Figure 4.15 - Tensile stress bearing capacity of plasma sprayed NiCrAlY at 0.4% strain as a function of temperature

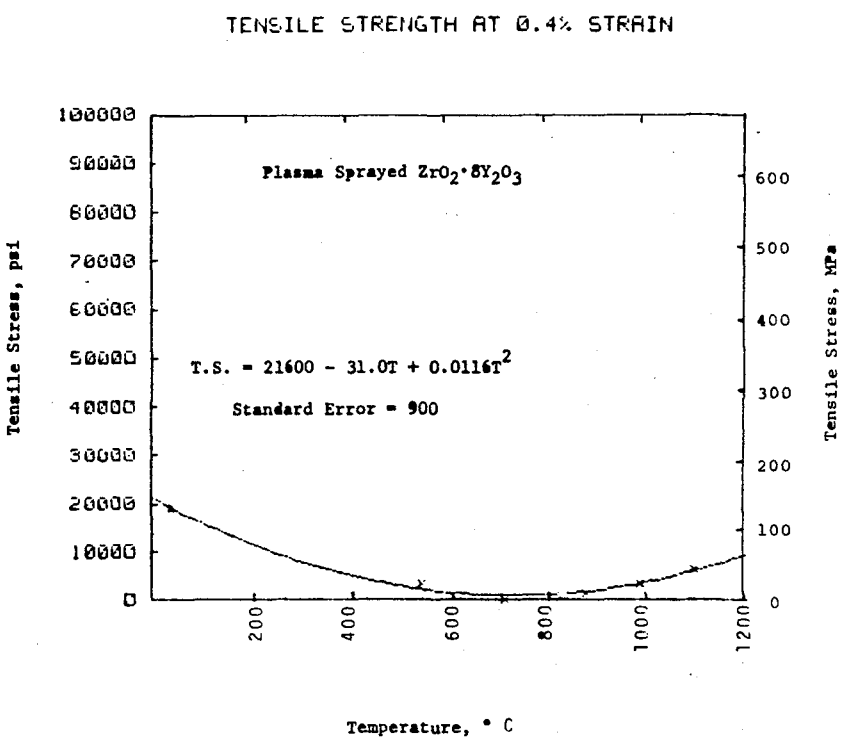

Figure 4.16 - Tensile stress bearing capacity of plasma sprayed $ZrO_2 \cdot 8Y_2O_3$ at 0.4% strain as a function of temperature

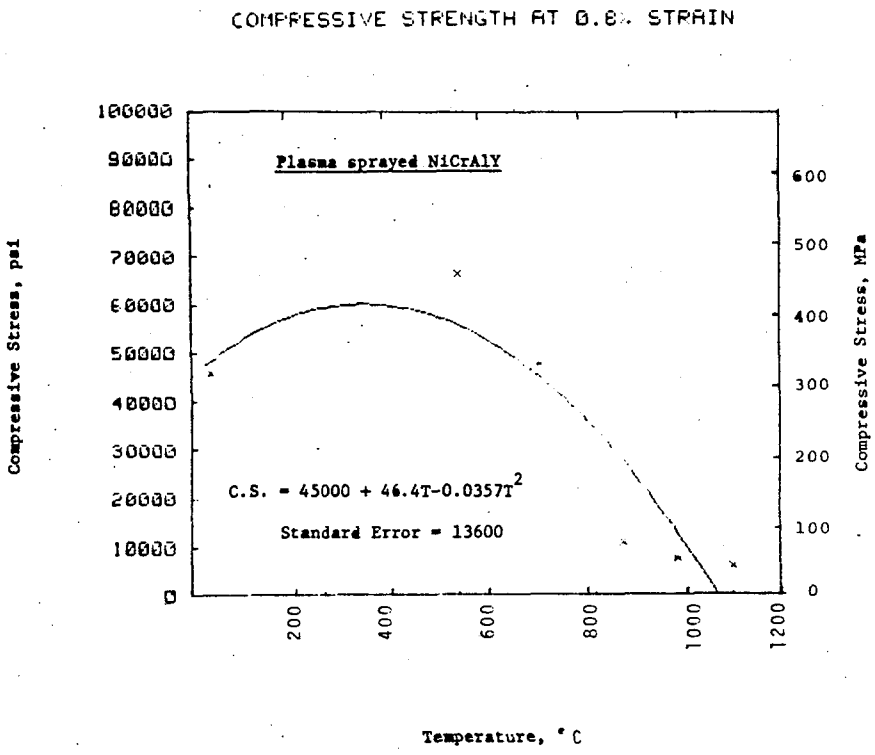

Figure 4.17 - Compressive stress bearing capacity of plasma sprayed NiCrAlY at 0.8% strain as a function of temperature

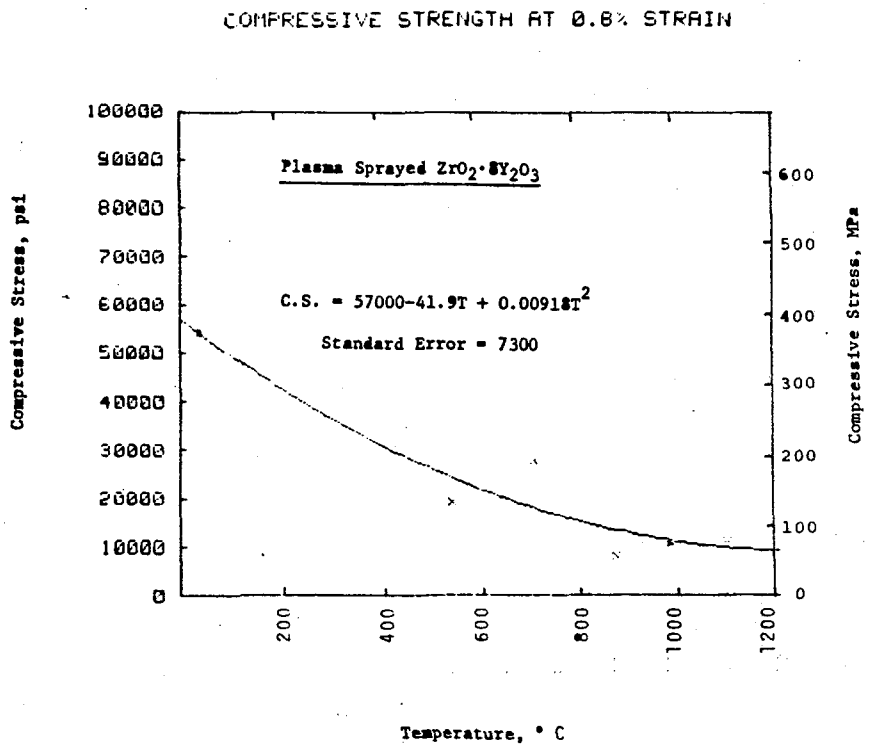

Figure 4.18 - Compressive stress bearing capacity of plasma sprayed $ZrO_2 \cdot 8Y_2O_3$ at 0.8% strain as a function of temperature

Tensile stress and strain values for both the plasma sprayed zirconia and NiCrAlY on the substrate are well above those which would be determined if the two had been tested apart from the substrate. The reason for this is that crack propagation of the weakest link of a monolyth of coating material in tension would constitute a failure and an end to the test. In the case of a coating on a stronger, more ductile substrate loaded in tension, fracture of the weakest link perpendicular to the bond plane causes the coating stress to be transferred through the substrate at the crack location. Since this is a very short distance, the coating can maintain much of its load bearing capacity. In fact, the coatings can withstand multiple cracking and still contribute to load bearing. The multiple cracking also allows the coating to be strained orders of magnitude beyond the monolyth of the same material.

4.3.6 Transverse Coating Tensile Strengths

Transverse coating strengths as functions of temperature are plotted in Figure 4.19. The line through the points was determined by polynominal regression analysis. The equation for the curve and the standard error are also given.

Although data was not obtained in the temperature region between 530 and 810K (500 and 1000°F), a strength maximum of about 17.4 MPa (2500 psi) is predicted to occur in that range. This maximum can be justified on the basis that during plasma spraying the substrate alloy is heated into that temperature range. Due to thermal expansion differences between the coating and the alloy, cooling the sprayed piece to room temperature causes residual stresses to arise. The room temperature residual stresses in turn lower the magnitude of applied stress required to cause fracture. On reheating, the stresses are initially reduced as the spraying temperature is approached, and then the stresses are reversed as the spraying temperature is exceeded. The strength reductions at temperatures above the spraying temperature might also be expected. Elevated temperature material strength degradation would also contribute

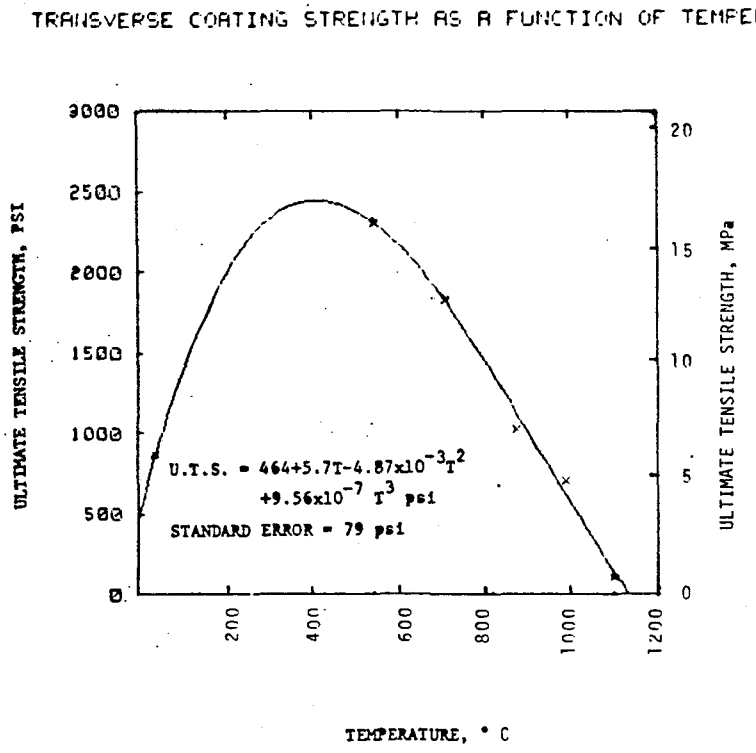

Figure 4.19 - Transverse coating strength of plasma sprayed $ZrO_2 \cdot 8Y_2O_3$/NiCr as a function of temperature

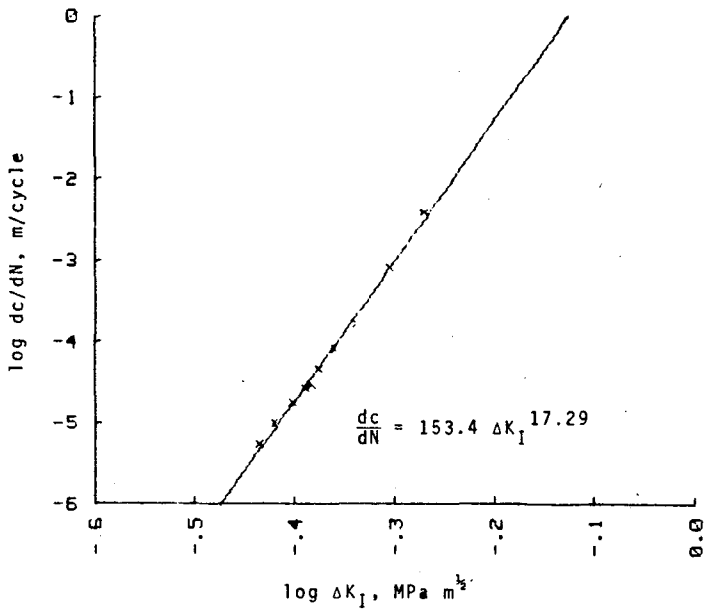

4.20 - Cyclic crack growth rate as a function of change in critical stress intensity factor.

to the overall strength loss at the higher temperatures, especially for the metallic components.

Fracture for all cases but the 2000°F test occurred near the interface between the bond coat and the ceramic. The fracture surfaces showed a mixture of ceramic and metallic particles. The surfaces of the 2000°F test specimen were severely oxidized and the fracture mode was indeterminable.

4.3.7 Fracture Toughness

The value of the Critical Strain Energy Release Rate, G_{I_c}, at room temperature was determined to be 17.1 Pa m with an estimated standard deviation of 2.3 Pa m. Using the elastic modulus measured in tension of 25.7 GPa and Poisson's ratio of 0.24 the value of the Critical Stress Intensity, K_{I_c} was calculated to be 0.683 MPa $m^{1/2}$ with a estimated standard deviation of 0.048 MPa $m^{1/2}$.

4.3.8 Cyclic Crack Growth Rates

Measured crack growth rates are shown to be linear on a log dc/dN versus log ΔK_I plot in Figure 4.20 where c is the crack length, N is the number of cycles and ΔK_I is the change in stress intensity on each cycle. The data thus fits the well known power law

$$dc/dN = B\ \Delta K_I^{\ n}$$

5.0 DESIGN ANALYSIS

The subject of part of this investigation was the cooled first stage rotor blade of the Westinghouse W501D, 92MW, combustion turbine. The study entailed finite element transient and steady state heat conduction and elastic stress analyses of both the uncoated (for reference) and two thermal barrier coating configurations. A total of 13 cases were run. The remaining part of this investigation concerned the overall aerodynamic and thermodynamic performance of the engine.

In this section, the finite element analysis and its results will be discussed. Highlights of the detailed design analyses will be summarized in three categories which correspond to the objectives of this task:

- Effects of coatings on base metal life
- Effects of turbine operation on coating stresses
- Effects of coatings on engine performance

5.1 Finite Element Analysis

The matrix of analysis conditions studied is given in Table 5.1. These represent a wide spectrum of operating conditions and several coating conditions which allowed the effects of thermal barrier coatings to be fully assessed for a particular component in an industrial turbine. The model used, the inputs into the model and some of the results are discussed.

5.1.1 Finite Element Model

The model used to assess the mid-height cross-section of the W501D first stage rotor blade is shown in Figure 5.1. It consists of 896 two dimensional, eight node, isoparametric elements. The coated model is an

TABLE 5.1

ANALYSIS MATRIX

Configuration	Steady State	Normal Startup Transient	Normal Shutdown Transient	Full Load Tripout Transient	Hot Start Transient
Uncoated	X	X	X	X	X
0.38 mm $Y_2O_3 \cdot ZrO_2$ TBC with 5 mil NiCrAlY bond coat	X	X	X	X	X
0.19 mm $Y_2O_3 \cdot ZrO_2$ TBC with 7.5 mil NiCrAlY bond coat	X	X		X	

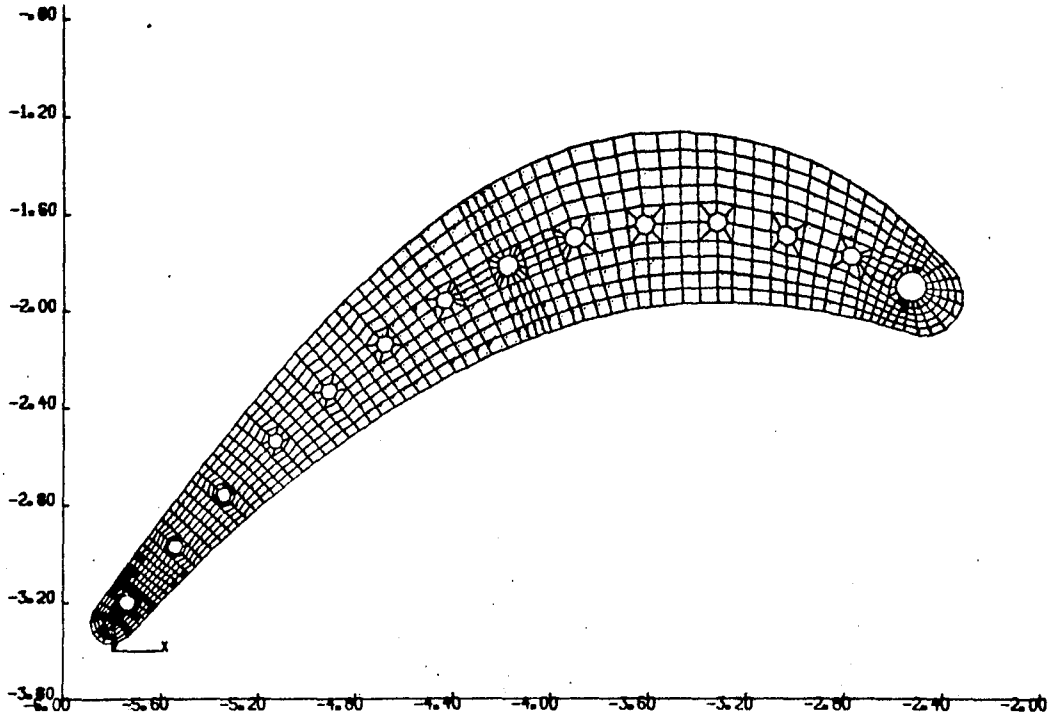

Figure 5.1 - Finite element model of W501D 1st stage rotor blade, mean height, airfoil section, uncoated

extension of the uncoated one. Three 162 element layers were added to the periphery of the previous model making the total number 1382. The first layer was 0.13 mm thick followed by two 0.19 mm thick layers. A blow up plot of the coated leading edge, and the trailing edge are shown in Figures 5.2 and 5.3.

Two coating thickness cases were studied. In the first case, the 5 mil layer was given the properties of a NiCrAlY bond coating and the two 7.5 mil layers the properties of $ZrO_2 \cdot Y_2O_3$. In other words, the first case is a 15 mil ceramic coating on a 5 mil bond coat. In the second case the 5 mil layer was given the properties of the blade base metal, thereby eliminating it as a coating. The first 0.19 mm layer was then given the properties of the NiCrAlY bond and the second 0.19 mm layer the properties of the ceramic. Thus, case two was essentially equivalent to reducing the ceramic thickness in case one by one half.

5.1.2 Inputs

The inputs into the model included the thermal loads, the mechanical loads and the material properties.

5.1.2.1 Thermal Boundary Conditions. The bases for the thermal load inputs are the hot gas and coolant temperatures during the turbine run and the heat transfer to the component. Figure 5.4 shows the blade hot gas temperature versus time after start up and relates the temperature versus time profile to the W501D starting sequence from initiation through cranking to reaching base load operation in about 29 minutes. Figure 5.5 provides the internal coolant hole temperatures during start up.

Figure 5.6 describes corresponding transient start up heat transfer coefficient versus time relationship for the external surface and the coolant hole surface versus time. In this case, the coefficient is presented as a ratio factor h/h_{baseload} where h_{baseload} is as presented in Figure 5.7.

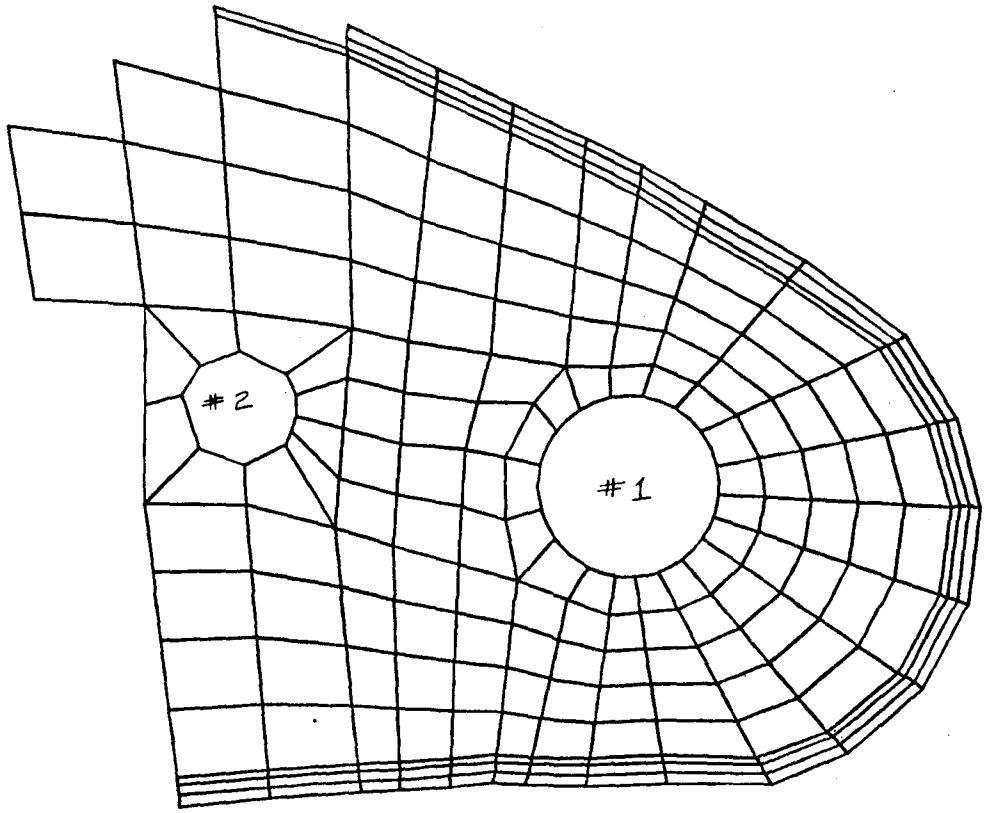

Figure 5.2 - Leading edge region, TBC blade model

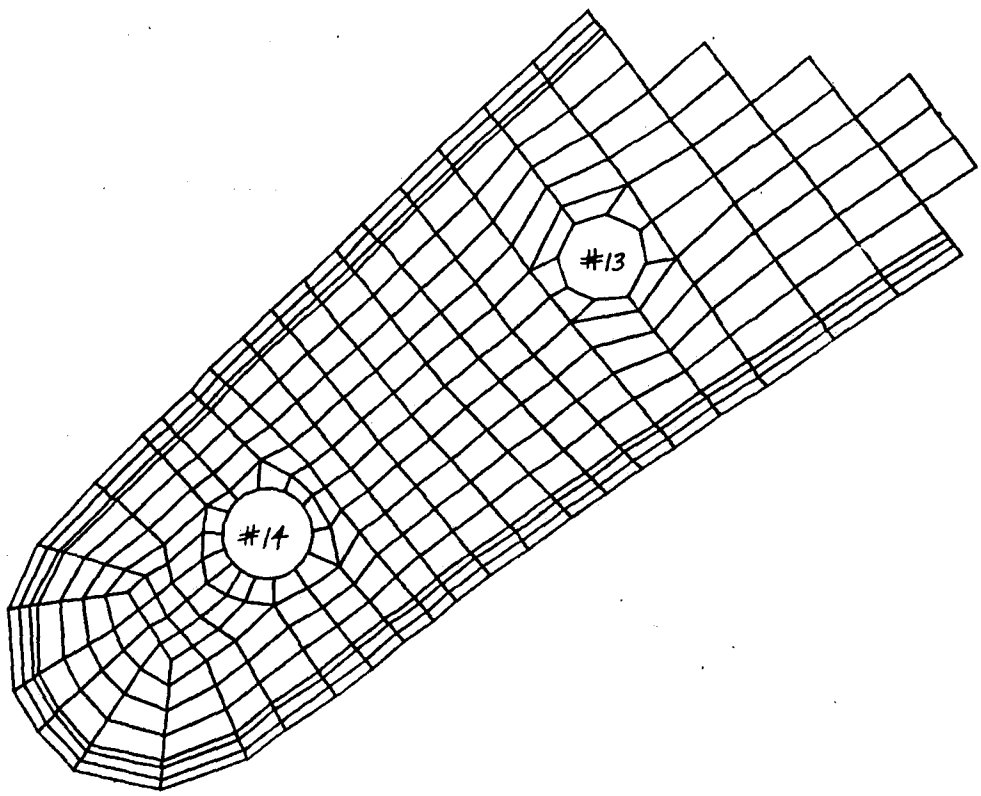

Figure 5.3 - Trailing edge region, TBC model

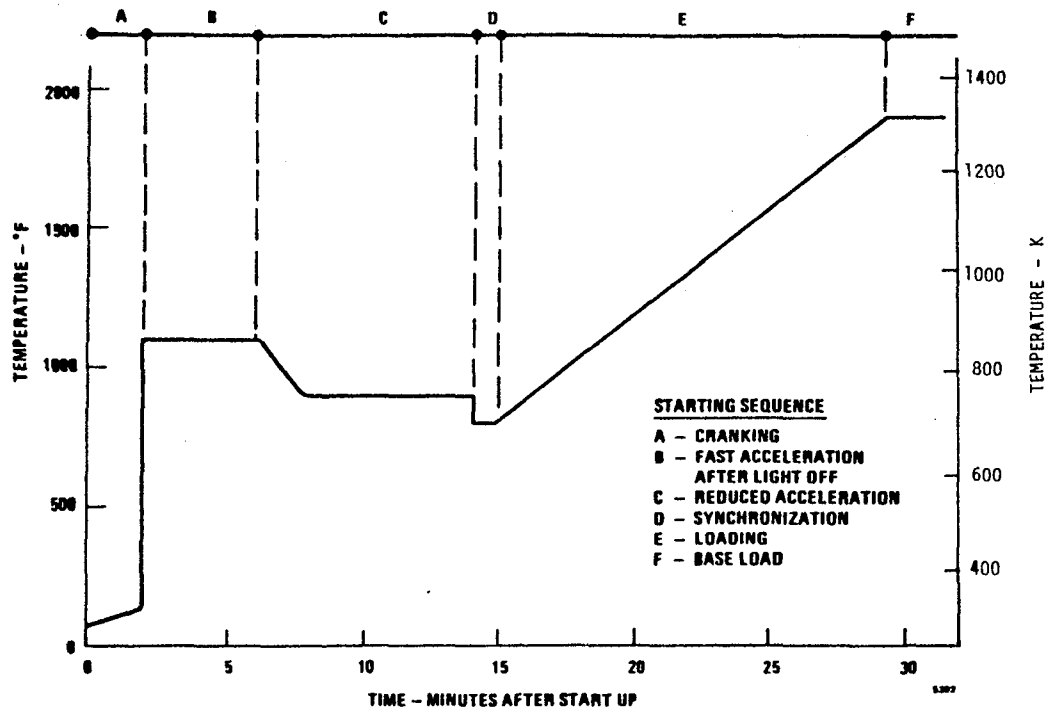

Figure 5.4 - W501D Row 1 blade hot gas temperature during startup

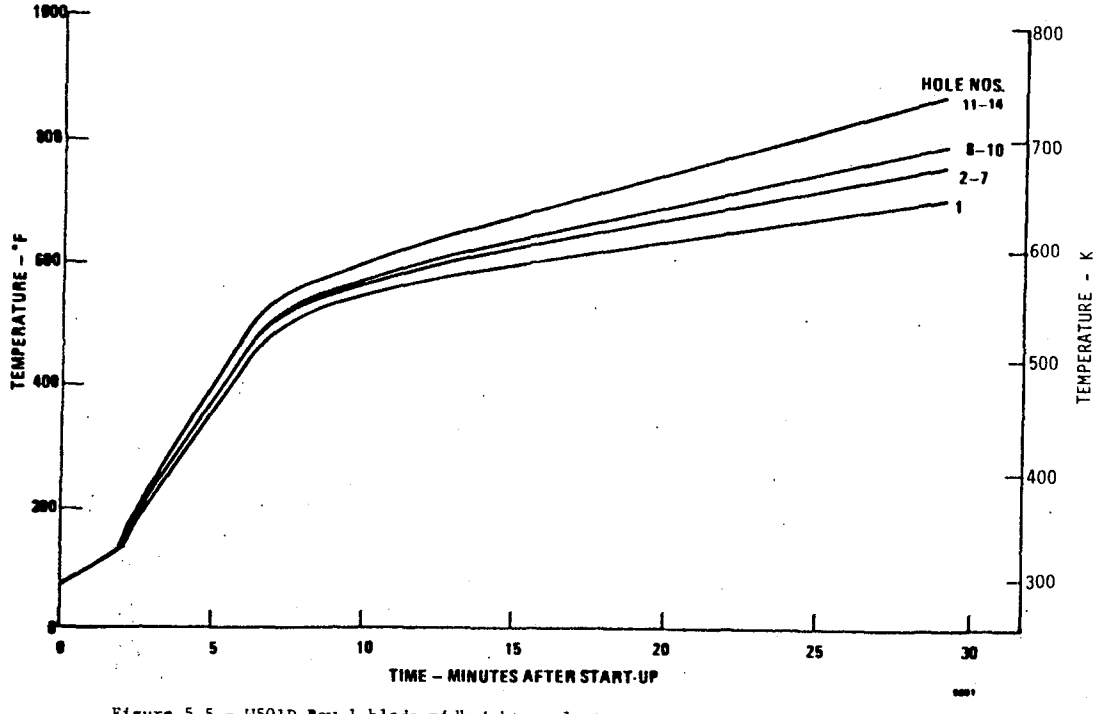

Figure 5.5 - W501D Row 1 blade midheight coolant temperature during startup

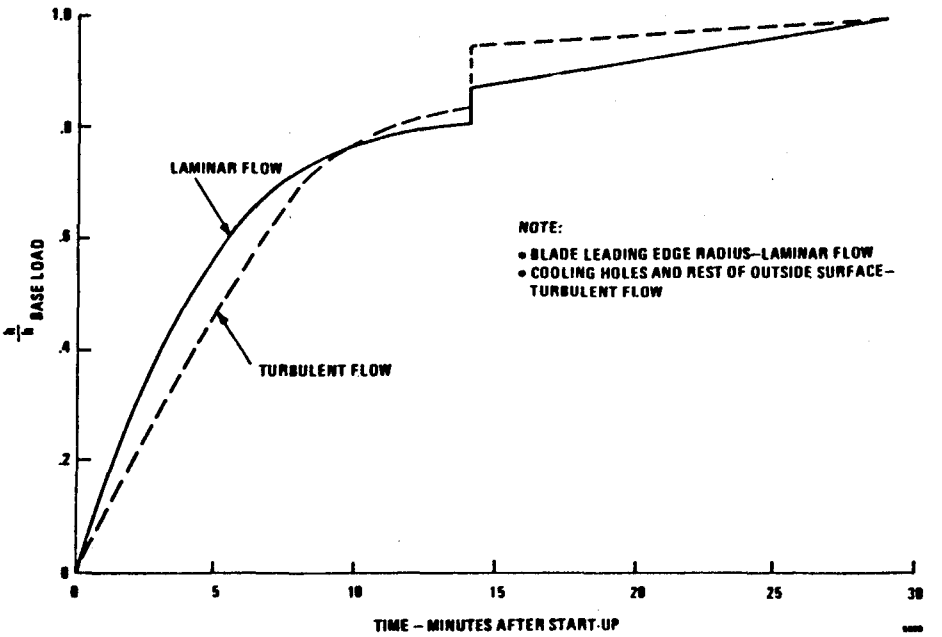

Figure 5.6 - W501D Row 1 blade heat transfer during startup

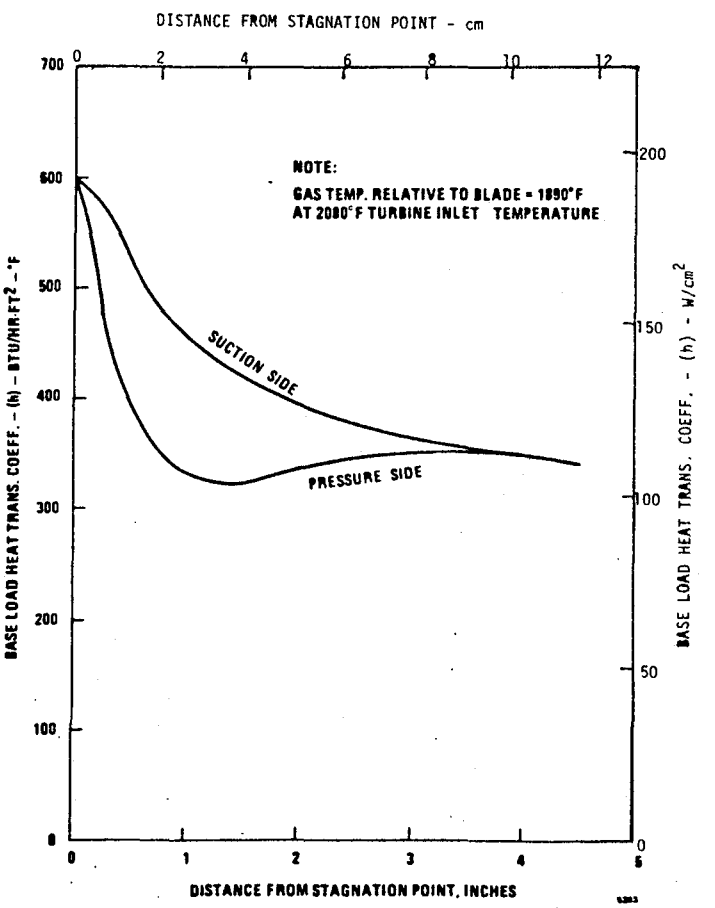

Figure 5.7 - W501D Row 1 blade baseload steady state heat transfer coefficients--mean section

Figures 5.8 and 5.9 depict the blade gas path and coolant flow shut down temperatures versus time and related heat transfer ratio versus time after trip out from idle conditions, respectively.

5.1.2.2 Stress Boundary Conditions (Loadings). The stress boundary conditions, are of course, mainly the temperature distributions obtained from the heat conduction runs. The external loads are the centrifugal load of the top half of the blade and the gas bending moments. Because the gas bending stresses are small, they were neglected in the calculations. The centrifugal force at full speed (3600 RPM) is 76,060 N for the uncoated blade and 82,290 N for the 0.38 mm TBC blade. This results in base metal average stresses of 61 and 66 MPa. External loads for the transient runs were calculated by multiplying full load values by the square of the ratio of speed at a given time to 3600.

5.1.2.3 Material Properties. The U710 base metal properties were generated in Westinghouse laboratories and were taken from the Westinghouse Combustion Turbine materials manual. The NiCrAlY bond and $ZrO_2 \cdot Y_2O_3$ TBC material properties were taken from NASA CR-135359 [ref. 15].

5.1.3 Results of Finite Element Analyses

Finite element analyses were performed on uncoated blades and blades with 0.19 and 0.38 mm of ceramic coating. Typical steady state metal temperature and stress contours for the uncoated blade are shown in Figures 5.10 and 5.11. Similar contours for the base metal of the 0.38 mm TBC blade are shown in Figures 5.12 and 5.13. The contours given are for the substrate metal part of the blade only. The temperature and stress distributions in the coatings will be presented later.

At steady state, temperature minima, tensile stress maxima and shear maxima were shown to occur at the surface of the No. 5 cooling hole. The compressive stress maxima occur at the outer surfaces of the blade. Coating with 0.38 mm of ceramic reduces the maximum tensile

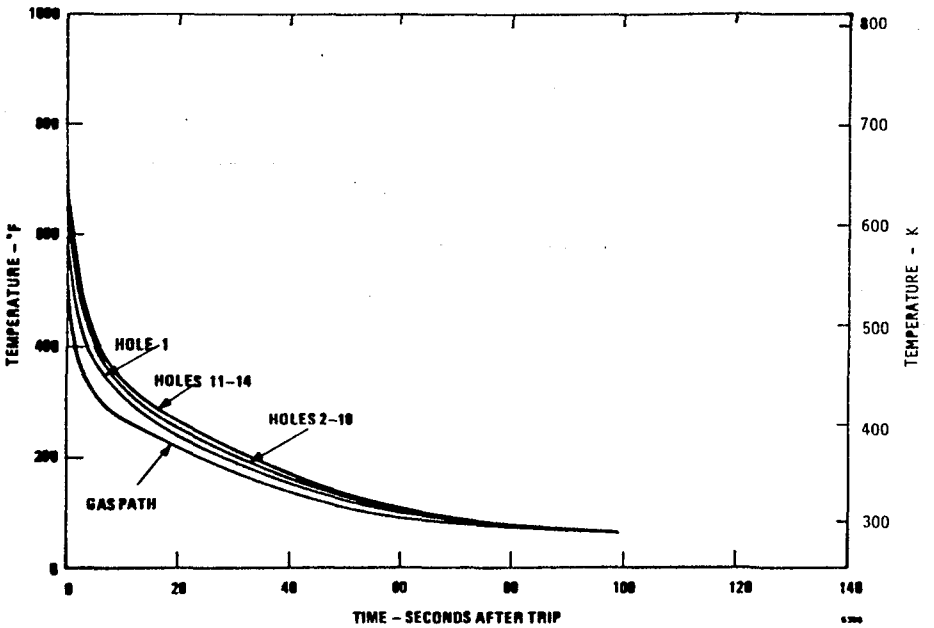

Figure 5.8 - W501D Row 1 blade environment temperature following tripout

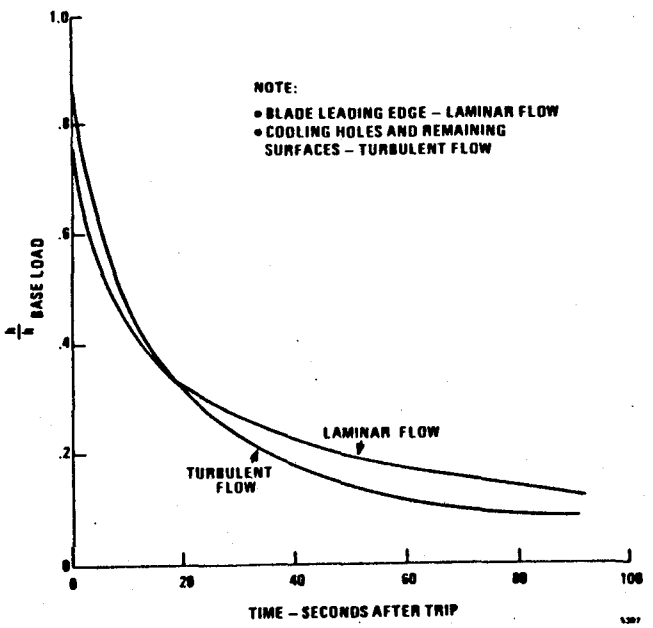

Figure 5.9 - W501D Row 1 blade heat transfer following tripout

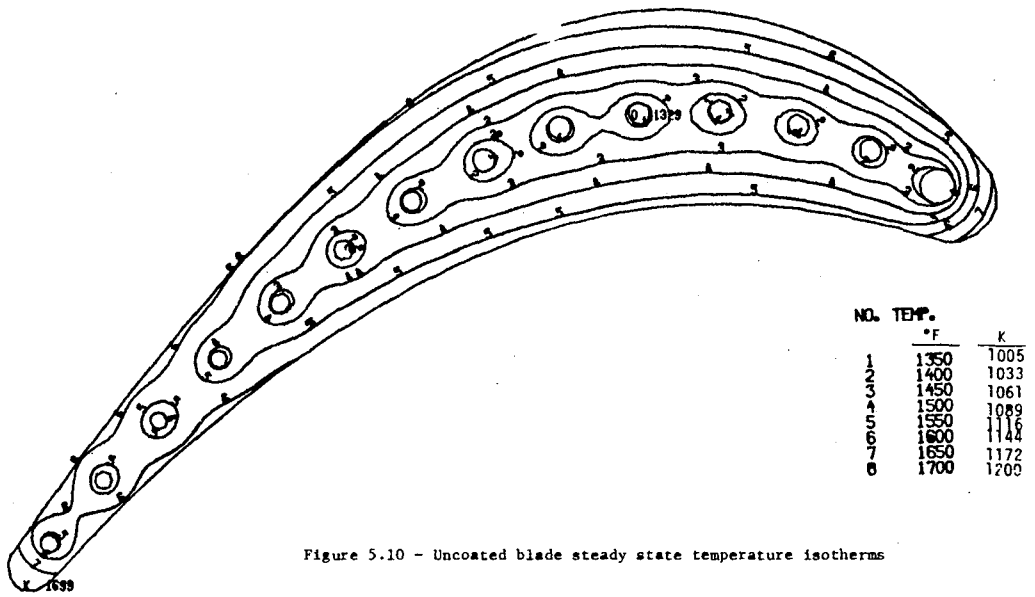

Figure 5.10 - Uncoated blade steady state temperature isotherms

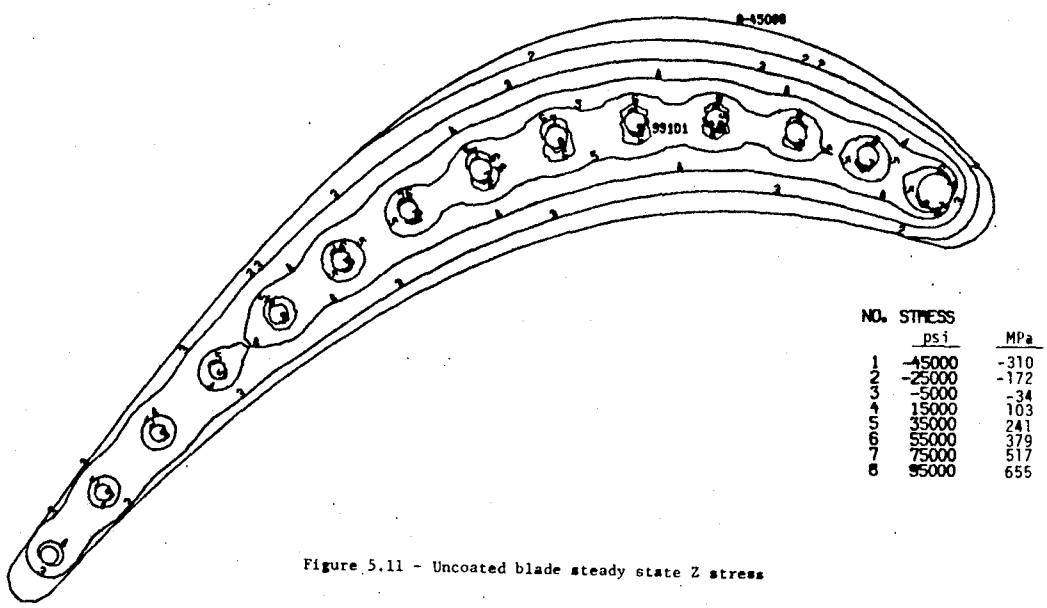

Figure 5.11 - Uncoated blade steady state Z stress

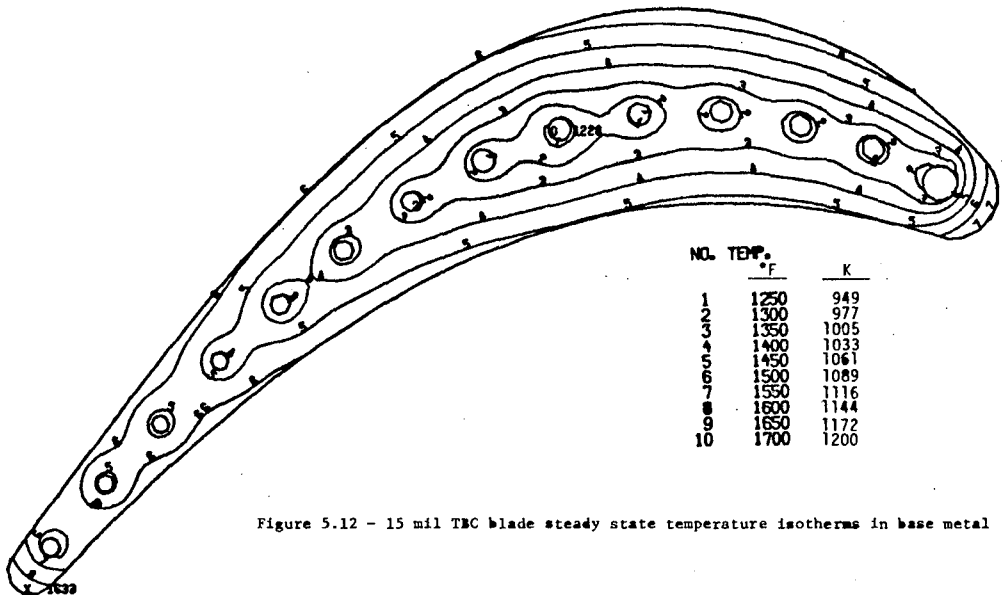

Figure 5.12 - 15 mil TBC blade steady state temperature isotherms in base metal

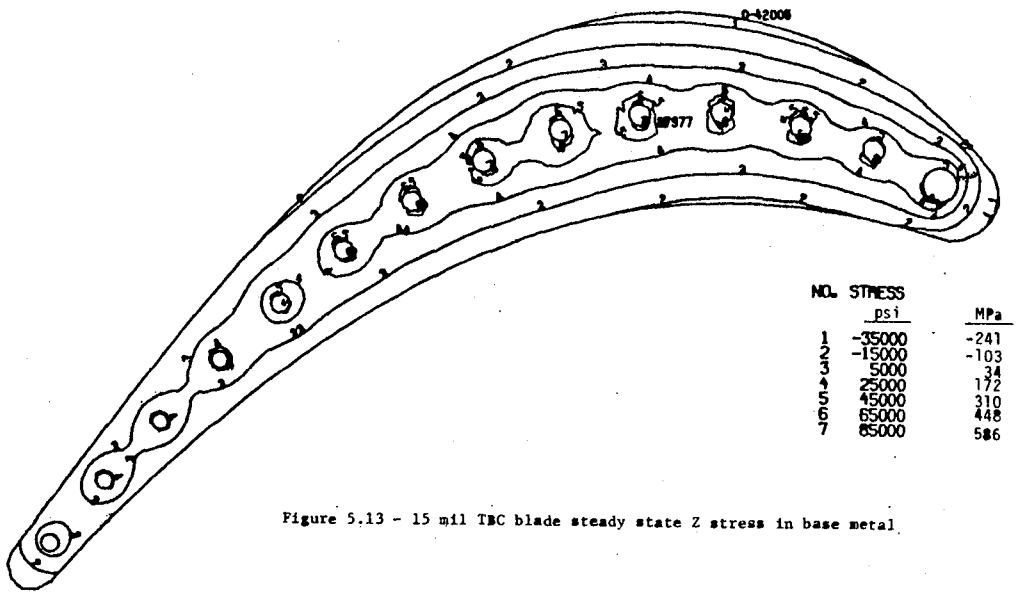

Figure 5.13 - 15 mil TBC blade steady state Z stress in base metal

stresses by about 12 percent and the maximum compressive stresses by up to 19 percent.

The finite element analyses have also been carried out for the uncoated, 0.19 and 0.38 mm TBC coated blades for a full range of normal start up and shut down procedures, as well as for the severe conditions of hot start up and full load dump. Instead of presenting the data as stress contours, the data have been summarized for the five positions shown in Figure 5.14. These in turn have been plotted as functions of time within a turbine run cycle. Typical temperature and stress responses of the blade are plotted in Figures 5.15 through 5.18. Figures 5.15 and 5.16 show the thermal response to a normal start, normal shutdown, hot start, and full load tripout for selected regions (Figure 5.14) on the blade, i.e., leading edge, trailing edge, suction side, pressure side, and edge of hole number five (counting from the leading edge). Plotted in Figures 5.17 and 5.18 are the z-stresses[(a)] caused by these transients for the same points on the blade. In each of the figures, both the uncoated and 0.38 mm TBC coated blade results are presented.

As would be expected, the exterior metal surfaces operate in compression during start-ups and at steady state, while the interior surfaces operate in tension. These stress states reverse themselves during the shutdown procedures. Figures 5.15 through 5.18 have two sets of lines that allow the comparison between the coated and uncoated versions of the blades: the uncoated version is represented by a solid line and the coated version by a dashed line. In each of the positions and at every time during the operational cycle, the effect of the coating is to moderate the stresses. That is, the magnitudes of both the tensile and compressive stresses are reduced. The largest effects occur for the full load trip out. The major contribution of this stress moderation should be in the improvement of low cycle fatigue life. Creep rupture life should also be enhanced since both the stresses and temperatures are reduced.

(a) the z-direction is the direction normal to the plane of the cross-section, i.e., perpendicular to the plane of the paper.

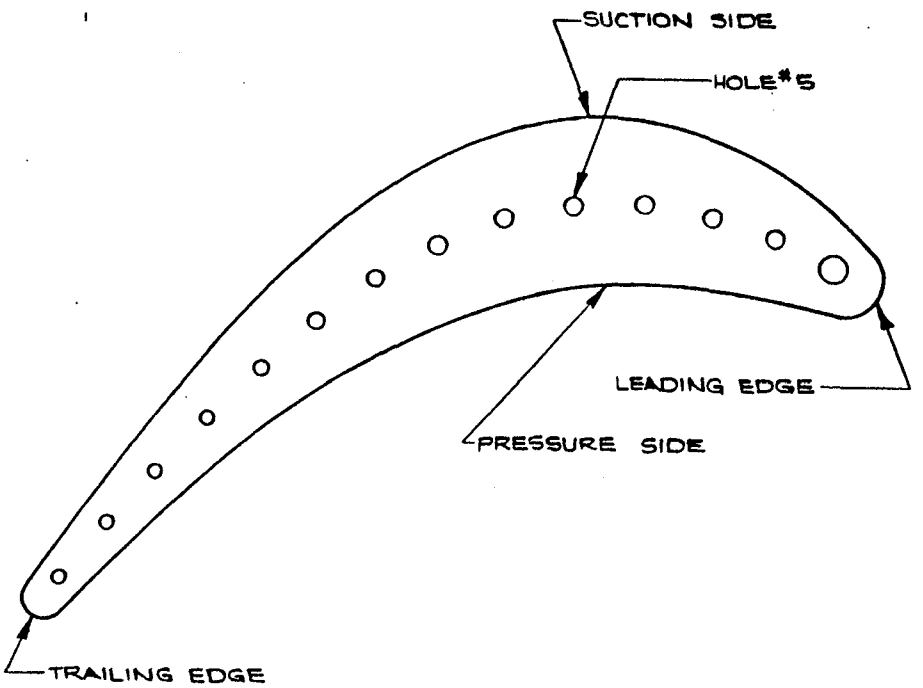

Figure 5.14 - Regions selected for plotting of transient stresses and temperatures

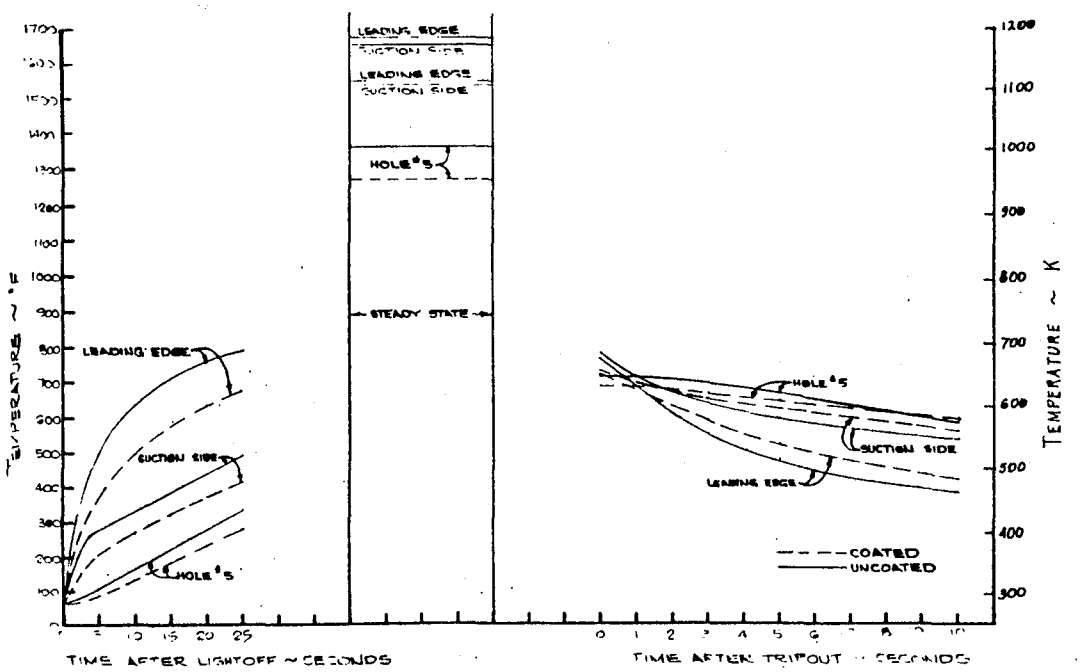

Figure 5.15 - Effect of 15 mil TBC on base metal temperature
W501D coated 1st stage roter blade mean (midsection) section
Normal startup and shutdown

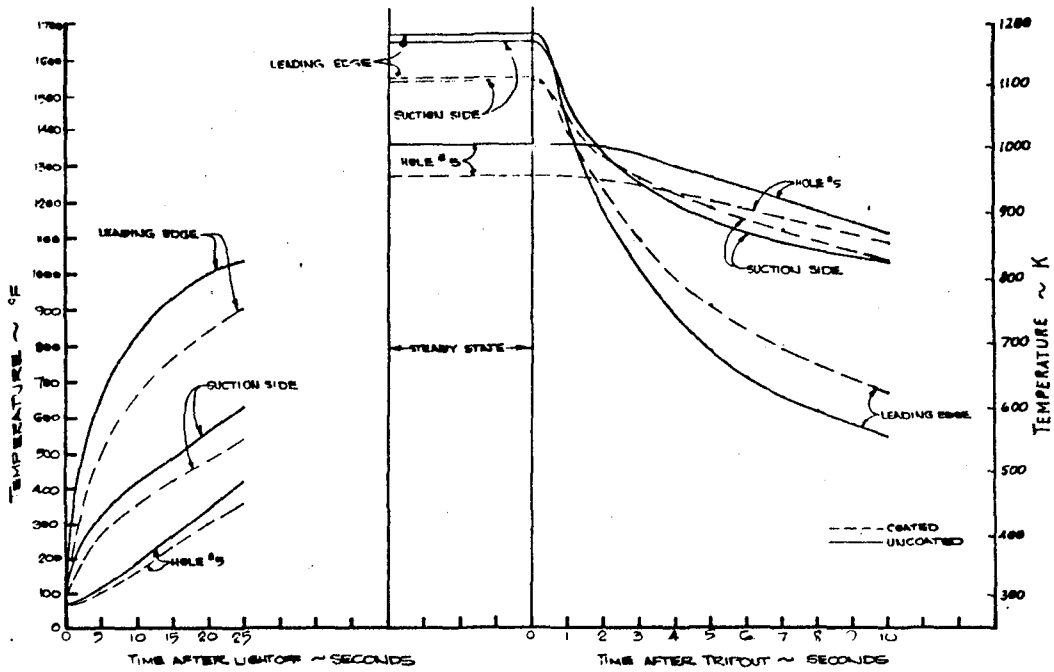

Figure 5.16 - Effect of 15 mil TBC on base metal temperature - W501D coated 1st stage rotor blade mean (midheight) section - Hot start and full load dump

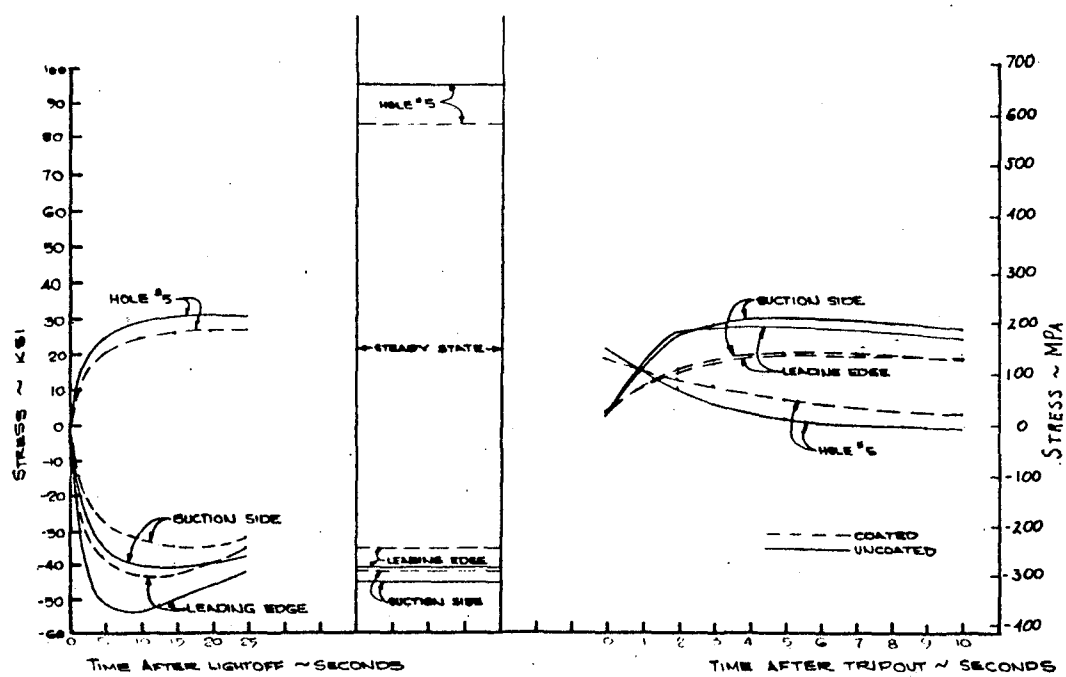

Figure 5.17 - Effect of 15 mil TBC on base metal σ_z - W501D coated 1st stage rotor blade mean (midheight) section Normal startup and shutdown

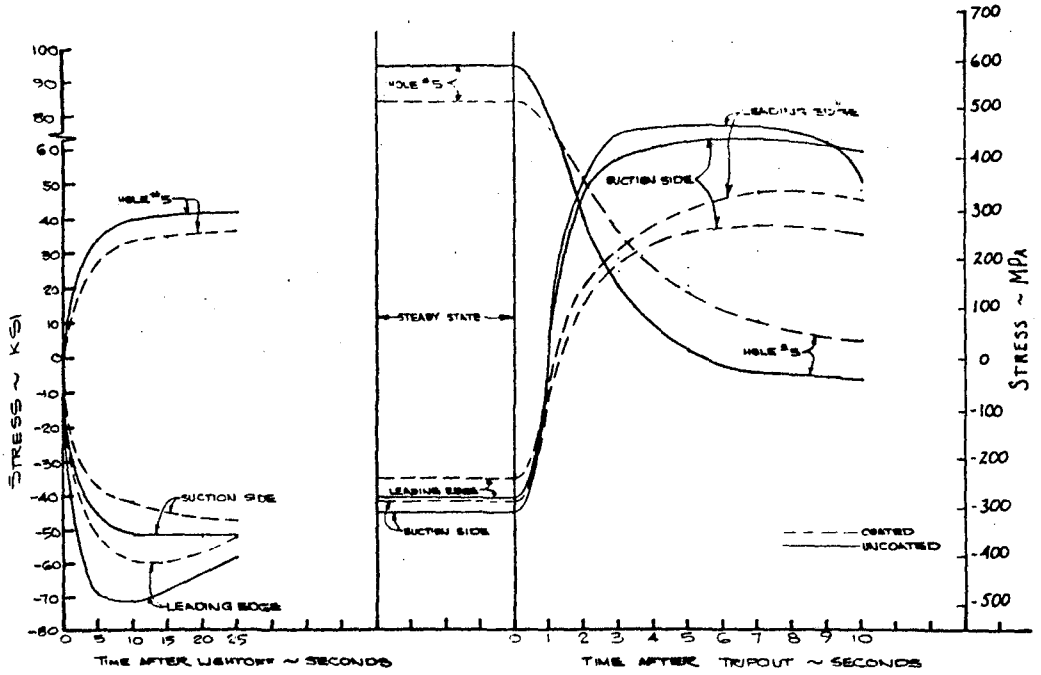

Figure 5.18 - Effect of 15 mil TBC on base metal σ_r - W501D coated 1st stage rotor blade mean (midheight) section - Hot start and full load dump

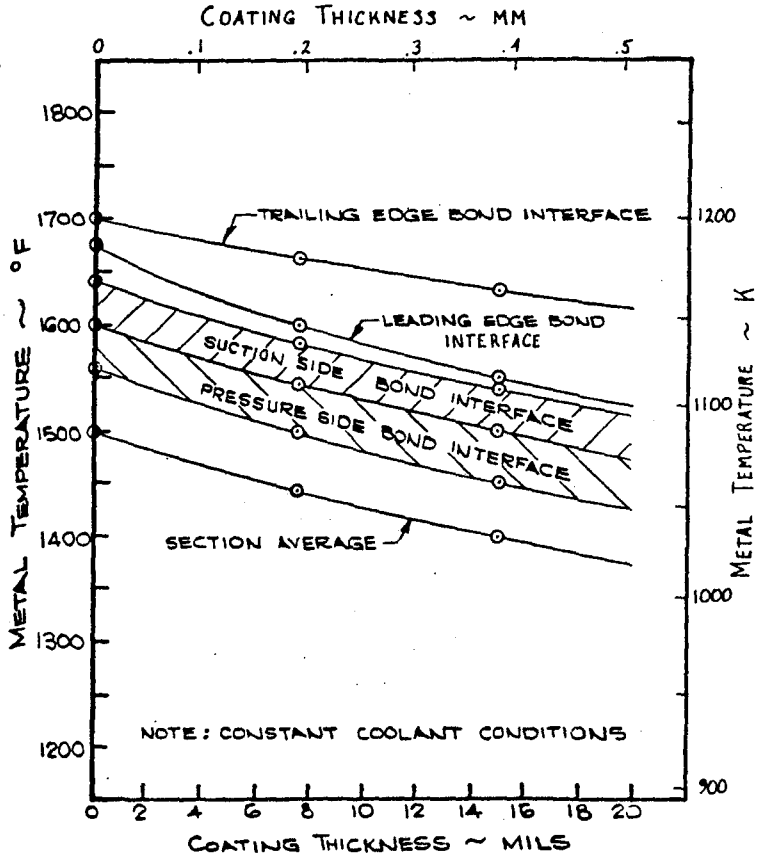

Figure 5.19 - Effect of TBC thickness on base metal temperature

5.2 Effect of Coatings on Base Metal Life

The results of the finite element analyses were assessed to estimate the effects of coatings on the creep, low cycle fatigue and corrosion lives of the blade material. The assumption made was that the cooling air flow was maintained constant and that the principal influence of the coatings was to reduce the metal temperatures[(b)]. The calculated temperature reductions at various positions on the blade and for the section average as functions of coating thickness are given in Figure 5.19. A 0.19 mm ceramic coating is shown to reduce the base metal temperature by 33K and a 0.38 mm coating by 56K.

The effect of this temperature reduction on the relative creep rupture life is shown in Figure 5.20. A four fold improvement in life-time is estimated to be achieved with a 0.19 mm coating. A 0.38 mm coating improves life ten times that expected for an uncoated blade.

Start-up and shut down cycles of turbines can lead to low cycle fatigue damage of the components. The expected fatigue lives of turbine alloys, as shown in Figure 5.21, are temperature dependent. An order of magnitude improvement is expected for the 56K temperature reduction achieved by 0.38 mm coating.

Two effects of ceramic coatings on corrosion resistance are expected. The major contribution of a coating is to prevent the deposition contaminants from contacting the metal, thus eliminating or retarding chemical reactions. This was determined in the other tasks of the program. The second contribution of an insulating coating is the corrosion reduction due to the diminishing of the metal surface temperature. Therefore, even if the contaminant reached the metal, corrosion of the alloy shown in Figure 5.22 would be reduced by nearly one half with a 0.38 mm thermal barrier coating.

(b) The alternative option of maintaining constant temperature with reduced air flow does not change base metal life.

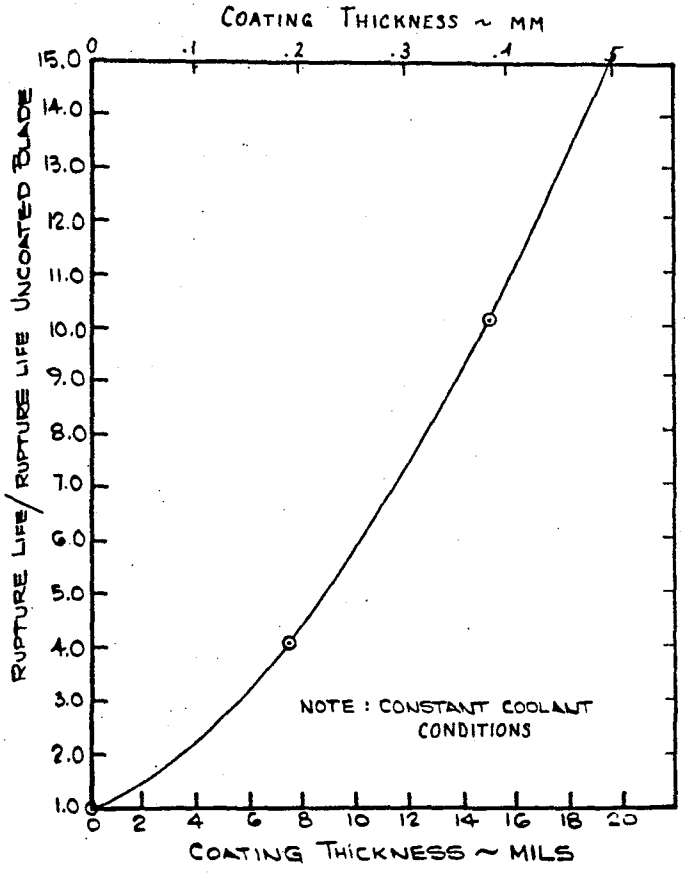

Figure 5.20 - Effect of TBC thickness on base metal rupture life

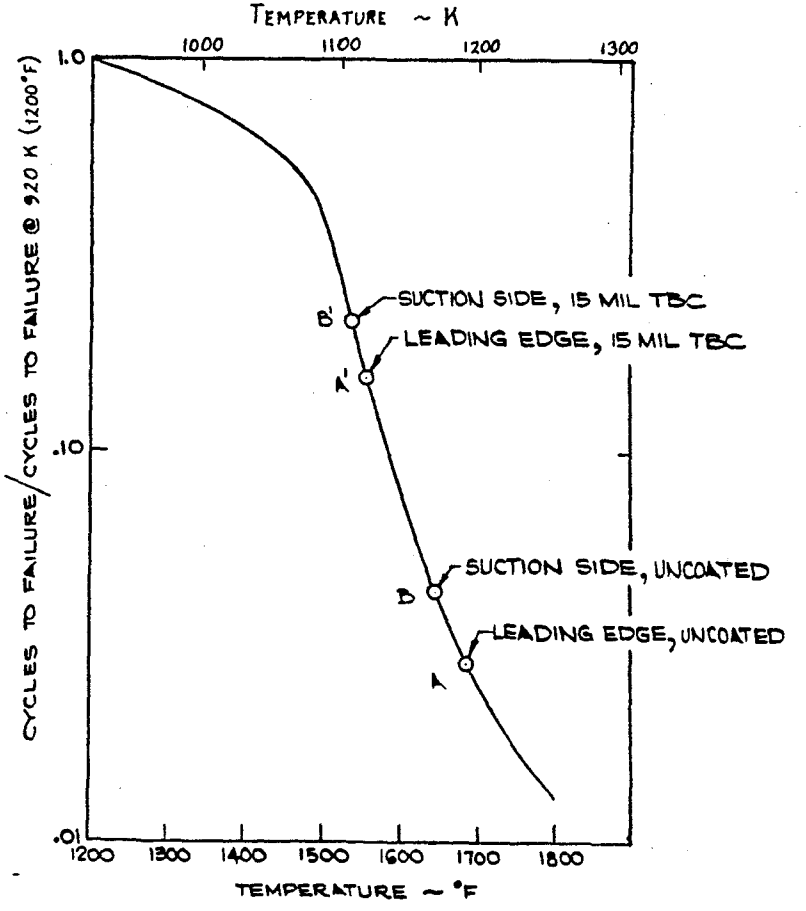

Figure 5.21. - Effect of temperature on LCF of typical nickel base alloys at low strain range and long hold times

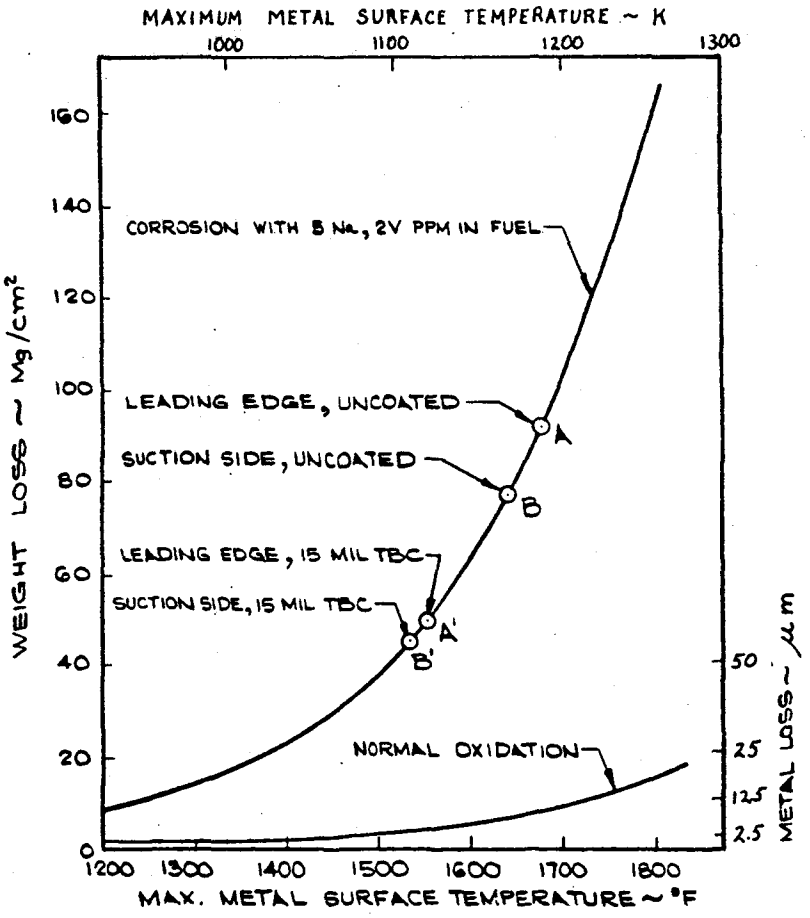

Figure 5.22 - Corrosion of U-500 alloy when burning 3-GT fuel compared to normal oxidation in 150 hrs

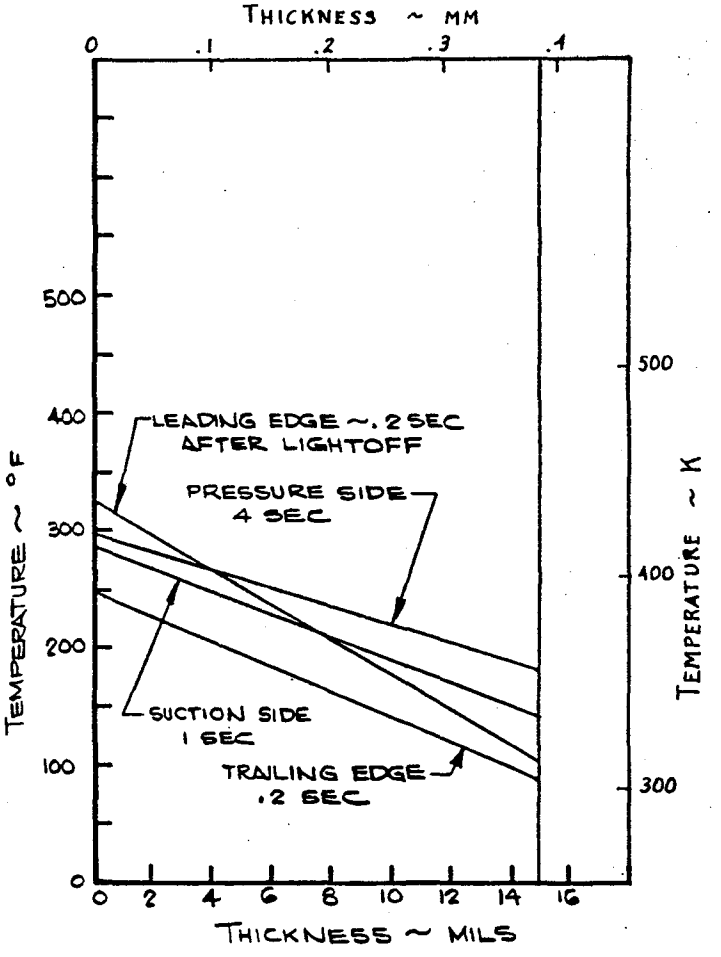

Figure 5.23 - Temperature distribution in 15 mil TBC during normal startup

5.3 Effect of Turbine Operation on Coating Stresses

Temperature gradients occurring in all stages of the turbine operation give rise to thermally induced stresses within the coatings and at the interface between the ceramic and bond coats. If these stresses are sufficiently high, they can lead to coating fracture. Fracture of porous plasma sprayed ceramic coatings does not necessarily cause coating failure. As was demonstrated in the Task IB tensile tests, multiple coating fracture in planes perpendicular to the bond interface gives these coatings a large degree of strain tolerance. That is, the cracks allow the coating to be strained well beyond values that could be achieved with similar monolythic materials. On the other hand, fracture in the plane of the bond interface cannot be tolerated, since this leads to loss of coating adherence. These two types of coating fractures were analytically assessed in this task.

Typical temperature profiles for start-up, steady state and shut down operating conditions are shown in Figures 5.23, 5.24 and 5.25. In these plots and the subsequent stress plots, four positions around the periphery of the mid height airfoil cross section are represented. The times on the start-up and shut down plots represent those when the maximum gradient occurred at each position. Maximum heat transfer occurs at the leading edge and the trailing edge has the thinnest section. Therefore, these two reach their temperature maxima before either side of the blade.

The stresses within the coatings as functions of coating thicknesses which result from these thermal gradients are given in Figures 5.26, 5.27 and 5.28. The t direction refers to the tangent to the bond interface within the plane of the airfoil cross-section. The z direction refers to the direction parallel to the bond interface, and perpendicular to the plane of the airfoil cross section. The n direction is normal to the bond interface within the cross sectional plane.

The coatings are shown to be stressed in tension in both the z and

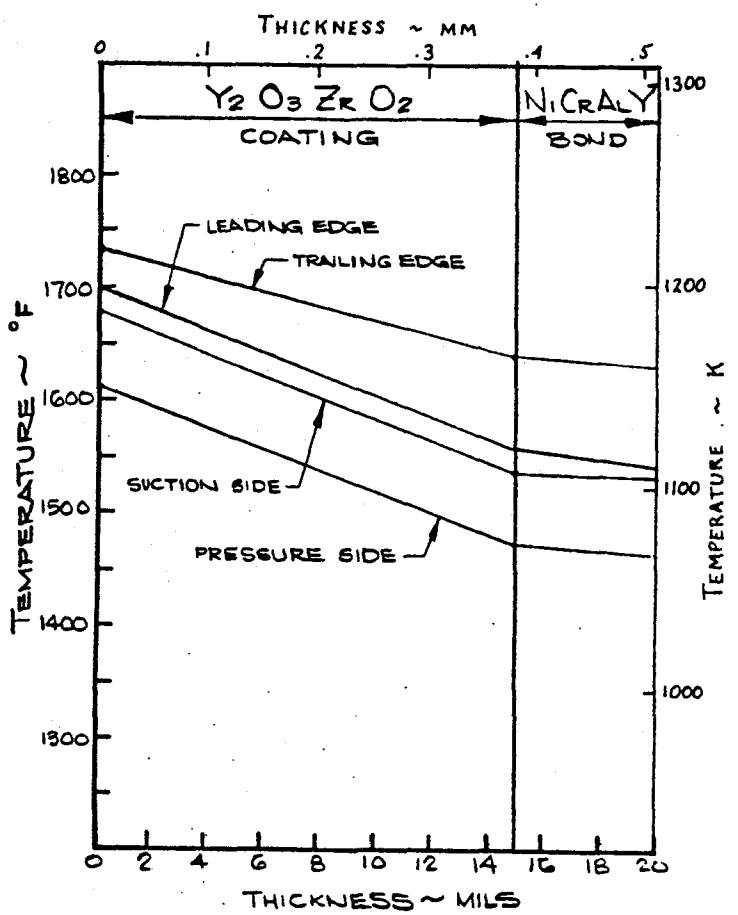

Figure 5.24 - Temperature distribution in 15 mil TBC and NiCrAlY bond at steady state

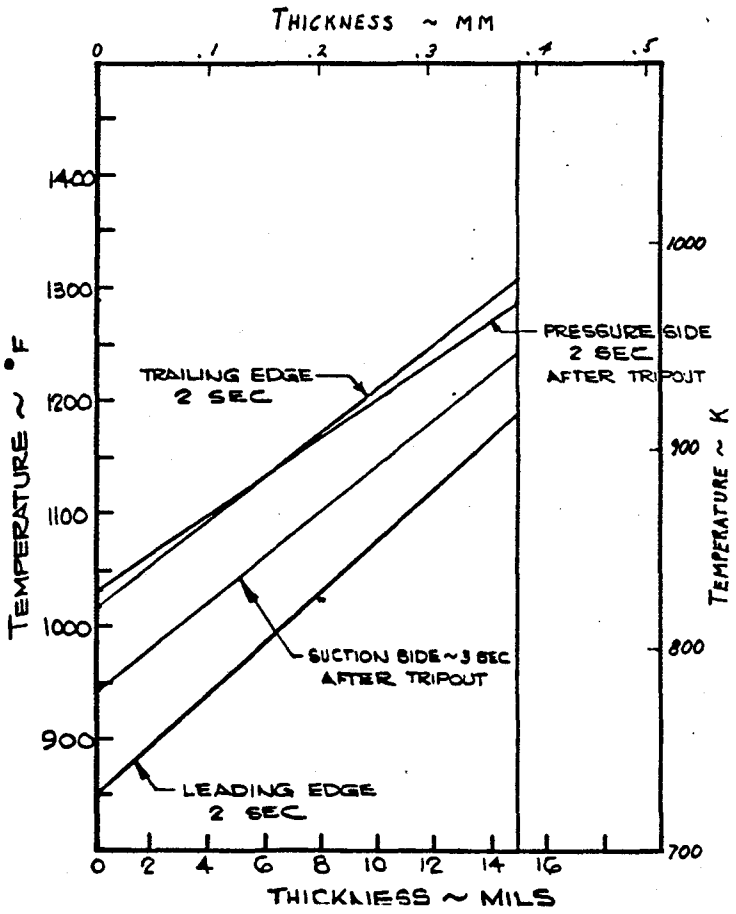

Figure 5.25 - Temperature distribution in 15 mil TBC during full load dump

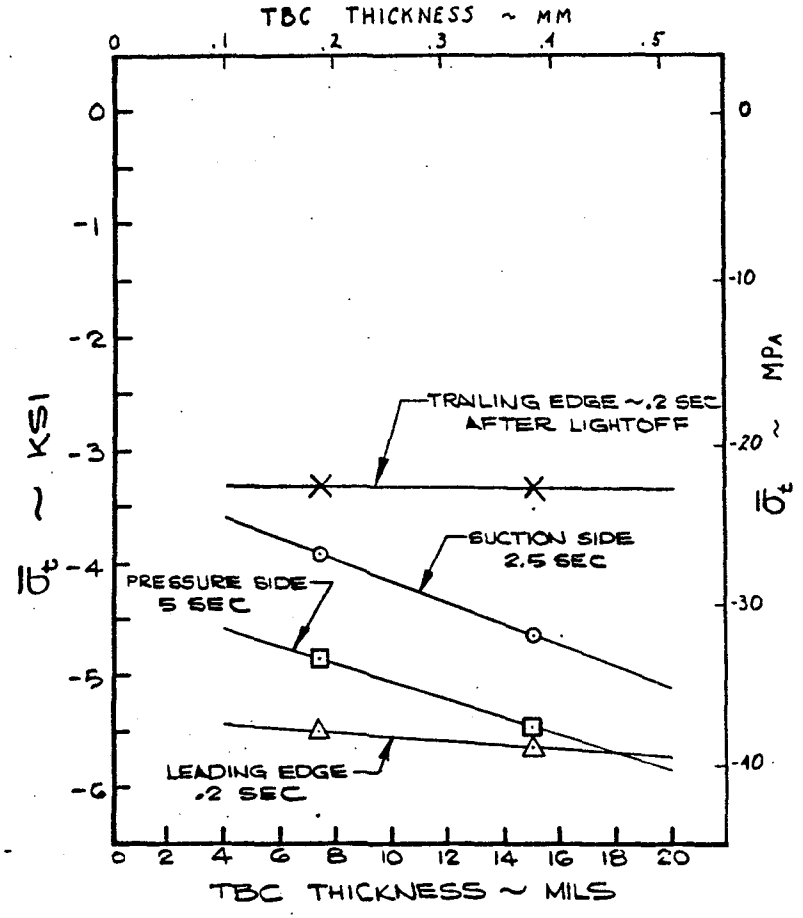

Figure 5.26 - Effect of thickness on average tangential compressive stress in TBC during normal startup

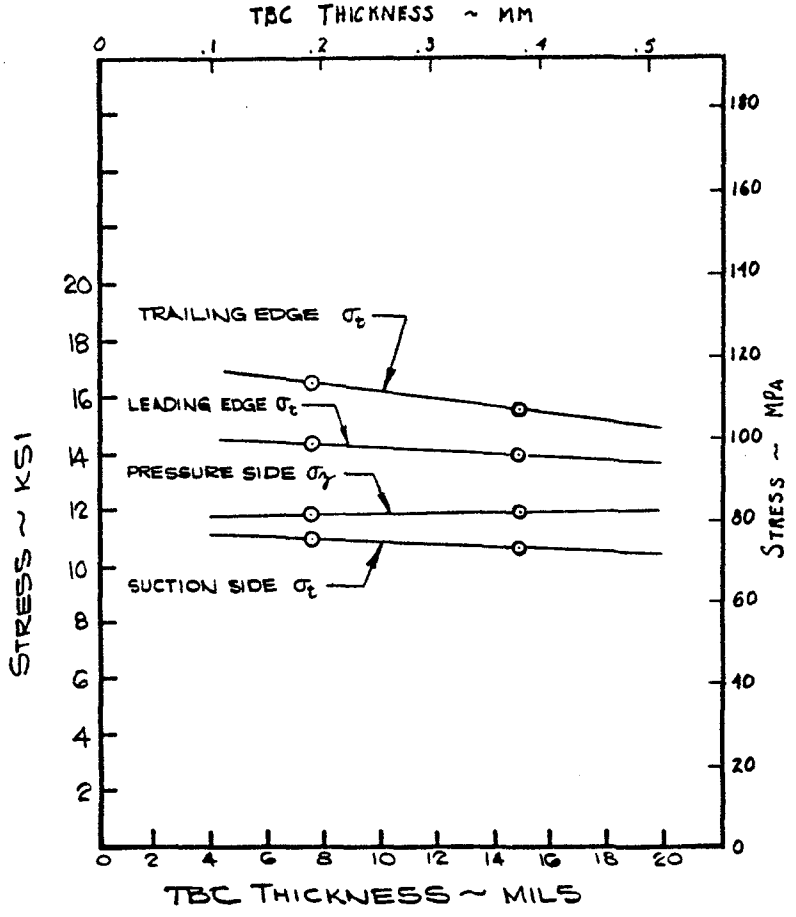

Figure 5.27 - Effect of TBC thickness on stress at interface of TBC and bond coat at steady state

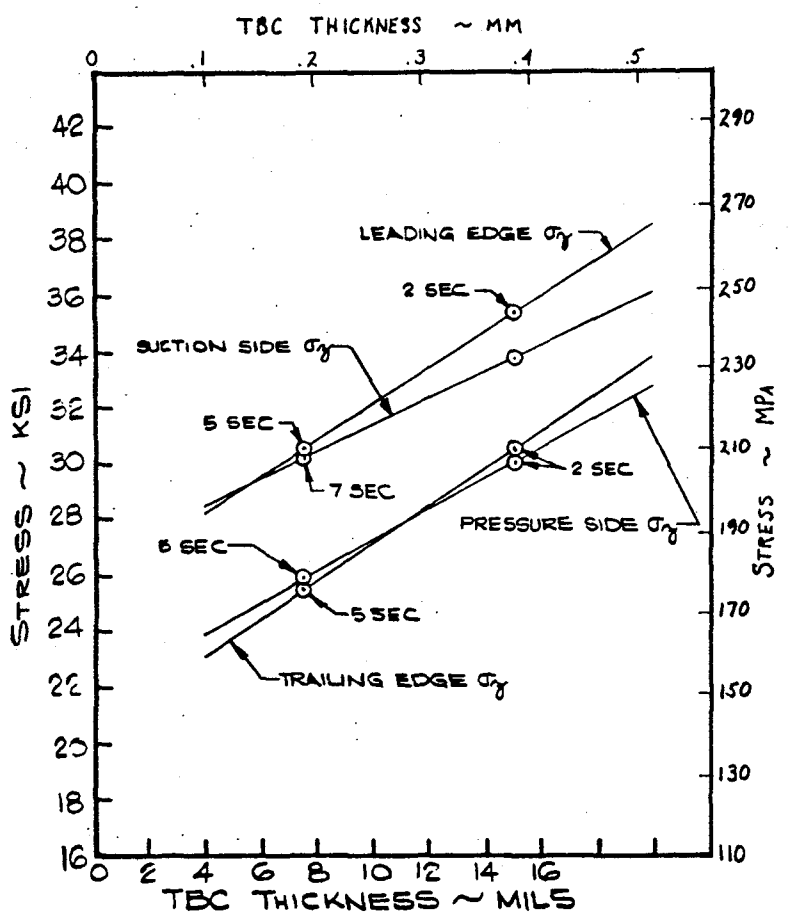

Figure 5.28 - Effect of TBC thickness on max stress in TBC from a full load tripout

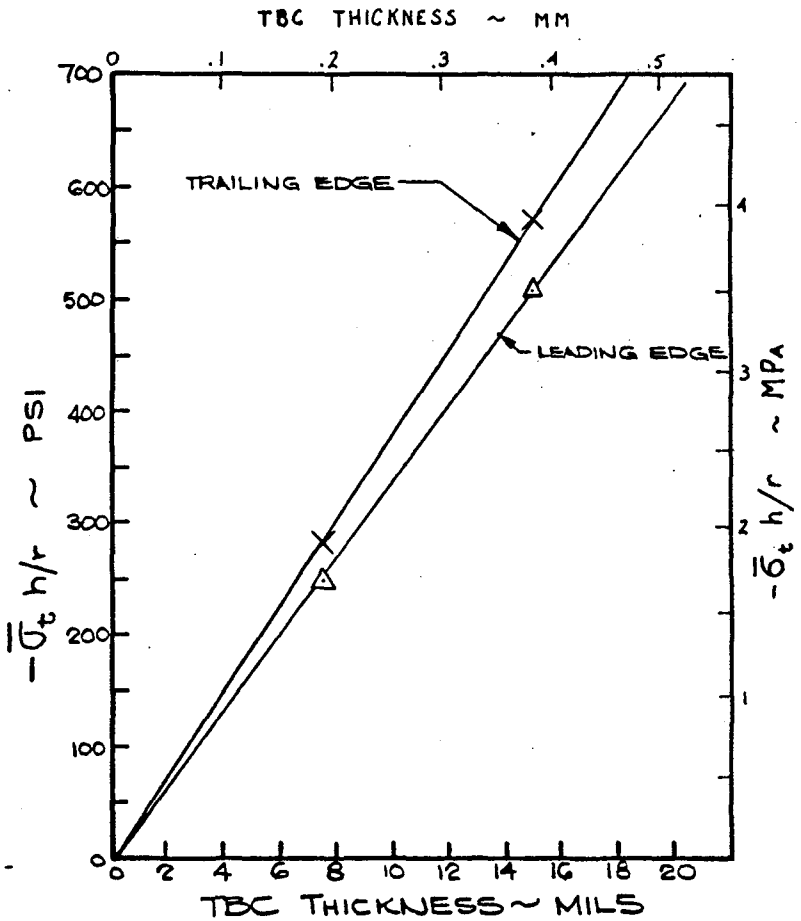

Figure 5.29 - Effect of TBC thickness on normal (bond separating) stress during normal startup

t directions for the steady state and shut down conditions shown in Figures 5.27 and 5.28. At steady state the stresses are reasonally independent of coating thickness, but increase with thickness on shut down. The stresses for both conditions are above the fracture strength of the material, and therefore cracks with planes normal to the bond interface would be expected. As previously reasoned, bond failure would not be expected.

The start-up stresses directed parallel to the bond interface are shown to be compressive in Figure 5.26. The leading and trailing edge stresses are independent of coating thickness but the side compressive stresses increase in magnitude with thickness. Compressive failures would not be expected at these magnitudes. However, the radial stresses, directed normally to the bond interface are tensile. Because of the low aspect ratio (thickness to length) used for the finite elements which modeled the coating, accurate computer determinations of these radial stresses could not be made. Since the tangential stresses were more precise, these were used to calculate the radial stresses, σ_n, via the relationship:

$$\sigma_n = \bar{\sigma}_t \, h/r \qquad (1)$$

where $\bar{\sigma}_t$ is the mean stress through the thin wall coating thickness, h, and r is the radius of curvature of the coating.

The largest normal bond stresses occur at the leading and trailing edges and are plotted as functions of coating thickness in Figure 5.29. The stresses are shown to increase linearly with coating thickness.

5.4 Effects of Coating on Engine Performance

The effects of adding thermal barrier coatings to the hot section components of an existing Westinghouse combustion turbine design, W501D, were assessed. Both thermodynamic and aerodynamic analyses were performed for two operational conditions. First, the cooling air flow was maintained

constant and the metal temperature was allowed to decrease. This is the case previously discussed which increases metal lifetime. In the second case, the metal temperature was held constant, with suitable reduction of the cooling flow. These two cases represent the operational envelop with respect to performance for constant gas temperatures.

The analyses were conducted for both simple and combined cycles. Plots of performance changes with increasing coating thickness are given in Figures 5.30 and 5.31 for the two types of cycles. These show that maintenance of the cooling flow at a constant level causes a degeneration in performance with increasing coating thickness. Specific power decreases, as does efficiency which is reciprocally related to heat rate. The causes for this can be attributed to the aerodynamic blockage by the coating (i.e., the reduction of the hot gas flow through area) as well as the thickening of the trailing edges which increases turbulence.

Performance is improved by maintaining the metal temperature constant. Since the thermal insulation of the coatings increases with thickness, less cooling air is required and less of the turbine power is needed to provide the air. Above approximately 0.38 mm of coating, the aerodynamic factors begin to reverse the improvement trend. Thus 0.38 to 0.51 mm of coating would be considered to be a maximum.

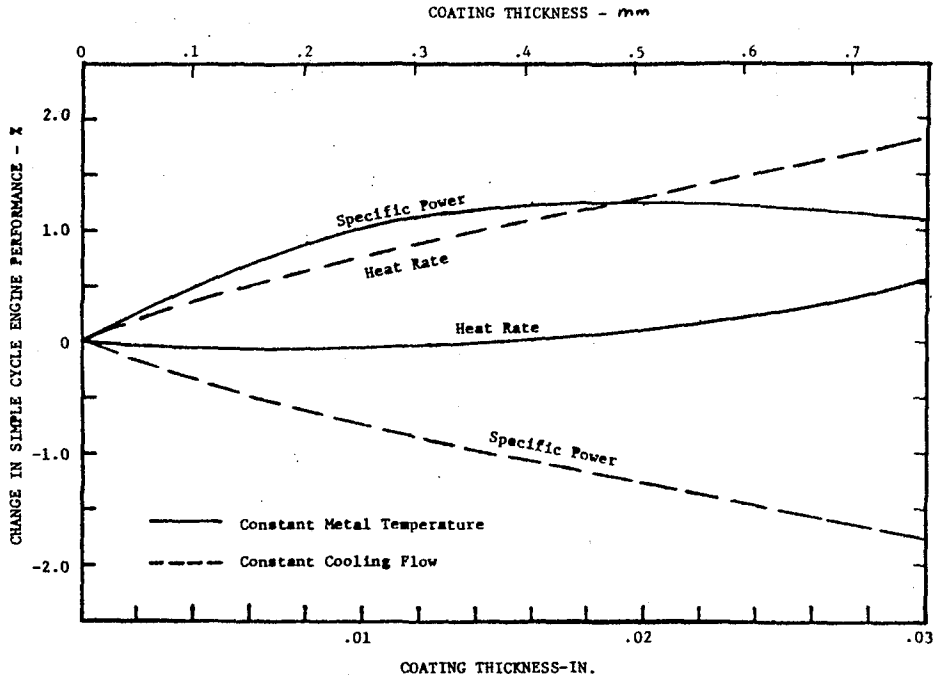

Figure 5.30 - Effect of ceramic TB coating thickness on simple cycle heat rate and specific power

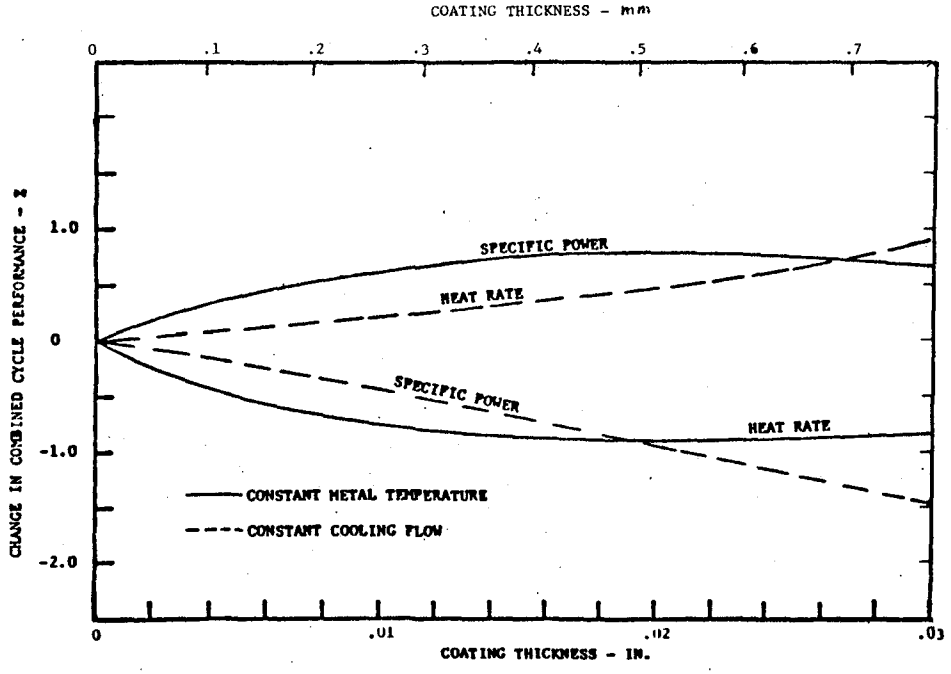

Figure 5.31 - Effect of ceramic TB coating thickness on combined cycle heat rate and specific power

6.0 COATING ENDURANCE

In order for ceramic coatings to endure turbine environments, they must be resistant to the cyclic thermal stresses imposed on them as well as to the corrosion products of combustion. These will be discussed in this section. A quantitative analysis of thermal stress failures will be presented. First, the coating stresses and types of cracks generated during the various parts of a typical engine operational cycle as well as those caused by the application processes will be surveyed. A fracture mechanics approach to analytically define coating failures is proposed. The relationships derived are used to assess the endurance of a zirconia thermal barrier coating.

The products of combustion have the potential to deteriorate both the ceramic and bond coatings. In this program, the ceramic component was primarily attacked in the dirty fuel tests. However, evidence for bond coat attack will also be discussed.

6.1 Thermal Stresses

6.1.1 Coating Stresses and Cracks

Two sources of thermally induced stresses are of concern when considering coating failure mechanisms: residual and transient operational. Residual stresses arise because most coating application methods involve heating of both the coating and substrate. A change in temperature from that of deposition will give rise to stresses due to differences in expansion between the components. The operational thermal stresses are induced by thermal gradients during the various stages of the operational thermal cycle. This latter type will be discussed first.

Analyses of typical coated heat engine components in the Coating Design Analysis section shows that the stresses are tensile in directions parallel to coating/bond interface for elevated temperature steady state operating conditions and during the cooling portion of the cycle. On the other hand, the stresses are in tangential compression during the heating portion of the cycle. Tensile tangential stresses lead to coating fractures perpendicular to the bond interface. It has been demonstrated that these types of coating cracks rarely lead to coating failure. In fact, they give the coating tolerance to large tensile strains as shown in the Coating Properties section. However, compressive tangential stresses can lead to coating flaking [ref. 15]. On flat surfaces, the failures can occur by shear parallel to the interface. On curved surfaces, tangential compressive coating stresses can induce stresses normal to the interface which can cause the coating to flake. This latter mechanism is probably the most commonly observed one, and will be the basis of the treatment given in the remainder of this section. As an example of this type of failure, coated airfoils in turbines generally flake at the leading and trailing edges where the convex radii of curvature are minimum and the normal interfacial tensile stresses are maximum.

On complex geometries, coating stresses must be determined with computer methods such as finite element analysis. However, a simple 2-dimensional treatment has been presented by McDonald which models the stresses quite well [ref. 16]. It assumes that the substrate is relatively rigid with respect to the coating and that the coating is thin with respect to its radius of curvature. The rapid heating of the coating causes it to expand with respect to the colder substrate causing it to go into tangential compression. This in turn induces a tensile stress, σ_n, normal to the bond interface. The transient tangential stress was given to be

$$\sigma_t^{tr} = -\frac{\alpha_c E_c}{(1-\nu)} \frac{Q}{A k_c} h \qquad (1)$$

where α_c is the thermal expansion coefficient, E_c is the elastic modulus, ν is Poisson's ratio, k_c is the thermal conductivity, h is the thickness, and R is the radius of curvature of the coating. The heat flux per unit area is Q/A. The stress acting against the bond is

$$\sigma_n = -\frac{h}{R} \sigma_t \tag{2}$$

Residual stresses arise from differences in thermal expansion between the coating and substrate and differences between the temperatures of the two components during deposition. In many coating operations, hot coating material is applied to a cold substrate. During application the coating temperature reduces to some average value, $\overline{T}_{cd}$, while the substrate temperature increases to another average value, $\overline{T}_{sd}$. On completion of the coating procedure, and cooling to some temperature, T, the strain difference, $\Delta\varepsilon$ is

$$\Delta\varepsilon = \alpha_s (T-\overline{T}_{sd}) - \alpha_c (T-\overline{T}_{cd}) \tag{3}$$

where α_s is the expansion coefficient of the substrate. Assuming the metal substrate to be more rigid and massive than the coating, then the tangential residual stress in the coating is given by

$$\sigma_t^{res} = \frac{E_c}{(1-\nu)} [\alpha_s (T-\overline{T}_{sd}) - \alpha_c (T-\overline{T}_{cd})] \tag{4}$$

The total normal stress to the bond interface is then obtained by summing equations 1 and 4, and substituting into equation 2

$$\sigma_n = \frac{h\, E_c}{R(1-\nu)} \left[\frac{\alpha_c Q h}{A\, k_c} + \alpha_c (T-\overline{T}_{cd}) - \alpha_s (T-\overline{T}_{sd}) \right] \tag{5}$$

For a given heat flux, the stress normal to the bond increases with increasing coating thickness, increasing elastic modulus, decreasing radius of curvature and decreasing thermal conductivity. The ceramic thermal expansion coefficient affects the transient and residual stress components differently, i.e., increasing α_c increases the former and decreases the latter stress component. Finally, the effect of the substrate temperature during deposition with respect to that of the coating must be noted, since the residual stress component can be tensile or compressive depending on the temperatures and the relative expansion coefficients. High $\overline{T}_{sd}$ values favor high tensile bond stresses and low $\overline{T}_{sd}$ values favor compressive stresses.

Thus, the stresses induced in coatings are complex and are seen to be dependent not only upon the heat flux, the material properties and the geometry, but also on the conditions of deposition.

6.1.2 Stress Intensity Factors

The stress intensity relationships for cracks parallel to the bond interface of a cylindrical coating are not available. However, an established two-dimensional relationship may be adapted if several criteria are met. The relationship is that for a long thin strip of unit width with a centrally located crack oriented with its length parallel to the crack's surface [ref. 17]. The coating can be modeled as a lengthwise half of the strip as schematically shown in Figure 6.1, if the other half (the substrate) is rigid compared to the coating half, and if the coating thickness is small compared to its radius of curvature. The strain energy release rate for the coating case would then be one half of that of the strip, and the stress intensity $2^{-1/2}$ of that of the strip.

A dimensionless plot of $K_I/\sigma_n h^{1/2}$ versus $(c/h)^{1/2}$ is also given in Figure 6.1. The curve is composed of a blending of two relationships. At small crack sizes, it appears to the crack that it is located in a semi-infinite coating medium, and the stress

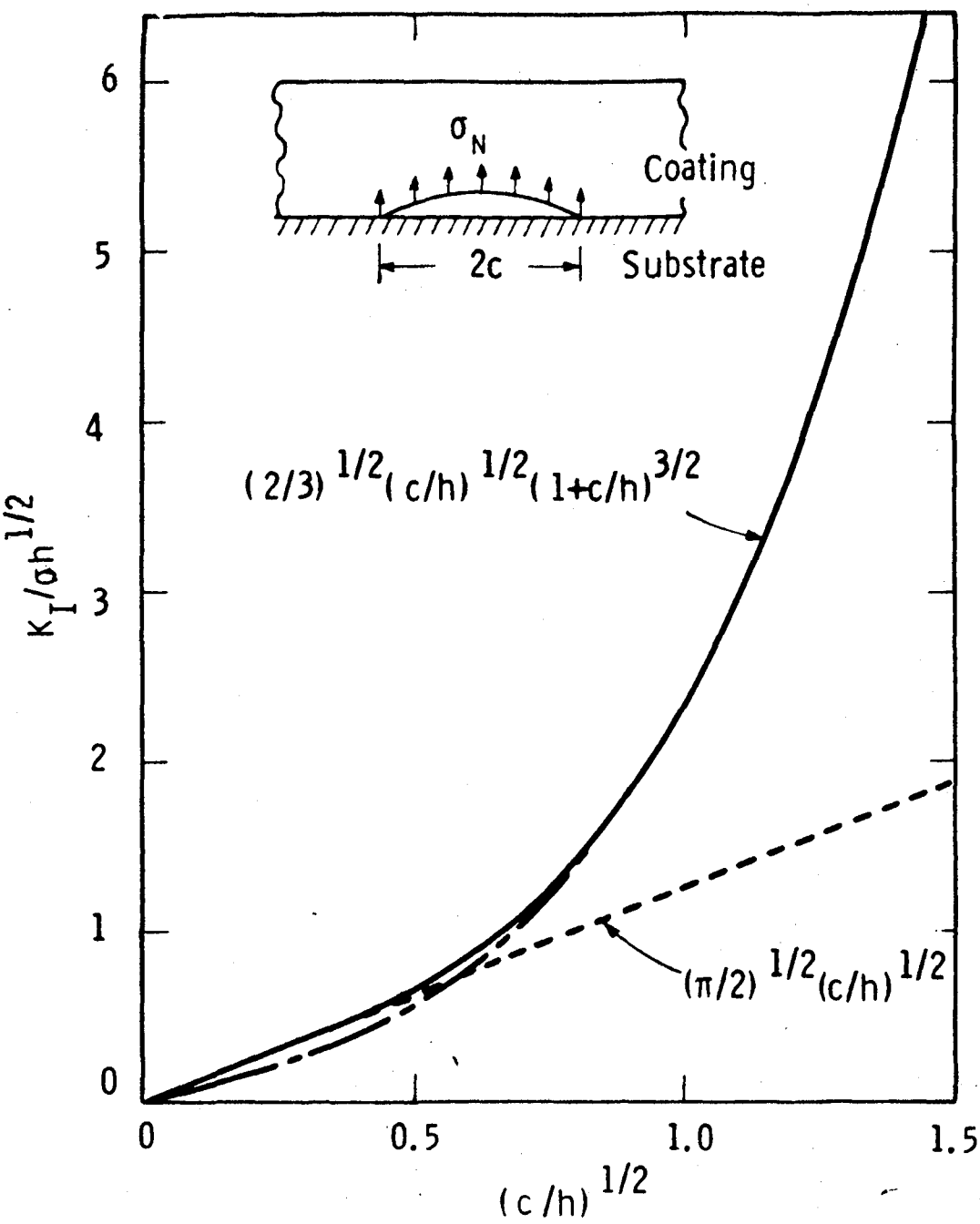

Figure 6.1 - Dimensionless stress intensity factors as a function of dimensionless crack size.

intensity is proportional to $c^{1/2}$. At crack sizes very much above c/h values of 0.4, the bending component becomes dominant and the stress intensity is proportional to c^2.

The normal stress to be used in these relationships is that given in equation 5. The single cycle failure criteria is that rapid crack propogation occurs when the applied stress intensity exceeds the critical value, K_{I_c}. In properly engineered coatings, single cycle failures are not usual. However, multicycle failures are common. The implication is that subcritical crack growth occurs.

6.1.3 Thermocyclic Crack Growth

Although either the strength or the fracture toughness criterion can be adequately used for single cycle failure, the advantages of the latter come into play when modeling cyclic failures. This is because there is no satisfactory method of describing the strength degradation caused by cycling. On the other hand, subcritical crack growth, as described in fracture toughness technology, provides an adequate model. The rate of crack growth has been determined to be approximated by:

$$\frac{dc}{dN} = B\ \Delta K_I^n \qquad (6)$$

where N is the number of cycles, ΔK_I is the stress intensity change per cycle and B and n are material constants.

For constant thermocyclic stress conditions, both c and ΔK_I (which is also a function of c) will increase with time until c reaches a critical value at which point fast fracture will occur. From Figure 6.1, the stress intensities are given by

$$\Delta\ K_I = \left(\frac{\pi}{2}\right)^{1/2} \Delta\sigma_n\ c^{1/2},\ c < 0.4\ h \qquad (7)$$

and

$$\Delta K_I = \left(\frac{2}{3}\right)^{1/2} \Delta\sigma_n c^{1/2} \left(1 + \frac{c}{h}\right)^{3/2}, \quad c > 0.4\ h \qquad (8)$$

Substituting equations 7 and 8 into equation 6, the following integral equation can be written.

$$N_f = \frac{1}{B\Delta\sigma^n}\left[\left(\frac{2}{\pi}\right)^{n/2} \int_{c_o}^{4h} \frac{dc}{c^{n/2}} + \left(\frac{3}{2}\right)^{n/2} \int_{4h}^{c_f} \frac{dc}{c^{n/2}\left(1 + \frac{c}{h}\right)^{3n/2}}\right] \qquad (9)$$

where N_f is the number of thermal cycles to failure, c_o is the initial crack size and c_f is the final crack size. In principal, the initial crack size can be determined nondestructively, although in practice this is difficult. Alternatively, it can be determined from measurements of the coating fracture strength normal to the bond interface and the critical stress intensity using the relationships given in Figure 1. The final crack size can be determined from the thermally induced applied stress intensity and those relationships. Finally, the cyclic crack growth parameters B and n must also be experimentally determined.

6.1.4 Coating Endurance

The number of thermal cycles that a thermal barrier coating can withstand before failure can be determined using equation 9 and the property values measured in the Coating Properties Section which are summarized in Table 6.1. Since the initial crack size is unknown, it must be estimated from the strength of the coating and the critical stress intensity using Figure 6.1. The final crack size can also be estimated from the thermocyclic stress and the critical stress intensity.

TABLE 6.1

Room Temperature Properties of Plasma Sprayed
Zirconia Thermal Barrier Coatings*

Property	Value
Elastic Modulus, E_c	
in tension	25.7 GPa
in compression	36.1 GPA
Poisson's Ratio, ν	0.24
Thermal Conductivity, k_c	1.51 W/m K
Coefficient of Thermal Expansion, α_c	9.06×10^{-6}/K
Tensile Strength Normal to Bond, σ_{n_f}	16.0 MPa
Critical Stress Intensity Factor, K_{I_c}	0.683 MPa $m^{1/2}$
Cyclic Crack Growth Rate Parameters:	
Coefficient, B	153 m/cycle
Power Value, n	17.3

*$ZrO_2 \cdot 8Y_2O_3$ on NiCrAlY bond coating, -200 +325 mesh, 20 v/o porosity

The results of these calculations, N_f, are plotted as a function of the total thermal stress (residual plus operational) in Figure 6.2 for a 381 μm (15 mil) thick coating. Typical operational values of $\Delta\sigma_n$ for coatings on both test bars [ref. 15] and turbine blades[(a)] have been determined to be 4 MPa. Thus coating endurance would be expected to be in excess of 10^6 cycles. However, this does not account for the residual stresses which can be of the same order. Also, this is a mean value which does not account for distributions of property values or initial crack sizes. For a total stress of 8 MPa, coatings would fail within 180 thermal cycles. For stresses in excess of 9.5 MPa, failures are expected during the first cycle. In practice, lifetimes greater than 500 cycles to failure in clean fuels have been reported in this program. Similar NASA Lewis produced coatings have lifetimes up to 1100 cycles [ref. 15].

6.2 Ceramic Coating Corrosion

6.2.1 Sodium Sulfate

In this program, deposits of Na_2SO_4 were found on all specimens after testing with both types of contaminated fuels (simulated sea salt and simulated residual fuels). This salt proved to be most detrimental to coating life. It forms as a liquid on the surfaces of the ceramic coatings, which in the present case operate at temperatures below the dew point but above the melting point of Na_2SO_4. The liquid then penetrates the pores of the coating to depths where the temperatures are above the melting point. No evidence has been found that there is a chemical reaction between Na_2SO_4 and $ZrO_2 \cdot Y_2O_3$ which was the primary material tested. Instead, it appears that the freezing and thawing of the salt during thermal cycling mechanically cracks the ceramic, ultimately causing it to flake off.

(a) Section 5.

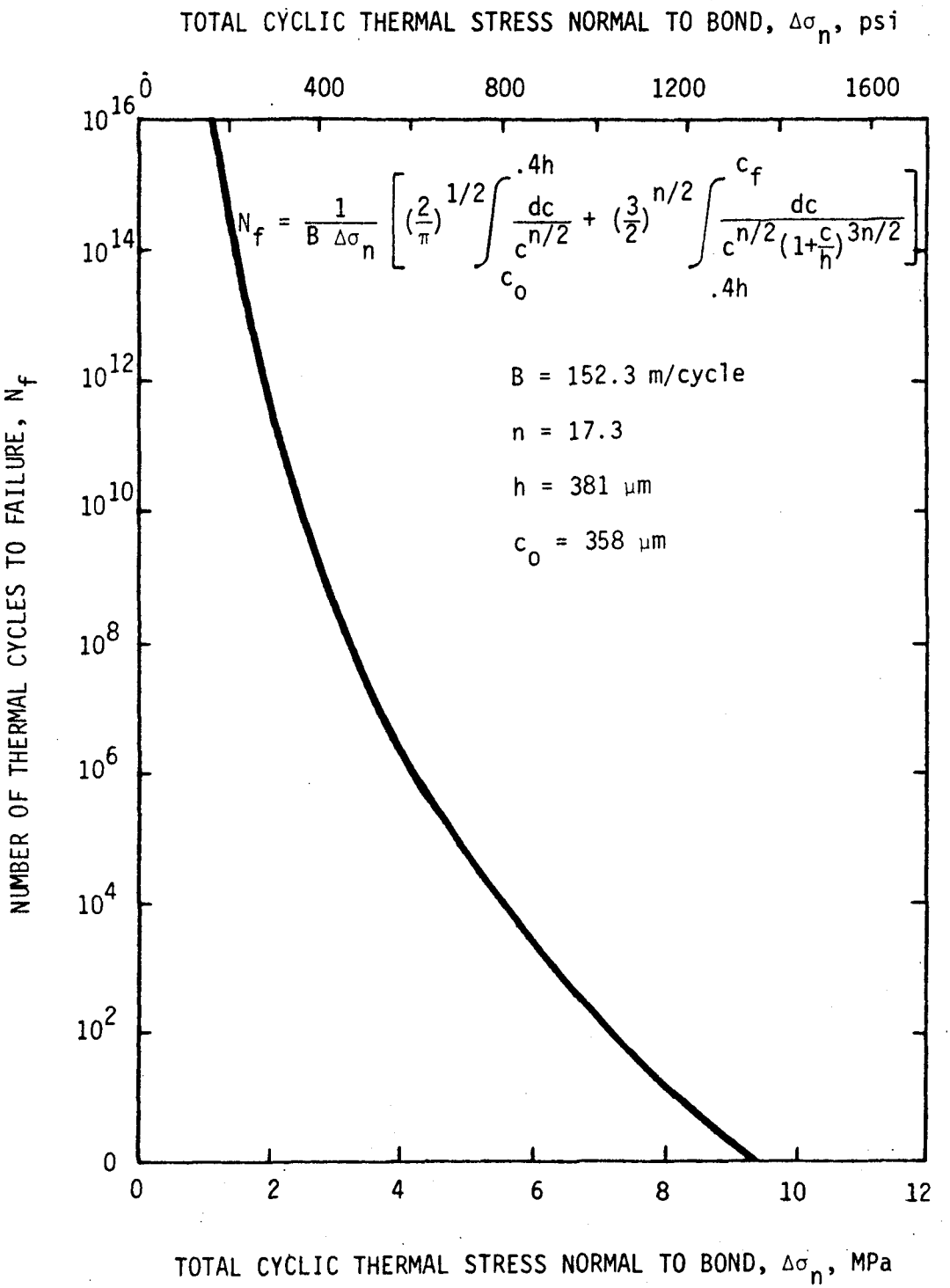

Figure 6.2 - Calculated values of coating cyclic life as a function of applied thermal stress.

The mechanism proposed for this freeze-thaw coating degradation is as follows. Assume a pore at a depth within the ceramic coating with small radiating crack(s) and that the pore and crack(s) are filled and wetted by liquid Na_2SO_4 at operational temperature. As the temperature is reduced, the salt first solidifies, adhering to the surface of the pore. The salt immediately is in a state of hydrostatic tension. As the temperature reduces further the radial tensile strain increases, since the expansion coefficient of the Na_2SO_4 is greater than that of $ZrO_2 \cdot Y_2O_3$. During this cool down portion of the thermal cycle, the induced tensile stresses in the salt relax plastically at the higher temperatures and then become more elastic at the lower temperatures. On the heating portion of the cycle, the tensile stresses in salt at first decrease in magnitude and then become compressive. At higher temperatures compressive stress relaxation and finally melting of the salt occurs. The maximum value of the hydrostatic compression stress achieved during the cycle is then dependent on the heating and cooling rates of the coating and of the creep rate of the salt. It is this hydrostatic pressurization of the pore that puts the ceramic matrix in tangential tension at the pore surface, and this in turn causes extension of the preexisting cracks. It should be noted that if the Na_2SO_4 remained elastic throughout the temperature range, this phenomenon would not occur since the salt would simply load and unload in hydrostatic tension and never become compressive. The tangential stress at the pore surface would then always be compressive and no crack extension would occur.

Failure of the coating is then by incremental crack extension due to thermal cycling until the crack reaches a critical size for fast fracture. The treatment previously presented for subcritical crack growth due to thermal cycling is valid here, and equation 6 can be used. A different stress intensity relationship is required. The case can be approximately modeled by a two dimensional circular pore of radius r with two semicracks of length c radiating

diametrically. Both the pore and cracks are subjected to an internal hydrostatic pressure p. The cyclic stress intensity factor, ΔK_I, [ref. 16] is

$$\Delta K_I = \Delta p \sqrt{\pi c}\ f(c,r) \tag{10}$$

where

$$f(c,r) = 2.24 - 3.09 \left(\frac{c}{r+c}\right) + 4.10 \left(\frac{c}{r+c}\right)^2 - 3.59 \left(\frac{c}{r+c}\right)^3 + 1.33 \left(\frac{c}{r+c}\right)^4 \tag{11}$$

The numbers of cycles to failure are determined by substituting equation 10 into 6 and integrating between the initial and final crack sizes.

There are several reasons why this is an approximation. First, it is two dimensional, whereas the porosity is not. Second it assumes a small pore size in comparison to the coating thickness. Also, the pore is considered to be singular and independent of other pores which will be acting similarly. Finally, the geometry is idealized.

For a shallow penetrating salt, the effects of the salt would be relatively independent of the thermal stress case previously presented and coating lifetime would depend on which crack propagation rate was faster. Lifetimes would be minimized by deep penetrating salts since the effects would be additive. That is, the crack extension occurring per thermal cycle would be the sum of that caused by the hydrostatic salt pressure and to that of the thermal stress in the coating. This worst case condition is usually observed since coatings subject to Na_2SO_4 corrosion fail primarily near the bond coat interface. Thus, the cyclic lifetime is

$$N_f = \frac{1}{B} \int_{c_o}^{c_f} \frac{dc}{(\Sigma \Delta K_I)^n} \tag{12}$$

where $\Sigma\Delta K_I$ is the sum of the stress intensities.

6.2.2 Vanadium and Others

Although the test conditions used in this program seem to favor Na_2SO_4 mechanical failures, chemical corrosion by V and other contaminants cannot be entirely precluded. These have been discussed in detail elsewhere [ref. 10]. Various phase destabilization mechanisms have been proposed. The $ZrO_2 \cdot Y_2O_3$ coating is primarily tetragonal as deposited. If this transforms to monoclinic, disruptive shear and dilational stresses and strains can crack the coating. Possible causes for this transformation are Y_2O_3 depletion of the $ZrO_2 \cdot Y_2O_3$ by the formation of YVO_4, or formation of ternary $ZrO_2 \cdot Y_2O_3 \cdot V_2O_5$ with differing phase stabilities.

Another possibility is enhanced crack growth by stress corrosion mechanisms. These have been observed in both metal and ceramic systems. They operate by the diffusion of gaseous or liquid species down the crack and the reaction at the highly stressed crack tips. The reactions assist bond separation by a variety of mechanisms and promote crack extension. It is possible that V_2O_5 or one of the other contaminants present could enter into the stress corrosion process, although no direct evidence has been found.

Subcritical crack growth by stress corrosion has also been empirically found to follow a power law such that

$$\frac{dc}{dt} = F \, K_I^{\,m}$$

where t is time, F and m are constants which depend on the material, the corrosive agent, temperature, etc. Systematic studies will be required to assess these effects.

6.3 Bond Coat Oxidation/Corrosion

Evidence exists for thermal barrier coating failure which is attributable to oxidation or corrosion of the bond coating. In this study, metal temperature excursions during one test to 1280 K (1850°F) caused rapid failure of a number of specimens which had been doing well up to the time of that excursion. Other programs have shown that operating bond coats at temperatures much above 1170 K (1650°F) reduces lifetime of coating systems [ref. 10]. Still others indicate that ceramic coating failures are functions of bond coat composition,, possibly associated with the oxidation resistances of those compositions [ref. 11].

The thermal stress coating failure arguments previously presented can be extended to the present discussion. Ceramic coating failures were attributed to subscritical or fast crack growth at the ceramic/bond coating interface due to thermally induced stresses. If a significant oxide/corrosion scale is formed at that interface, it would be expected to degenerate that bond strength (fracture toughness) and/or promote crack growth within the oxide scale itself. Thus, the numbers of thermal cycles to failure would be drastically reduced by the higher temperature exposures.

Corrosion of the bond coat and wire screen metals is retarded by the presence of the porous zirconia layer even though the corrosive salts have been shown to contact those metals. Several possible explanations can be proposed. First, the thermal insulation provided by the ceramic causes those metals to operate at lower temperatures and chemical reaction rates would be reduced. Equally importantly, is the fact that these reactions depend on both the transport of reactants to and products of reaction away from the surface through the salt. The tortuous path through the ceramic porosity retards diffusion and thus suppresses the reaction rates further. Both diffusion and chemical reaction are highly temperature dependent and could explain some of the rapid failures at higher operating temperatures.

7. CONCLUSIONS

The following is a summary of the principal findings of this investigation.

- For turbine operational conditions for which the combustion gas inlet temperature is maintained constant, the insulative properties of ceramic coatings on hot section components can be used to either lower the operating temperatures of the metal components or to reduce the cooling air flow requirements.

  - The benefit of lower metal operating temperatures is in the improvement of the lifetimes of the coated components with respect to uncoated components. Thermal analysis indicates that the temperature reduction provided by a 380 μm (15 mil) thick coating would improve the creep rupture and low cycle fatigue lives by an order of magnitude and the corrosion life by two times. These benefits would, however, be accompanied by a loss in turbine performance since both efficiency and specific power would be reduced.

  - The reduction in the parasitic cooling air flow required to maintain metal temperatures constant would increase turbine performance. Both specific power and efficiency would improve. Neglecting the capability of the coating to act as a corrosion barrier for the moment, no improvement in component lifetimes would be expected for this operational condition.

The benefits to be achieved are thus selective. The third alternative of raising the gas inlet temperature was not assessed in this program.

- Ceramic coatings do act as corrosion barriers. Even the poorest quality coatings assessed in this program provided some protection.

Ceramic coated specimens which spalled and flaked excessively performed better than either uncoated or NiCrAlY bond coated only specimens. For the better ceramic coatings which maintained their integrities, corrosion by the deposition salts which penetrated to the metal interfaces was retarded. A number of the best coatings did not allow penetration of those salts over the maximum test duration and would therefore be expected to provide the longest term corrosion barrier.

- Plasma sprayed zirconia on an MCrAlY bond coating remains the best ceramic coating candidate. In particular, coarse grained zirconia with 8 w/o yttria performed the best in this program. It has both the best combination of properties and has undergone the most extensive development.

- The porosity required to give ceramic coatings thermal stress resistance makes these coatings subject to failure by products of combustion which yield corrosive deposits. In particular, sodium sulfate is detrimental to coating life. Coating failure is attributable to internal mechanical stresses occurring during thermal cycling by the sodium sulfate which has penetrated the pores of the coating. Any ceramic coating with porosity connected to the surface should be subject to this cyclic freeze-thaw failure mechanism.

The failure mechanisms for coatings subjected to combustion products containing vanadium and/or magnesium could be chemical in nature. Possible mechanisms include destabilization of the zirconia and stress assisted corrosion at crack tips.

- Lifetimes of porous ceramic coatings in corrosive environments can be significantly lengthened by applying dense overcoats to retard penetration of contaminants into the interiors of the coatings. The best overcoats assessed in this program for the plasma sprayed course particle zirconia basecoat were:

  - plasma sprayed fine particle zirconia
  - plasma sprayed fine particle zirconia containing 20 to 25 v/o of certain glasses.

The best combination was 4.5 times better than the NASA baseline and sputter overcoated combined average, and 3.2 times better than the Westinghouse baseline coating.

- Thermal cyclic lifetimes of ceramic coatings can be improved by incorporating a wire metal screen intermediate to the ceramic and bond coats. The screen functions as a mechanical lock for the ceramic and retards crack propagation. Although the times to the observations of initial failure did not differ significantly for specimens with and without this intermediate layer, the rate of subsequent flaking was less for the specimens with the screens.

Intermediate layers which consisted of a mixture of ceramic and bond materials performed nearly as well as the wire screen and no intermediate layers. However, such graded coatings are limited to lower metal operative temperatures than duplex coatings. Feltmetal intermediate layers had significantly lower lifetimes.

- An understanding of thermal stress failures was achieved. Analytical models based on fracture mechanics theories were derived for quantitatively assessing both single cycle and multiple thermal cycle failures. The models account for both the thermal transient and residual stresses induced in the coatings. Both geometries and material properties are considered. Predictions of the thermal cyclic lifetimes of zirconia coatings were made.

8. RECOMMENDATIONS

Ceramic coatings on hot stage components can improve either the component lifetimes or the overall turbine performance. The endurance of a number of candidates in clean fuel combustion is reasonably good. Although considerable progress was made in this program to improve endurance of coatings subjected to lower grade fuels and/or marine environments, the endurance still falls short of the 10,000 hour industrial/utility turbine requirements. Quantification of the thermal stress failure mechanism was initiated in the program, but corrosion mechanisms are only qualitatively understood. Based on these results, the following recommendations are made.

- The most promising ceramic coatings in this study should be applied to utility turbine components of an existing design for testing in the field. The specific turbine selected should be one that operates with clean fuel so as to improve the survival probability of the coatings. The purpose of this testing is to investigate durability under actual operating conditions.

- Another iteration of coating development is required to further improve corrosion/oxidation resistances of the coating systems. Items to be investigated include:
  - Densification and optimization of the bond coating composition to further improve its oxidation and corrosion resistance at higher metal operating temperatures.
  - Optimization of the application procedures of the ceramic coatings to further improve their thermal stress resistance.
  - Optimization of the dense overcoat to ensure its long term integrity as a barrier to penetration of contaminants.

- Investigation of other promising coatings now under development such as EB-PVD coatings or other plasma spray types.

- Basic studies should be undertaken to improve the understanding of the functioning of ceramic coatings:
  - Coating failures are by propagation of cracks parallel to the bond coating interface. Understanding of these mechanisms require the application of fracture mechanics technology. Although this was initiated in the present study with regard to cylindrical geometries, further refinements are required and other geometries such as coated flat surfaces should be assessed.
  - Two types of corrosion mechanisms were identified in the program. Sodium sulfate causes mechanical crack propagation during thermal cyclic operations. A fracture mechanics approach should be used to quantify this failure mode. Vanadium corrosion on the other hand is probably chemical in nature and requires a thermochemical approach.
  - Oxidation of the bond coat at the interface with the ceramic coating could create an easy path for fracture. A basic investigation of this mechanism should also be made.

These and other fundamental studies are required to more efficiently design coatings. The more empirical approach that has been used to date has been necessary to obtain a data base and has been relatively successful. However, it has been costly. Future development work could be more focused if the fundamentals were better understood.

9. REFERENCES

1. A. Peckman, "Ceramics for High Temperatures," Chem. Eng., Vol. 60, No. 11, pp 186-190, 1953.

2. W. D. Walton, Jr., "Present and Future Problem Areas for High Temperature Inorganic Coatings," Amer. Ceram. Soc. Bull., Vol. 40, No. 3 pp 136-141, 1961.

3. J. V. Long, "Refractory Coatings for High Temperature Protection," Metal Prog., Vol. 79, No. 3 pp 114-120, 1961.

4. C. J. Spengler, S. Y. Lee and S. T. Scheirer, "Corrosion Evaluation of Superalloys and Metal Coatings for Combustion Turbines Utilizing Alternative Fuels," Proc. First Conf. on Advanced Materials for Alternative Fuel Capable Directly Fired Heat Engines, July, 1979, Castine ME., pp 416-447, 1979.

5. Anonymous, "Ceramic Protection for Jet Aircraft," Ceramic Age, Vol. 68, No. 3, pp 22, 23, 36, 1956.

6. W. B. Brown and JNB Livingood, "Cooling of Gas Turbines, IX, Cooling Effects from Use of Ceramic Coatings on Water-Cooled Turbine Blades," Natl. Advisory Comm. Aeronautical Res. Memo, 1948, No. E8H03.

7. S. Stecura and C. H. Liebert, "Thermal Barrier Coating System, U. S. Patent No. 4,055,705, Oct. 25, 1977.

8. S. Levine, P. Hodge and R. Miller, "NASA Progress on Ceramic Coatings for Industrial/Utility Gas Turbines" Proc. First Conf. on Advance Materials for Alternative Fuel Capable Directly Fired Heat Engines, July 1979, Castine, ME., pp 667-679, 1979.

9. R. J. Bratton, S. C. Singhal and W. Hays, "Ceramic Rotor Blade Development, Part I - Ceramic Thermal Barrier Coatings" Final Report, EPRI Research Project RP 421-1, 1977.

10. R. J. Bratton, S. K. Lau and S. Y. Lee, "Evaluation of Present Thermal Barrier Coatings for Potential Service in Electric Utility Gas Turbines" Final Report, NASA CR-165545, 1981.

11. S. Stecura, "Effects of Yttrium, Aluminum and Chromium Concentrations in Bond Coatings on the Performance of Zirconia-Yttria Thermal Barriers, NASA TM-79206, 1979.

12. G. E. McDonald, Communication from NASA Lewis Research Center.

13. J. W. Patten, R. W. Moss, M. A. Bayne, D. D. Hays, E. D. McClanahan and J. W. Fairbanks, "Development of Sputter Deposited Multilayered Ceramics Metal Coatings," Proc. First Conf. on Advanced Materials for Alternative Fuel Capable Directly Fired Heat Engines, Castine, ME., July, 1979, pp 615-628, 1979.

14. R. E. Demaray, "Dedicated Electron Beam Reactive Physical Vapor Deposition (R.P.V.D.) Apparatus for the Production of Ceramic Thermal Barrier Coatings," Airco Timescal Final Report Batelle/DOE Subcontract No. B-A0760-A-U 1981.

15. D. E. Andress, "Analytical Study of Thermal Barrier Coated - First Stage Blades in an F-100 Engine," NASA CR-135359, 1978.

16. G. McDonald and R. C. Henricks, "Effect of Thermal Cycling on ZrO_2-Y_2O_3 Thermal Barrier Coatings," Thin Solid Films, Vol. 73, pp. 491-496, 1980.

17. H. Tada, P. C. Paris and G. R. Irwin, "The Stress Analysis of Cracks Handbook," Del Research Corp., Hellertown, PA (1973).